Surprising Magnetotransport in Oxide Heterostructures

Veerendra K. Guduru

Surprising Magnetotransport in Oxide Heterostructures
Veerendra Kumar Guduru
Thesis Radboud Universiteit Nijmegen - Illustrated
With references - With summary in Dutch
ISBN: 978-94-6259-138-7
Cover: Schematic illustration of oxide heterostructure with the applied
magnetic field-oriented perpendicular to its interface.

Surprising Magnetotransport in Oxide Heterostructures

PROEFSCHRIFT

ter verkrijging van de graad van doctor
aan de Radboud Universiteit Nijmegen,
op gezag van de rector magnificus prof. mr. S.C.J.J. Kortmann,
volgens besluit van het college van decanen
in het openbaar te verdedigen op dinsdag 3 juni 2014
om 12:30 uur precies

door

Veerendra Kumar Guduru

geboren op 26 Augustus 1984
te Guntur (India)

PROMOTOR:	PROF. DR. IR. J. C. MAAN
COPROMOTOR:	DR. A. MCCOLLAM DR. U. ZEITLER
MANUSCRIPTCOMMISSIE:	PROF. DR. A. FASOLINO
	PROF. DR. IR. A. BRINKMAN (UNIVERSITEIT TWENTE)
	PROF. DR. M. S. GOLDEN (UNIVERSITEIT VAN AMSTERDAM)

Het werk beschreven in dit proefschrift is uitgevoerd aan de faculteit der Natuurwetenschappen, Wiskunde en Informatica van de Radboud Universiteit Nijmegen en maakt deel uit van het onderzoeksprogramma van de 'Stichting voor Fundamenteel Onderzoek der Materie' (FOM), die financieel gesteund wordt door de Nederlandse Organisatie voor Wetenschappelijk onderzoek (NWO).

And I set my heart to seek and search out by wisdom
concerning all that is done under heaven;
this burdensome task God has given to the sons of man,
by which they may be exercised.
King Solomon (Ecclesiastes 1:13)

Contents

Chapter 1

General introduction

In the last few decades, developments in electronic devices have drastically changed the way society functions daily and the quality of life for many has improved. This change was made possible by new physical effects and electronic device concepts brought forth by semiconductor physics research from the middle of the 20^{th} century. The success of this research is based on the fact that fundamental understanding and realization of functional properties of various materials go hand-in-hand, resulting in very successful technological applications coming from fundamental research.

In the line of discoveries which made this possible, the first one to mention is the practical realization of the transistor effect in a semiconducting material germanium by J. Bardeen, W. Brattain, and W. Shockley in 1947. The entire field of semiconductor physics is based on manipulating the flow of electrons and thereby making electricity carry signals or perform work to realize a desired functionality.[1] Examples are the theoretical prediction[2] in 1926 and the experimental demonstration[3] in 1959 of electric field-effect phenomenon in metal-oxide semiconductor transistors made of silicon, which is now the backbone of modern electronics, and the giant magnetoresistance effect,[4] which is the principle behind computer hard drive and flash memory.

Further advancement in semiconductor research led to the development of semiconductor heterostructures, termed as "man made crystals" by Leo Esaki. Heterostructures can be defined as heterogeneous semiconductor structures combining two or more different materials. In a heterostructure, the transition region or the common boundary or interface between materials plays the essential role in defining the device properties or functionality, according to Nobel laureate H. Kroemer "the interface is the device".[5] Introducing the heterostructure concept into semiconductor physics research has led to the discovery of new physical effects such as the (fractional) quantum Hall effect.[6,7] At the same time it revolutionized technology, which has led to the fundamental improvement of characteristics of all known practical semiconductor devices, and the invention of new ones.[8] Additionally, research on semiconductor heterostructures led to the development of low-dimensional semiconductors such as heterostructure quantum wells, superlattices, quantum wires, quantum dots, and their fundamental understanding and technological applications.[9]

The concept of making heterostructures has been extended to materials with more complex composition such as different types of transition metal oxides. The study of the fundamental physical properties and potential applications of complex oxide based heterostructures is a rapidly developing field of research in condensed matter science.[10–12] The remarkable discovery of the spontaneously formed conducting interface between two band-insulating perovskite oxides $SrTiO_3$ (STO) and $LaAlO_3$ (LAO)[13] in 2004, attracted lots of attention. Many of its physical attributes closely resemble those of conventional semiconductor heterostructures such as quantum oscillations with 2D character[14–16] and electric field tunable switching.[17,18] At the same time, the LAO/STO conducting interface was found to exhibit some other physical properties such as superconductivity[19] and magnetism.[20–24]

Currently there are three proposed mechanisms for the interface conductivity in LAO/STO heterostructures: (i) *electronic reconstruction*, where the transfer of charge across a polar (LAO) to nonpolar (STO) interface causes effective electron doping at the interface to avoid a "polar catastrophe" due to diverging potential across the LAO film;[25–27] (ii) *oxygen vacancies* formed at the interface during the growth of LAO film on STO substrate can dope the interface by donating two free electrons for each oxygen vacancy;[28,29] (iii) *La/Sr intermixing* as a result of lattice deformation at the interface. In this scenario, the polar catastrophe can be avoided due to compositional roughening at the interface.[30] Though these mechanisms are proposed to be responsible for conducting interface in LAO/STO heterostructures, the exact origin and nature of the interface charge carriers is still not clear. In order to realize the full potential of LAO/STO heterostructures in technological applications, the fundamental origin and state of the interface conductivity has to be understood thoroughly.

This thesis work describes our contribution to the on-going efforts to understand the type of conduction charge carriers present at the LAO/STO interface, and their physical origin. In our investigation we have used two kinds of LAO/STO heterostructures, one that exhibits magnetic signatures and another that shows quantum oscillations. Our experimental investigations of these two kinds of samples are presented in detail in chapters 3, 4, 5 and 6 of this thesis. Basically by varying the number of monolayers of the deposited LAO/STO a different behaviour is observed and studied in this thesis. The contents of this thesis is summarised in the following.

The second chapter provides general introductions to the growth of oxide heterostructures using pulsed laser deposition and the transport properties of two-dimensional (2D) electron systems, together with experimental techniques used in our magnetotransport measurements. The third chapter describes the magnetotransport experiments performed on an LAO/STO sample which exhibits magnetic signatures, after illumination with selective photon energies.[31] The results of our investigation by means of Hall effect measurements shows that illuminating the surface of the sample with UV light of energy greater than the STO bandgap, optically excites a parallel high mobility electron conducting channel. In the fourth chapter, we study the interface electronic structure of the magnetic LAO/STO heterostructure, by means of temperature and magnetic-field-orientation-dependent magnetotransport measurements. Our analysis of the Hall resistance and magnetoresistance data shows that two electron-like conduction channels, with different densities and mobilities, are present at the interface, in agreement with the results in chapter 3.[32, 33]

In the fifth chapter, we describe the magnetotransport performed on LAO/STO samples which show Shubnikov-de Haas (SdH) oscillations in high magnetic fields and at low-temperatures. The analyses of the SdH results reveal that four or five 2D conduction subbands are present at the interface with different electron effective masses. Magnetic-field-orientation-dependent measurements confirm the multiple 2D subband structure of the Fermi surface.[16] In the sixth chapter we study magnetic scattering in LAO/STO heterostructures in high magnetic fields and at low-temperatures with magnetotransport experiments. The analysis of our results indicates the presence of magnetic moments, which are coupled antiferromagnetically via the interface conduction electrons at very low-energy scale.

References

[1] Jack S. Kilby, Nobel Lecture in Physics (2000), available at: http://www.nobelprize.org/nobelprizes/physics/laureates/2000/kilby-lecture.pdf.

[2] J. E. Lilienfeld,“Method and apparatus for controlling electric currents,” U. S. Patent No. 1,745,175 (Filed October 8, 1926. Issued January 18, 1930), available at: http://www.computerhistory.org/semiconductor/timeline/1926-field.html.

[3] D. Kahng,“Electric Field Controlled Semiconductor Device,” U. S. Patent No. 3,102,230 (Filed 31 May 31, 1960, issued August 27, 1963), available at: http://www.computerhistory.org/semiconductor/timeline/1960-MOS.html.

[4] M. N. Baibich, J. M. Broto, A. Fert, F. N. Van Dau, F. Petroff, P. Eitenne, G. Creuzet, A. Friederich, and J. Chazelas, Phys. Rev. Lett. **61**, 2472 (1988).

[5] H. Kroemer, Rev. Mod. Phys. **73**, 783 (2001).

[6] K. von Klitzing, Rev. Mod. Phys. **58**, 519 (1986).

[7] H. L. Störmer, Rev. Mod. Phys. **71**, 875 (1999).

[8] H. L. Störmer, R. Dingle, A. C. Gossard, W. Wiegmann, and M. D. Sturge Solid State Commun., **29**, 705 (1979).

[9] Zhores I. Alferov, Rev. Mod. Phys. **73**, 767 (2001).

[10] H. Y. Hwang, Y. Iwasa, M. Kawasaki, B. Keimer, N. Nagaosa, and Y. Tokura, Nature Mater. **11**, 103 (2012).

[11] J. Mannhart and D. G. Schlom, Science **327**, 1607 (2010).

[12] E. Assmann, P. Blaha, R. Laskowski, K. Held, S. Okamoto, and G. Sangiovanni, Phys. Rev. Lett. **110**, 078701 (2013).

[13] A. Ohtomo and H.Y. Hwang, Nature **427**, 423 (2004).

[14] M. Ben Shalom, A. Ron, A. Palevski, and Y. Dagan, Phys. Rev. Lett. **105**, 206401 (2010).

[15] A. D. Caviglia, S. Gariglio, C. Cancellieri, B. Sacepe, A. Fete, N. Reyren, M. Gabay, A. F. Morpurgo, and J.-M. Triscone, Phys. Rev. Lett. **105**, 236802 (2010).

[16] A. McCollam, S. Wenderich, M. K. Kruize, V. K. Guduru, H. J. A. Molegraaf, M. Huijben, G. Koster, D. H. A. Blank, G. Rijnders, A. Brinkman, H. Hilgenkamp, U. Zeitler, and J. C. Maan, Appl. Phys. Lett.: Materials **2**, 022102 (2014).

[17] S. Thiel, G. Hammerl, A. Schmehl, C. W. Schneider, and J. Mannhart, Science **313**, 1942 (2006).

[18] A. D. Caviglia, S. Gariglio, N. Reyren, D. Jaccard, T. Schneider, M. Gabay, S. Thiel, G. Hammerl, J. Mannhart, and J.-M. Triscone, Nature (London) **456**, 624 (2008).

[19] N. Reyren, S. Thiel, A. D. Caviglia, L. F. Kourkoutis, G. Hammerl, C. Richter, C. W. Schneider, T. Kopp, A. S. Ruetschi, D. Jaccard, M. Gabay, D. A. Muller, J.-M. Triscone, and J. Mannhart, Science **317**, 1196 (2007).

[20] A. Brinkman, M. Van Zalk, J. Huijben, U. Zeitler, J. C. Maan, W. G. Van der Wiel, G. Rijnders, D. H. A. Blank, and H. Hilgenkamp, Nature Mater. **6**, 493 (2007).

[21] Ariando, X. Wang, G. Baskaran, Z. Q. Liu, J. Huijben, J. B. Yi, A. Annadi, A. R. Barman, A. Rusydi, S. Dhar, Y. P. Feng, J. Ding, H. Hilgenkamp, and T. Venkatesan, Nature Commun. **2**, 188 (2011).

[22] D. A. Dikin, M. Mehta, C. W. Bark, C. M. Folkman, C. B. Eom, and V. Chandrasekhar, Phys. Rev. Lett. **107**, 056802 (2011).

[23] L. Li, C. Richter, J. Mannhart, and R. C. Ashoori, Nature Phys. **7**, 762 (2011).

[24] J. A. Bert, B. Kalisky, C. Bell, M. Kim, Y. Hikita, H. Y. Hwang, and K. A. Moler, Nature Phys. **7**, 767 (2011).

[25] N. Nakagawa, H. Y. Hwang, and D. A. Muller, Nature Mater. **5**, 204 (2006).

[26] K. Yoshimatsu, R. Yasuhara, H. Kumigashira, and M. Oshima, Phys. Rev. Lett. **101**, 026802 (2008).

[27] M. Sing, G. Berner, K. Goß, A. Müller, A. Ruff, A. Wetscherek, S. Thiel, J. Mannhart, S. A. Pauli, C. W. Schneider, P. R. Willmott, M. Gorgoi, F. Schäfers, and R. Claessen, Phys. Rev. Lett. **102**, 176805 (2009).

[28] W. Siemons, G. Koster, H. Yamamoto, W. A. Harrison, G. Lucovsky, T. H. Geballe, D. H. A. Blank, and M. R. Beasley, Phys. Rev. Lett. **98**, 196802 (2007).

[29] G. Herranz, M. Basleti, M. Bibes, C. Carretero, E. Tafra, E. Jacquet, K. Bouzehouane, C. Deranlot, A. Hamzi, J.-M. Broto, A. Barthelemy, and A. Fert, Phys. Rev. Lett. **98**, 216803 (2007).

[30] P. R. Willmott, S. A. Pauli, R. Herger, C. M. Schleptz, D. Martoccia, B. D. Patterson, B. Delley, R. Clarke, D. Kumah, C. Cionca, and Y. Yacoby, Phys. Rev. Lett. **99**, 155502 (2007).

[31] V. K. Guduru, A. Granados del Aguila, S. Wenderich, M. K. Kruize, A. McCollam, P. C. M. Christianen, U. Zeitler, A. Brinkman, G. Rijnders, H. Hilgenkamp, and J. C. Maan, Appl. Phys. Lett. **102**, 051604 (2013).

[32] V. K. Guduru, A. McCollam, S. Wenderich, M. K. Kruize, A. Brinkman, M. Huijben, G. Koster, D. H. A. Blank, G. Rijnders, H. Hilgenkamp, J. C. Maan, and U. Zeitler, J. Kor. Phys. Soci. **63**, 437 (2013).

[33] V. K. Guduru, A. McCollam, A. Jost, S. Wenderich, H. Hilgenkamp, J. C. Maan, A. Brinkman, and U. Zeitler, Phys. Rev. B **88**, 241301(R) (2013).

Chapter 2

Growth and magnetotransport theory of oxide heterostructures

Abstract

In this chapter we provide a general introduction to the growth of oxide heterostructures and the general transport properties of two-dimensional electron systems. First we introduce the procedure to make the conducting $LaAlO_3/SrTiO_3$ heterostructures with main focus on the pulsed laser deposition technique. In the second part we describe the theoretical concepts used to explain magnetotransport properties of such 2D electron systems in the classical and quantum-mechanical regime.

2.1 Introduction

The advancement of material processing technologies in the past few decades has enabled production of ultra pure (down to atomic level) thin films from a wide variety of materials. A good example is the epitaxial growth of semiconductor heterostructures with extremely high purity and crystalline quality, allowing exploration of their fundamental and functional physical properties.[1] Molecular beam epitaxy (MBE) and pulsed laser deposition (PLD) are the most widely used techniques to realize epitaxial quality films down to single atomic-layer precision. The successful application of MBE is demonstrated in the growth of high quality semiconducting AlGaAs/GaAs[2] and wide band gap semiconducting oxide ZnMgO/ZnO[3,4] heterostructures. PLD is widely used for the growth of complex oxide thin-films, such as high-T_c superconductors $YBa_2Cu_3O_7$ and $Bi_2Sr_2Ca_2Cu_3O_{10}$.[5,6] The addition of reflection high-energy electron diffraction (RHEED) to the PLD and MBE techniques enables *in situ* monitoring of the growth of thin films with precision of a single atomic layer, as well as investigation of their surface quality.[7,8]

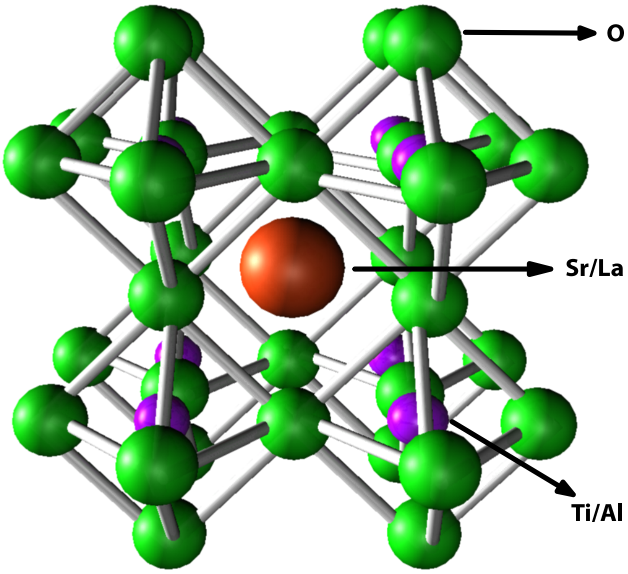

Figure 2.1: *Schematic of general perovskite crystal structure consist of layers of SrO and TiO_2 for $SrTiO_3$ and layers of LaO and AlO_2 for $LaAlO_3$. The atomic orbitals are completely filled for both $SrTiO_3$ and $LaAlO_3$ making them electrical insulators.*

Availability of such advanced thin film production techniques enabled us to explore the physical properties of a new class of heterostructures based on transition metal oxide (TMO) thin films. This an emerging field of research in condensed matter science[9] started with the discovery of metallic conductivity in TMO heterostructures ($LaTiO_3/SrTiO_3$) formed out of two insulating materials $SrTiO_3$ and $LaTiO_3$.[10] The major breakthrough in this new class of TMO based heterostructures came with the discovery of a high mobility 2-dimensional (2D) conducting interface ($LaAlO_3/SrTiO_3$) between two band-insulting perovskite oxides $SrTiO_3$ (STO, nonpolar) and $LaAlO_3$ (LAO, polar) in 2004 by Ohtomo and Hwang.[11] Schematic of $SrTiO_3$ and $LaAlO_3$ perovskite oxide crystal structure is shown in Fig. 2.1. In recent years, extensive research on conducting LAO/STO heterostructures, fabricated mainly by the PLD technique, led to the discovery of novel electronic phases exhibited by this interface. This interface exhibits superconductivity,[12] magnetism,[13–15] tunable switching of high mobility interface conductivity,[16–19] quantum oscillations,[11,20–22] coexistence of superconductivity and ferromagnetism in two dimensions.[23–25] The fabrication of the LAO/STO heterostructures using the PLD technique is described below.

2.2 Growth of oxide heterostructures

The fabrication process of LAO/STO heterostructures consists of two major steps: singly terminating the [001] surface of a high quality crystalline $SrTiO_3$ substrate with TiO_2 (section 2.2.1), and subsequently growing an atomically sharp LAO film on it in the PLD chamber (section 2.2.2). All the samples discussed in this thesis were fabricated at MESA+ Institute for Nanotechnology in Enschede by S. Wenderich, and M. K. Kruize.

2.2.1 $SrTiO_3$ substrate preparation

Prior to the growth of LAO layers on the STO substrate in the PLD chamber, the $SrTiO_3$ [001] substrates of dimensions 5 x 5 x 0.5 mm^3 are subjected to a chemical treatment, which yields a single TiO_2 terminated surface.[26,27] The as received $SrTiO_3$ substrates are cleaned in ultrasonic baths of acetone and ethanol for 15 minutes each, followed by 30 minutes in an ultrasonic bath of demi-water and 30 seconds in a buffered hydrogen fluoride solution, which results in a TiO_2 terminated surface. The TiO_2 terminated $SrTiO_3$ substrates are annealed in a pure oxygen environment at 950°C for 90 minutes to straighten the terraces.

The quality of the surface morphology of the chemically treated $SrTiO_3$ substrate is checked with atomic force microscopy (AFM). A typical AFM image of the surface morphology of good quality TiO_2 terminated $SrTiO_3$ substrate is shown in Fig. 2.2. The terraces are the result of a small miscut of the $SrTiO_3$ with respect to the (001) crystal plane. The results of the AFM scan show that all terraces in the substrate have the height of a unit cell (not half a unit cell or multiple unit cells, i.e. step bunching). Sometimes bad crystal quality results in all sorts of etch pits, which can also be clearly visible in AFM scans. After checking the STO surface using AFM scans, the good quality TiO_2 terminated single crystal STO [001] substrate is used to grow unit cells of LAO overlayers by PLD, as discussed in the following section.

2.2.2 Pulsed laser deposition

PLD is a widely used material processing technique for growing atomically sharp thin films from more than one constituent element. A typical PLD setup

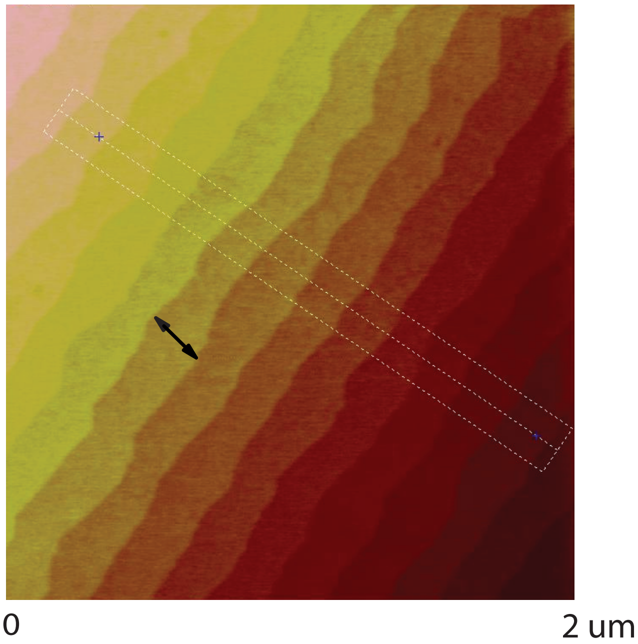

Figure 2.2: *Atomic force microscopy (AFM) image of the surface of a TiO_2-terminated $SrTiO_3$ substrate prepared by chemical and thermal treatment, the dotted lines indicate the direction of the AFM scan performed. The surface shows single unit-cell-height terraces (steps) as a result of a small miscut with respect to the [001] plane, the width of one of these terraces is represented by an arrow.*[28]

is shown schematically in Fig. 2.3. Another attractive feature of the PLD is good atomic-scale stoichiometric control in the thin-films made of complex systems, for example in high-T_c superconductors $YBa_2Cu_3O_7$, and $Bi_2Sr_2Ca_2Cu_3O_{10}$.[5,6]

PLD is therefore the most widely used technique to make LAO/STO heterostructures with atomically sharp interfaces.[29,30] The main advantage of PLD is the possibility of independently varying deposition parameters such as background oxygen pressure, substrate temperature and rate of evaporated material. This possibility enables us to fabricate LAO/STO heterostructures with different deposition conditions, thereby changing the physical properties of the interface.[31] For the growth of LAO/STO heterostructures, high purity, stoichiometric and single crystalline $LaAlO_3$ is used as the target material. For the

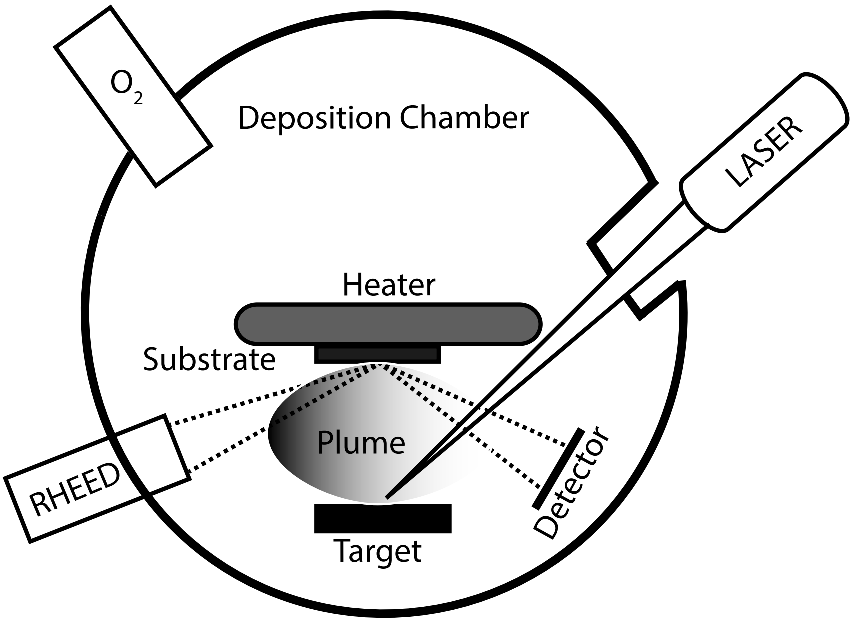

Figure 2.3: *Schematic representation of pulsed laser deposition growth setup. Reflection high-energy electron diffraction (RHEED) measures in-situ the layer-by-layer growth of the deposited film. The desired material (using single-crystalline target) film can be grown on the substrate, at various background oxygen pressures, substrate temperatures and evaporation rates of the target material.*

ablation of the $LaAlO_3$ target, a short high-energy KrF excimer laser pulse of wavelength 248 nm is used. The typical energy value of the laser pulse is about 100 mJ, with a standard deviation of about 2 mJ. The target is exposed to a laser pulse fluence (energy density) of 1.3 J/cm^2, with a spot size of 1.76 mm^2 and a repetition rate of 1 Hz. This high energy laser pulse causes sudden evaporation from the target surface and generation of a plasma plume (Fig. 2.3). This plume is composed of particles such as neutral atoms, positive and negative ions and electrons with very high kinetic energy. The interaction of the particles with the background gas leads to a thermalization of the plume and the particles reach the surface of the substrate with a strongly reduced kinetic energy and form a thin film of the target material.[32]

Our samples were grown with oxygen pressures between 10^{-2} and 10^{-6} mbar. In order to have good thermal contact, the STO substrate is glued to the heater with silver paint. The substrate is maintained at the desired temperature during deposition, typically in the range of 600 - 850°C. Using optimised deposition parameters a good quality thin film of LAO (or other desired complex oxide material) is deposited on the STO substrate and results in an LAO/STO heterostructure with an atomically sharp interface.

The thickness and quality of the deposited layer can be monitored in situ using the RHEED method as shown in Fig. 2.3.[7,8] Fig. 2.4(a) and Fig. 2.4(b) show the RHEED diffraction patterns before and after growth of the LAO layer, which are typical for STO and show a direct spot (the beam itself) and opposite to it three clear reflection/diffraction spots. The central one is the reflected spot, the side spots are the first order diffraction spots. We are interested in the intensity of the reflected spot, as the surface reflectivity is proportional to the smoothness of the surface. During growth, as parts of the new monolayer are deposited, the intensity drops until it reaches a minimum when half of the monolayer is deposited. A maximum is reached again when the monolayer is finished and the surface is very smooth again. Therefore every oscillation in the RHEED intensity plot corresponds to the growth of a single monolayer. The in situ monitored RHEED oscillation pattern for the growth of 26 unit cells of LAO overlayers on top of STO substrate is shown in the Fig. 2.4(c). This pattern shows that the 2D layer growth is preserved across the sample. Variation in the intensity of the oscillations is related to the changes in the detection method background, but is not related to the layer growth properties.

After the growth of the desired thickness of LAO, the sample is cooled to room temperature in the deposition oxygen pressure at a rate of 10°C/min. The samples used in this thesis were not subjected to any extra post-annealing procedures. The LAO/STO interface properties strongly depend on the deposition conditions like the base oxygen pressure and the substrate temperature used

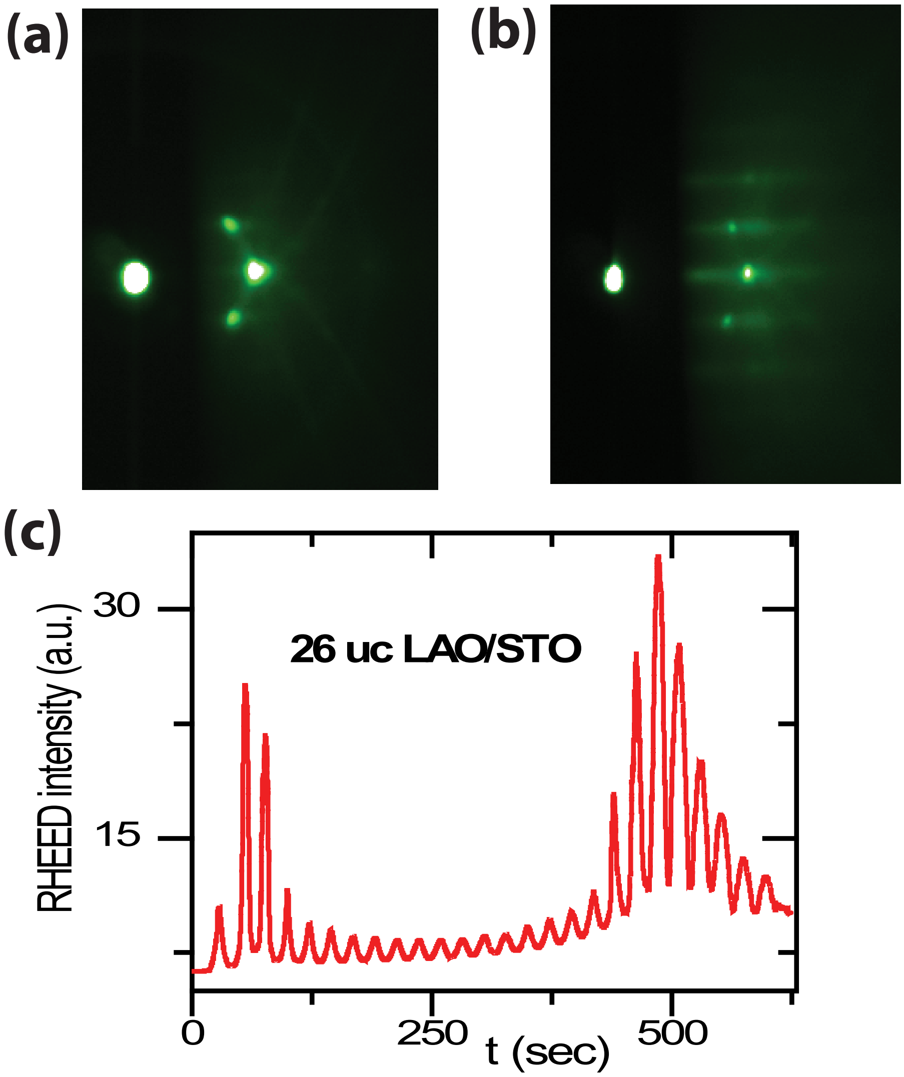

Figure 2.4: *(a) and (b) Reflection high-energy electron diffraction (RHEED) patterns for STO substrate before and after deposition of LAO layers, (c) the RHEED oscillation pattern showing the growth of 26 unit cells (uc) of LAO overlayers on STO substrate.*

during the growth of LAO overlayer. All the information about the specific deposition conditions used for the various samples is provided in the individual chapters presented in this thesis.

2.3 Magnetotransport measurements

2.3.1 Experimental procedure

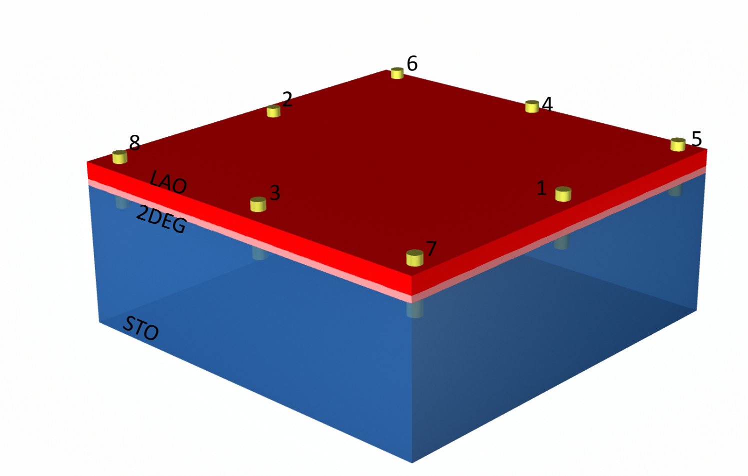

Figure 2.5: *Schematic view of an LAO/STO heterostructure with the numbered contact configuration used for the transport measurements. The contacts are made in such a way that they penetrate through 2DEG at the interface into the STO substrate.*

Magnetotransport is a powerful probe of the behaviour of free or quasi-free electrons in conventional 2D semiconductor heterostructures. Experimental results in high magnetic fields and at low-temperatures provided fundamental understanding about the properties of 2D conducting charge carriers in semiconductor heterostructures such as GaAs/AlGsAs. We apply the knowledge and expertise gained from studies of semiconductor heterostructures, in transport measurements on the new class of LAO/STO oxide heterostructures.
The LAO/STO sample was mounted on a ceramic chip carrier and ultrasonically wire-bonded using aluminium wires. The sample resistance was measured with the contacts as schematically depicted in Fig. 2.5: the resistances obtained from Ohm's law are denoted as $R_{ij,kl}$, where current is passed through the contacts i and j, and the voltage drop is measured between k and l. For a homogeneous thin-film sample with a 2D sheet of conducting electrons, the sheet resistance R_s can be obtained by applying the van der Pauw (vdP) procedure to the longitudinal resistance measured from the four corner contacts on the sample.[33] For a uniform 2D conducting sheet, the sheet resistance R_s is equal to its resistivity ρ_{xx}, which has the units of Ω (rather than Ω m in three dimensions).

We now give an example of vdP procedure on an LAO/STO heterostructure with a 26 unit cell thick LAO film, with four edge contacts numbered 5, 6, 7, 8 (Fig. 2.5), at 4.2 K when no magnetic field is applied. For performing measurements, we pass the current between the contacts 5 and 6 (I_{56}) and the voltage drop is measured across the opposite edge of the sample between the contacts 7 and 8 (V_{78}). The resistance obtained using Ohm's law in this configuration is $R_{56,78}$ (4.2 K) = 3.18 kΩ. By repeating the same procedure after changing the measurement contact configuration to I_{78} and V_{56}, the resistance obtained is $R_{78,56}$ = (4.2 K) = 3.17 kΩ. Using the same procedure with a different configuration of the same contacts we obtained the resistances $R_{75,86}$ (4.2 K) = 4.52 kΩ and $R_{86,75}$ (4.2 K) = 4.71 kΩ. The longitudinal resistance obtained for two different contact configurations is related to the sheet resistance by the vdP formula,[33] given as

$$\exp(-\frac{\pi R_{sym}}{R_s}) + \exp(-\frac{\pi R_{asym}}{R_s}) = 1, \tag{2.1}$$

where we define

$$R_{sym} = \frac{R_{56,78} + R_{78,56}}{2} = 3.18\ \mathrm{k\Omega}\ ; R_{asym} = \frac{R_{75,86} + R_{86,75}}{2} = 4.62\ \mathrm{k\Omega}. \tag{2.2}$$

Substituting Eq. 2.2 in Eq. 2.1 results in a sheet resistance R_s or resistivity ρ_{xx} = 17.46 kΩ at 4.2 K. Applying this procedure is only valid for samples with contacts made on the edges of the sample.

To measure both longitudinal resistance $R_{xx} = R_{34,75}$ and Hall resistance $R_{xy} = R_{34,12}$ at the same time in magnetotransport measurements, we chose a different contact configuration, where we passed the current across the middle contacts of the sample (1,2 or 3,4 in Fig. 2.5). This configuration measures the voltage drop along one side of the sample, which contributes to R_{xx}, and we cannot directly apply the vdP procedure to obtain ρ_{xx}. In order to obtain actual resistivity of the sample we used a simple relation $\rho_{xx} = \alpha \times R_{xx}$, where α is geometric factor of the sample. We determined the numeric ratio α between ρ_{xx} and R_{xx} for various parts of the sample where we find similar values for ρ_{xx}, which we discuss in detail in chapter 4.

Here we performed temperature-dependent magnetotransport measurements in a temperature controlled ^{4}He flow cryostat, a pumped ^{3}He system, and a dilution refrigerator, at magnetic fields up to 33 T. The electrical response of the sample was measured using a standard low-frequency lock-in technique with an excitation current in the range of nA to μA. In order to measure the sheet resistance (R_s) and Hall resistance ($R_{xy} = R_{34,12}$) in different contact configurations at the same time, instead of changing the contact configuration as in the vdP procedure (Eq. 2.2) we measured R_s and R_{xy} for both positive and negative magnetic field directions. To exclude the contribution of R_s in R_{xy} or vice versa, we symmetrized the longitudinal resistance data $((R_{xx}(+B)+R_{xx}(-B))/2)$ and antisymmetrized the Hall resistance data $((R_{xy}(+B)-R_{xy}(-B))/2)$ as with the vdP procedure.[33]

2.3.2 Magnetotransport in the classical regime

Free or quasi-free electrons in a medium with a constant relaxation time τ in an electric field $\vec{E}$, in the presence of magnetic field $\vec{B}$ applied perpendicular (z-direction) to the plane of their movement as depicted in Fig. 2.6 are described using Drude model (Eq. 2.3). This model describes the transport based on elastic collisions between electron and ionic cores, electron-electron and electron-ion interactions are neglected between collisions.[34,35] Under these conditions, the total force experienced by the free electrons is a combination of the electric (Coulomb) force (-e$\vec{E}$), the magnetic force (-e$(\vec{v}_d \times \vec{B})$), leading to the Lorentz force $-e(\vec{E}+\vec{v}_d \times \vec{B})$ and the force due to scattering $(m^*\vec{v}_d/\tau)$, where m^* is the electron effective mass, e is electronic charge and $\vec{v}_d$ is the drift velocity of the electrons, given as:

$$m^*(d\vec{v}_d/dt) = -e(\vec{E}+\vec{v}_d \times \vec{B}) - m^*\vec{v}_d/\tau. \tag{2.3}$$

The corresponding current density is $\vec{J}$ = - $ne\vec{v}_d$, where n is electron concentration. The solution for Eq. 2.3, in equilibrium $d\vec{v}_d/dt = 0$ and $\vec{B} = 0$, reduces to the simple form of Ohm's law:

$$\vec{J} = \sigma\vec{E} \qquad \text{with} \quad \sigma = \frac{ne^2\tau}{m^*}. \tag{2.4}$$

Ohm's law in this form can be used to describe microscopic electronic properties in equilibrium, where $\sigma = 1/\rho$ is the electrical conductivity.

In the presence of $\vec{B}$, the Lorentz force acts on the free carriers and results in an electric (Hall) field $\vec{E}_H$ perpendicular to the current as shown schematically in Fig. 2.6, for a 2D electron system with the magnetic field applied perpendicular to its plane. The scalar conductivity σ in Eq. 2.4 becomes a 2 × 2 tensor, written as:

$$\sigma = \frac{\sigma_0}{1+(\omega_c\tau)^2}\begin{pmatrix} 1 & -\omega_c\tau \\ \omega_c\tau & 1 \end{pmatrix}, \tag{2.5}$$

where $\omega_c = eB/m^*$ is the cyclotron frequency, $\sigma_0 = ne\mu$ is the zero field conductivity with $\mu = e\tau/m^*$, note that $\omega_c\tau = eB\tau/m^* = \mu B$.

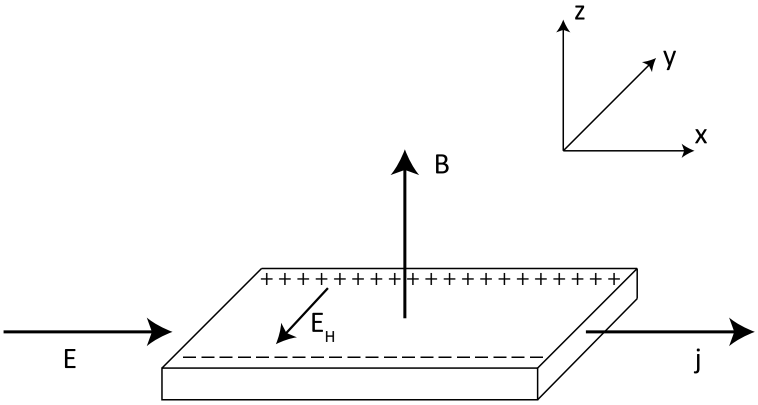

Figure 2.6: *Schematic view of the Hall effect. Electrons are subjected to the electric field $\vec{E}$ and applied magnetic field $\vec{B}$ along z-direction. The Lorentz force ($-e(\vec{E}+\vec{v}_d \times \vec{B})$ as given in Eq. 2.3) experienced by the electrons is balanced by the Hall field $\vec{E}_H$, which keeps the current density $\vec{J}$ unperturbed along x-direction.*

From the tensor inversion of σ (Eq. 2.5) the resistivity tensor can be obtained as:

$$\rho = \rho_0 \begin{pmatrix} 1 & \omega_c\tau \\ -\omega_c\tau & 1 \end{pmatrix}, \tag{2.6}$$

where $\rho_0 = 1/\sigma_0$ is the zero field resistivity.

The conductivity and resistivity components are related by the following formulas:

$$\rho_{xx} = \frac{\sigma_{xx}}{\sigma_{xx}^2+\sigma_{xy}^2} = \frac{m^*}{ne^2\tau}, \qquad \rho_{xy} = -\frac{\sigma_{xy}}{\sigma_{xx}^2+\sigma_{xy}^2} = \frac{B}{n\,|e|}. \tag{2.7}$$

or

$$\sigma_{xx} = \frac{\rho_{xx}}{\rho_{xx}^2+\rho_{xy}^2}, \qquad \sigma_{xy} = -\frac{\rho_{xy}}{\rho_{xx}^2+\rho_{xy}^2}. \tag{2.8}$$

Since the longitudinal resistivity ρ_{xx} is independent of the magnetic field (Eq. 2.7), $\rho_{xx} = \rho_0$ and depends only on the scattering time τ of the carriers. The Lorentz force acting on the free carriers under the magnetic field is balanced by the Hall field $\vec{E}_H = -\vec{B} \times \vec{v}_d$, which gives rise to a transverse resistivity component ρ_{xy} known as the Hall resistivity.[36] As a result of this compensation, the current

paths in the sample are essentially unperturbed and the longitudinal resistivity ρ_{xx} is unchanged in the magnetic field. The transverse component ρ_{xy} is linear in $\vec{B}$ and depends only on the free carrier concentration.
In an experiment we measure the components of resistivity ρ_{xx} and ρ_{xy} directly, and from the components we determine the electron density (n) and the mobility (μ) of the electron gas from Eq. 2.7,

$$n = \frac{B}{\rho_{xy}\,|e|}, \quad \mu = \frac{1}{ne\rho_0} \quad \text{or} \quad \rho_{xy} = \frac{B}{n\,|e|} = B\rho_0\mu. \tag{2.9}$$

Fig. 2.7 shows the Hall resistivity ρ_{xy} as a function of magnetic field for an LAO/STO heterostructure with a 26 unit cell thick LAO film, at 4.2 K. We extract the carrier concentration and mobility from the slope of the linear fit to the data, giving $n_{4.2K} = 8.9 \times 10^{13}$ cm^{-2} and mobility $\mu_{4.2K} = 3$ cm^2/Vs of the free carriers. Though the linear fit does not exactly start from zero like the ρ_{xy} data, slope of the fit at high magnetic field gives good estimate of the total n at 4.2 K for the interface electron system.
The validity of this simple formalism based on the Drude model is limited to charge carriers with a single relaxation time (mobility). If charge carriers with different relaxation times are present, the magnetotransport cannot be described using this model. This may arise when different types of charge carriers are present (different mobility, effective mass, or electrons and holes, or electrons from different bands). The total current density is the combination of the individual conductivities of the different channels,[37,38] and for multiple conducting channels σ can be expressed as:

$$\sigma = \begin{pmatrix} \sigma_{xx1} + \sigma_{xx2} + \sigma_{xx3} + ... & -\sigma_{xy1} - \sigma_{xy2} - \sigma_{xy3} - .... \\ \sigma_{xy1} + \sigma_{xy2} + \sigma_{xy3} + ... & \sigma_{xx1} + \sigma_{xx2} + \sigma_{xx3} + ... \end{pmatrix}. \tag{2.10}$$

The subscripts refer to the conductivities of three different types of electronic channels. In this case the Lorentz force experienced by the different types of carriers is not fully balanced by the Hall field, and transport of charge in the x direction becomes magnetic field dependent. Therefore, the measured resistivity components ρ_{xx} and ρ_{xy} are magnetic field dependent, and can be expressed as:

$$\frac{\rho_{xx}}{\rho_{xx}^2 + \rho_{xy}^2} = \sigma_{xx1} + \sigma_{xx2} + \sigma_{xx3} + ... = \frac{en_1\mu_1}{1 + (\mu_1 B)^2} + \frac{en_2\mu_2}{1 + (\mu_2 B)^2} + \frac{en_3\mu_3}{1 + (\mu_3 B)^2} + ..., \tag{2.11}$$

$$\frac{\rho_{xy}}{\rho_{xx}^2 + \rho_{xy}^2} = \sigma_{xy1} + \sigma_{xy2} + \sigma_{xy3} + ... = B(\mu_1\sigma_{xx1} + \mu_2\sigma_{xx2} + \mu_2\sigma_{xx3} + ...). \tag{2.12}$$

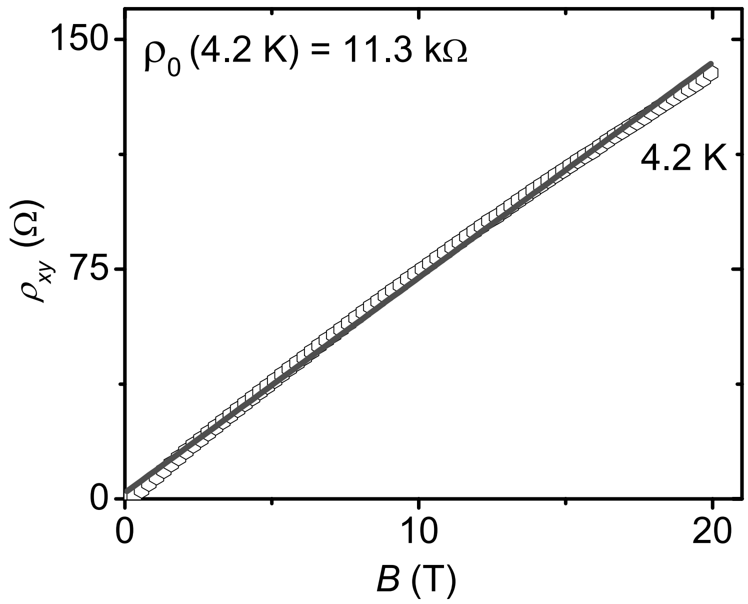

Figure 2.7: *(open symbols) Hall resistance $R_{xy} = \rho_{xy}$ data of the LAO/STO heterostructure with 26 unit cells of LAO film, as a function of magnetic field at 4.2 K, (solid line) linear fit to the experimental data.*

Solving the more complicated Eq. 2.11 and Eq. 2.12, for the case of two electronic channels with two different carrier densities (n_1 and n_2) and mobilities (μ_1 and μ_2), results in the following expressions for $\rho_{xx}(B)$ and $\rho_{xy}(B)$:[39]

$$\rho_{xx}(B) = \rho_0 \left[1 + \frac{(n_1\mu_1 n_2\mu_2(\mu_1 - \mu_2)^2 B^2)}{(n_1\mu_1 + n_2\mu_2)^2 + ((n_1 + n_2)\mu_1\mu_2 B)^2} \right], \tag{2.13}$$

$$\rho_{xy}(B) = \frac{B}{e} \frac{(n_1\mu_1^2 + n_2\mu_2^2) + (\mu_1\mu_2 B)^2(n_1 + n_2)}{(n_1\mu_1 + n_2\mu_2)^2 + (\mu_1\mu_2 B)^2(n_1 + n_2)^2}. \tag{2.14}$$

This complicated magnetic field dependence of $\rho_{xy}(B)$, $\rho_{xx}(B)$ reduces to a simpler behaviour in the extreme low field/low mobility or high field/high mobility limits. When $\mu_1 B \ll 1$ and $\mu_2 B \ll 1$, ρ_{xy} scales linearly and ρ_{xx} has a quadratic dependence on the applied magnetic field. However, when $\mu_1 B \gg 1$

and $\mu_2 B \gg 1$, ρ_{xy} shows field-linear behaviour and ρ_{xx} saturates (is field-independent). For an intermediate $\mu_1 B \ll 1$ and $\mu_2 B \simeq 1$, or vice versa, and $\rho_{xy}(B)$ shows complex non-linear behaviour as a function of magnetic field, as shown in Eq. 2.14.

This multi-band conduction occurs for the 2D electron systems in LAO/STO heterostructures in the classical magnetotransport regime, and results will be discussed in chapters 3 and 4.

2.3.3 Magnetotransport in the quantizing magnetic fields

Classical magnetotransport described by the Drude model is valid for 2D electron systems only when magnetic field induced quantization of the electronic energy levels is not important, as occurs in low magnetic fields ($\omega_c\tau < 1$) and at high temperatures ($k_B T > \hbar\omega_c$). For sufficiently high magnetic fields ($\omega_c\tau > 1$) and low temperatures ($k_B T < \hbar\omega_c$) magnetic field induced quantization of the levels cannot be neglected, and the quantum mechanical description has to be applied for 2D electron systems.

To describe magnetotransport in quantizing magnetic fields, we consider an isotropic and homogeneous 2D electron system in the xy-plane (Fig. 2.6). In this 2D electron system with confinement in the z-direction, the electronic motion in the z-direction is quantized and electrons occupy discrete energy levels E_i (subbands), and in-plane (x and y) motion is unrestricted at zero magnetic field. For 2D systems the density of states is constant in each energy level as depicted in Fig. 2.8(a), and is given by:

$$\begin{aligned} D_{2D}(E) &= \frac{m^*}{\pi\hbar^2}\sum_i \Theta(E-E_i), \\ \Theta(E-E_i) &= 0 \quad \text{for} \quad E < E_i \\ &= 1 \quad \text{for} \quad E > E_i, \end{aligned} \tag{2.15}$$

E_i is the subband energy of i^{th} state. This formula gives step-like behaviour to the constant density of states (Fig. 2.8(a)) for a 2D system.

When this 2D electron system is subjected to sufficiently high magnetic fields applied along z-direction, the cyclotron motion of electrons results in quantized energy states also in the xy-plane. The influence of magnetic field on the constant density of states of a 2D electron system at temperature $T = 0$ K is schematically illustrated in Fig. 2.8(b) and (c). The modified energy level spectrum in the xy-plane in the presence of magnetic field,[44] is given as:

$$E_N = (N+\frac{1}{2})\hbar\omega_c = (N+\frac{1}{2})\hbar\frac{eB}{m^*} \qquad (N = 0, 1, 2, 3, ...). \tag{2.16}$$

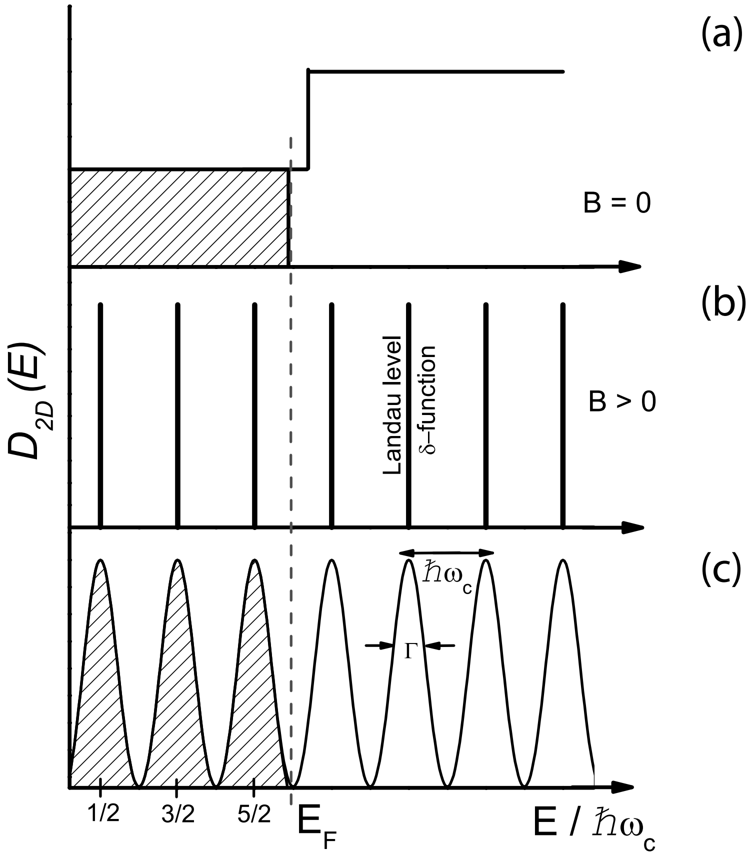

Figure 2.8: *(a) Schematic density of states for a 2D electron system (Eq. 2.15), for zero magnetic field, at* $T = 0$ *K. (b) For an ideal case (in the absence of scattering of charge carriers), in a magnetic field applied along z-direction (perpendicular to the plane of movement of charges as shown in Fig. 2.6). (c) In the presence of scattering of charge carriers, the Landau levels are broadened with width* Γ *(full width half maxima). The Landau levels are occupied up to the Fermi energy* E_F *(dashed line).*

In this solution the (Zeeman) spin splitting of the electronic levels has not been taken into account. The constant 2D density of states becomes a sequence of δ-functions (Landau levels), at energies given by Eq. 2.16, the degeneracy of each Landau level per unit area is $n_L = eB/h$, independent of the type of material or its parameters like effective mass m^*. Notice that the heavier the m^* the less separated are the Landau levels at a fixed magnetic field (as discussed in chapter 5, p.69). The so called Landau levels with a given quantum number N are degenerate.

The sharp δ-functions as shown in Fig. 2.8(b) only occur in an ideal 2D system, but when an electron typically has a finite time τ_i between scattering events, the levels are broadened by a finite width $\Gamma = \hbar/\tau_i$, as illustrated in Fig. 2.8(c). The quantum lifetime (mobility) τ_i (μ_i) is dictated by mainly small angle scattering whereas the transport (Hall) mobility μ (Eq. 2.9) is governed by wide angle scattering. The quantum lifetime τ_i determines the sharpness of quantum oscillations (discussed later in this chapter) in magnetic field, while the mobility μ determines the resistivity.

At a fixed magnetic field, Landau levels are filled up to the Fermi energy E_F (indicated as a dashed line in Fig. 2.8(c)), levels at higher energy than E_F are empty. The energy of the Landau levels increases linearly with the magnetic field resulting in a so-called *Landau fan* diagram[40] as depicted in Fig. 2.9. Typically, magnetotransport experiments are performed by keeping the total electron density n_{2D} constant, so the number of occupied Landau levels will change with the magnetic field. In a simple picture, we can consider that the Fermi energy E_F is pinned to the highest occupied Landau level (as sketched in Fig. 2.9). As the magnetic field is increased, the energy and the degeneracy of the Landau levels increases, which results in a change in the density of states D_{2D} at the Fermi level as successive Landau level energies become higher than E_F.

For the case of $\hbar\omega_c < \Gamma$ ($\omega_c\tau_i < 1$), i.e. the Landau level separation is smaller than its width, and the electron system exhibits classical behaviour as discussed in section 2.3.2. In this case, the Landau levels are “smeared out” and we do not expect to see strong changes in the density of states at the Fermi level. For the situation $\hbar\omega_c > \Gamma$ ($\omega_c\tau_i > 1$), i.e. the Landau level separation is greater than their width, the electron system exhibits well resolved quantized behaviour. In this case the electron survives for at least a complete cyclotron orbit in the magnetic field before it scatters and loses its quantum state.

Many properties of a conducting system depend primarily on the density of states near the Fermi energy (with k_BT being the thermal energy), thus the variation of D_{2D} at the Fermi energy as a function of magnetic field (Fig. 2.9) is reflected in many observable quantities, such as longitudinal resistivity ρ_{xx} and magnetic susceptibility. For the case of resistivity ρ_{xx} of a 2D electron system with moderate quantum mobility $\omega_c\tau_i > 1$ at $T = 0$ K, at low magnetic fields, the separation between the Landau levels is not large, so the change of resistivity as Landau levels pass through the Fermi energy may not be dramatic. But further increasing the magnetic field increases the separation between the neigh-

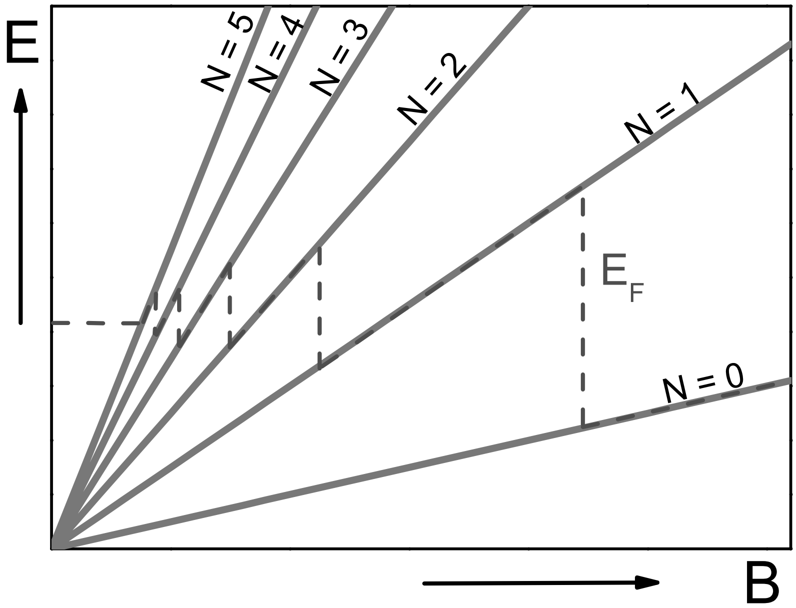

Figure 2.9: *Energy level diagram for electrons (single subband system) as a function of magnetic field only 5 Landau levels are shown. The degeneracy of Landau levels increases linearly with magnetic field. For a fixed electron density n_{2D} of the electron gas, the density of states D_{2D} oscillates at the Fermi energy E_F (dashed line) as a function of magnetic field.*[40]

bouring Landau levels and leads to strong oscillatory magnetoresistance. This type of behaviour of the electrons in high magnetic fields is called the *Shubnikov-de Haas effect* (SdH). This effect was observed experimentally for the first time in resistivity measurements of bismuth,[41] and later for a 2-dimensional electron gas in a si-MOSFET (metal oxide-semiconductor field-effect transistor).[42] SdH oscillations for various materials can be described theoretically using the following expression developed by Lifshitz and Kosevich[45] :

$$\rho_{xx}(B,T) = \frac{m^*}{ne^2\tau}\left[1 - 2e^{-\pi/\omega_c\tau_i}\ \frac{2\pi^2 k_B T/\hbar\omega_c}{\sinh(2\pi^2 k_B T/\hbar\omega_c)}\ \cos(2\pi\frac{hn}{2eB}+\phi)\right]. \tag{2.17}$$

The prefactor is the magnetic-field-independent longitudinal resistivity (Eq. 2.7) and the rest of the expression in square brackets describes the SdH oscillations with $1/B$-periodicity. The temperature dependent factor $2\pi^2 k_B T/\hbar\omega_c/\sinh(2\pi^2 k_B T/\hbar\omega_c)$ reduces the amplitude of the oscillations as a result of energy averaging over $k_B T$ around the Fermi energy. The exponential term $e^{-\pi/\omega_c\tau_i}$ accounts for the finite lifetime broadening of the Landau levels in the form of the Dingle temperature, expressed as $T_D = (e\hbar/2\pi k_B)(1/m^*\mu_i)$. From the analysis of SdH oscillations using Eq. 2.17, properties of a 2D electron system, such as the carrier concentration n_{2D}, the quantum lifetime τ_i and the electron effective mass m^*, can be obtained.

For a strictly 2D electron system, according to the cosine term $\cos(2\pi hn/2eB)$ of Eq. 2.17, the periodicity (frequency) of the SdH oscillations depends on the out-of-plane magnetic field component (i.e., increasing the angle between surface normal and applied magnetic field changes the periodicity of the oscillations by in-situ rotating the sample). It is quite common to measure the angular dependence of SdH oscillations, which is a powerful tool to verify 2D nature of the conduction electron gas in various new materials.[3,21,22,43] The frequency F of the oscillations is related to the cross-section area A of the Fermi-surface in a plane normal to the magnetic field by the Onsager relation[46] given as:

$$F = \frac{\hbar A}{2\pi e}. \tag{2.18}$$

For example, we have performed (outside of my main PhD project) angular dependence magnetotransport on patterned Bi_2Te_3 flakes to verify the dimensionality of the conduction electron system residing on its surface, in collaboration with M. Veldhorst and A. Brinkman from University of Twente. We show a part of the experimental results in Fig. 2.10 and details about the analysis of SdH oscillations using Eq. 2.17 are published in reference 47.

As we discussed (Eq. 2.17) for a 2D electron system, the periodicity (frequency) of the SdH oscillations depends on the out-of-plane magnetic field component. It can be seen in Fig. 2.10 that the oscillation maxima follow the expected shift (indicated as connected squares in Fig. 2.10) as the out-of-plane magnetic field, $B_\perp = B\cos(\theta)$, is increased. These measurements confirm the 2D nature of the electron transport in Bi_2Te_3 flakes originating from the surface states.

For the 2D electron systems with more than one occupied subband, the oscillation maxima deviate from the expected shift given by, $B_\perp = B\cos(\theta)$, and show complex periodicity, and is caused by the superposition of the frequency of the oscillations from different subbands. Multiple subband conduction occurs in the 2D electron gas present in LAO/STO heterostructures, the detailed procedure for analysis of such SdH oscillations originating from multiple 2D subbands is discussed later in chapter 5.

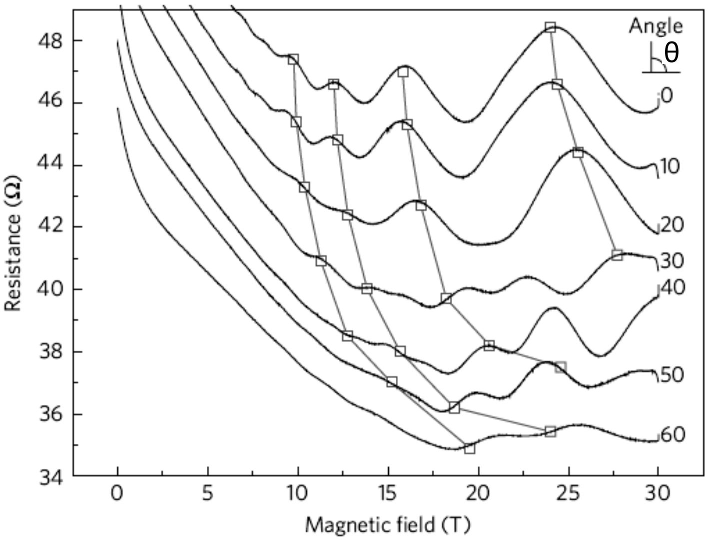

Figure 2.10: *Magnetic field-orientation-dependence of the Shubnikovde Haas oscillations from* Bi_2Te_3 *surface states, at 4.2 K, after subtraction of a linear background. The angle* θ *between the magnetic field direction and the surface normal is shown beside each of the curves. The square markers represent the expected shift of the maxima in magnetic field for a 2D system, given by* $B_\perp = B\cos(\theta)$*, indicating that the oscillations arise from 2D surface states.*[47]

References

[1] Zhores I. Alferov, Zhores I. Alferov, Rev. Mod. Phys. **73**, 767 (2001).

[2] V. Umansky, M. Heiblum, Y. Levinson, J. Smet, J. Nübler, and M. Dolev, J. Cryst. Growth **311**, 1658 (2009).

[3] A. Tsukazaki, A. Ohtomo, T. Kita, Y. Ohno, H. Ohno, and M. Kawasaki, Science **315**, 1388 (2007).

[4] A. Tsukazaki, S. Akasaka, K. Nakahara, Y. Ohno, H. Ohno, D. Maryenko, A. Ohtomo, and M. Kawasaki, Nat. Mater. **9**, 889 (2010).

[5] D. Dijkkamp, T. Venkatesan, X. D. Wu, S. A. Shaheen, N. Jisrawi, Y. H. Min-lee, W. L. Mclean, and M. Croft, Appl. Phys. Lett. **51**, 619 (1987).

[6] I. Bozovic and J. N. Eckstein, Appl. Surf. Sci. **113/114**, 189 (1998).

[7] H. Karl and B. Stritzker, Phys. Rev. Lett. **69**, 2939 (1992).

[8] G. J. H. M. Rijnders, G. Koster, D. H. A. Blank, and H. Rogalla, Appl. Phys. Lett. **70**, 1888 (1997).

[9] H. Y. Hwang, Y. Iwasa, M. Kawasaki, B. Keimer, N. Nagaosa, and Y. Tokura, Nature Mater. **11**, 103 (2012).

[10] A. Ohtomo, D. A. Muller, J. L. Grazul, and H. Y. Hwang, Nature **419**, 378 (2002).

[11] A. Ohtomo and H. Y. Hwang, Nature **427**, 423 (2004).

[12] N. Reyren, S. Thiel, A. D. Caviglia, L. F. Kourkoutis, G. Hammerl, C. Richter, C. W. Schneider, T. Kopp, A. S. Ruetschi, D. Jaccard, M. Gabay, D. A. Muller, J.-M. Triscone, and J. Mannhart, Science **317**, 1196 (2007).

[13] A. Brinkman, M. Van Zalk, J. Huijben, U. Zeitler, J. C. Maan, W. G. Van der Wiel, G. Rijnders, D. H. A. Blank, and H. Hilgenkamp, Nature Mater. **6**, 493 (2007).

[14] M. Ben Shalom, C. W. Tai, Y. Lereah, M. Sachs, E. Levy, D. Rakhmilevitch, A. Palevski, and Y. Dagan, Phys. Rev. B **80**, 140403 (2009).

[15] Ariando, X. Wang, G. Baskaran, Z. Q. Liu, J. Huijben, J. B. Yi, A. Annadi, A. R. Barman, A. Rusydi, S. Dhar, Y. P. Feng, J. Ding, H. Hilgenkamp, and T. Venkatesan, Nature Comm. **2**, 188 (2011).

[16] A. D. Caviglia, S. Gariglio, N. Reyren, D. Jaccard, T. Schneider, M. Gabay, S. Thiel, G. Hammerl, J. Mannhart, and J.-M. Triscone, Nature (London) **456**, 624 (2008).

[17] C. Cen, S. Thiel, G. Hammerl, C. W. Schneider, K. E. Andersen, C. S. Hellberg, J. Mannhart, and J. Levy, Nat. Mater. **7**, 298 (2008).

[18] S. Thiel, G. Hammerl, A. Schmehl, C. W. Schneider, and J. Mannhart, Science **313**, 1942 (2006).

[19] V. K. Guduru, A. Granados del Aguila, S. Wenderich, M. K. Kruize, A. McCollam, P. C. M. Christianen, U. Zeitler, A. Brinkman, G. Rijnders, H. Hilgenkamp, and J. C. Maan, Appl. Phys. Lett. **102**, 051604 (2013).

[20] M. Ben Shalom, A. Ron, A. Palevski, and Y. Dagan, Phys. Rev. Lett. **105**, 206401 (2010).

[21] A. D. Caviglia, S. Gariglio, C. Cancellieri, B. Sacepe, A. Fete, N. Reyren, M. Gabay, A. F. Morpurgo, and J.-M. Triscone, Phys. Rev. Lett. **105**, 236802 (2010).

[22] A. McCollam, S. Wenderich, M. K. Kruize, V. K. Guduru, H. J. A. Molegraaf, M. Huijben, G. Koster, D. H. A. Blank, G. Rijnders, A. Brinkman, H. Hilgenkamp, U. Zeitler, and J. C. Maan, Appl. Phys. Lett.: Materials **2**, 022102 (2014).

[23] D. A. Dikin, M. Mehta, C. W. Bark, C. M. Folkman, C. B. Eom, and V. Chandrasekhar, Phys. Rev. Lett. **107**, 056802 (2011).

[24] L. Li, C. Richter, J. Mannhart, and R. C. Ashoori, Nature Phys. **7**, 762 (2011).

[25] J. A. Bert, B. Kalisky1, C. Bell, M. Kim, Y. Hikita, H. Y. Hwang, and K. A. Moler, Nature Phys. **7**, 767 (2011).

[26] M. Kawasaki, K. Takahashi, T. Maeda, R. Tsuchiya, M. Shinohara, O. Ishiyama, T. Yonezawa, M. Yoshimoto, and H. Koinuma, Science **266**, 1540 (1994).

[27] G. Koster, B. L. Kropman, G. J. H. M. Rijnders, D. H. A. Blank, and H. Rogalla, Appl. Phys. Lett. **73**, 2920 (1998).

[28] This AFM image is taken at MESA+ Institute for Nanotechnology in Enschede by S. Wenderich.

[29] N. Nakagawa, H. Y. Hwang, and D. A. Muller, Nature Mater. **5**, 204 (2006).

[30] M. Huijben, G. Rijnders, D. H. A Blank, S. Bals, S. van Aert, J. Verbeeck, G. van Tendeloo, A. Brinkman, and H. Hilgenkamp, Nature Mater. **5**, 556 (2006).

[31] M. Huijben, A. Brinkman, G. Koster, G. Rijnders, H. Hilgenkamp, and D. H. A Blank, Adv. Mater. **21**, 1665 (2009).

[32] P. R. Willmott and J. R. Huber, Rev. Mod. Phys **72**, 315 (2000).

[33] L. J. van der Pauw, Philips Res. Repts **13**, 1 (1958).

[34] P. Drude, Ann. d. Phys. **306**, 566 (1900).

[35] P. Drude, Ann. d. Phys. **308**, 369 (1900).

[36] E. H. Hall, Am. J. Mathematics **2**, 287 (1879).

[37] H. van Houten, J. G. Williamson, M. E. I. Broekaart, C. T. Foxon, and J. J. Harris, Phys. Rev. B **37**, 2756 (1988).

[38] S. J. Battersby, F. M. Selten, J. J. Harris, and C. T. Foxon, Solid-State Electronics **31**, 1083 (1998).

[39] N. W. Ashcroft and N. D. Mermin, *Solid State Physics* (Harcourt Brace College Publishers, 1976) page number 240.

[40] T. Ihn, *Semiconductor Nanostructures: Quantum States and Electronic Transport* (Oxford University Press, 2010) p 291.

[41] L. Shubnikov and W. J. de Haas, Leiden Commun. **207a** (1930).

[42] A. B. Fowler, F. F. Fang, W. E. Howard, and P. J. Stiles, Phys. Rev. Lett. **16**, 901 (1966).

[43] Y. Kozuka, M. Kim, C. Bell, B. G. Kim, Y. Hikita, and H. Y. Hwang, Nature **462**, 487 (2009).

[44] L. D. Landau, Z. Phys **64**, 629 (1930). Vector potential A $= (0, Bx, 0)$.

[45] I. M. Lifshitz and A. M. Kosevich, Sov. Phys. JETP **2**, 636 (1956).

[46] D. Shoenberg *Magnetic Oscillations in Metals* (Cambridge University Press, 1984) p 23.

[47] M. Veldhorst, M. Snelder, M. Hoek, T. Gang, V. K. Guduru, X. L. Wang, U. Zeitler, W. G. Van der Wiel, A. A. Golubov, H. Hilgenkamp, and A. Brinkman, Nature Mater. **11**, 417 (2012).

Chapter 3

Optically excited multi-band conduction in $LaAlO_3/SrTiO_3$ heterostructures

Abstract

The low-temperature resistance of a conducting $LaAlO_3/SrTiO_3$ *interface with a 10 nm* $LaAlO_3$ *film decreases by more than 50% after illumination with light of energy higher than the* $SrTiO_3$ *band-gap. We explain our observations by optical excitation of an additional high mobility electron channel, which is spatially separated from the photo-excited holes. After illumination, we measure a strongly non-linear Hall resistance which is governed by the concentration and mobility of the photo-excited carriers. This can be explained within a two-carrier model where illumination creates a high mobility electron channel in addition to a low mobility electron channel which exists before illumination.*

This chapter is based on work published in: V. K. Guduru et al., Applied Physics Letters **102**, 051604 (2013).

3.1 Introduction

A conducting interface[1] between band-insulating perovskite oxides $LaAlO_3$ (LAO) and $SrTiO_3$ (STO) displays a wide variety of physical phenomena, such as superconductivity,[2] magnetism,[3–8] and quantum oscillations with 2D character.[9–11] Several mechanisms are suggested to describe the origin of conductivity at the LAO/STO interface.[12–17] However, the relative contribution of each mechanism appears to depend on the LAO film thickness and on the LAO growth conditions such as substrate temperature, oxygen partial pressure and the post annealing treatment, and the complete picture of the involved mechanisms is not yet clear.[18] In particular, growing 5-10 layers of LAO on STO yields a metallic interface with relatively high mobility and low electron concentration,[19,20] whereas growing 26 LAO layers with the same conditions results in a low mobility, high concentration electron system with interesting magnetic properties.[3] Tuning the transport properties at such a complex oxide interface by modulating the carrier density with light can both contribute to the understanding of its physics and open new pathways towards oxide-based optoelectronic device applications. It has been shown previously that interface conductivity in oxide heterostructures can be tuned by light or by an electric field.[21–25]

This chapter describes our investigation of the interface of a LAO/STO sample with 26 monolayers of LAO, using low-temperature (4.2 K) magnetotransport experiments under selective illumination. The temperature-dependent magnetotransport performed in a wide temperature range (0.3 K to 300 K) and at high magnetic fields are discussed in more detail in chapter 4. Illuminating the sample with UV light of energy greater than the STO band gap results in a sharp and persistent decrease of electrical resistance. Using Hall effect measurements, we show that before illumination there is a single, low mobility electron conduction band, and that a sharp drop in resistance upon illumination can be explained by a parallel conducting channel containing optically excited high mobility electrons.

3.2 Sample preparation and experimental set-up

Our sample was grown by pulsed laser deposition (PLD) and has a 10 nm thick (26 unit cells) LAO film on a TiO_2-terminated single crystal STO [001] substrate (treatment described in Ref. 26). More details about the general growth procedure involved in making the LAO/STO heterostructures were discussed in chapter 2 (section 2.2). Specifically for this sample, the LAO film was deposited at a substrate temperature of 850°C and an oxygen pressure of 2×10^{-3}

mbar, using a single-crystal $LaAlO_3$ target. The growth of the LAO film was monitored using in situ reflection high-energy electron diffraction. After the growth, samples were cooled to room temperature in the deposition pressure. The fabrication LAO/STO heterostructure and atomic force microscopy was performed at MESA+ Institute for Nanotechnology in Enschede.

The sample was mounted on a ceramic chip carrier and electrical contacts were made with an ultrasonic wire-bonder, using aluminium wires. The magnetoresistance and Hall resistance were measured at 4.2 K in a van der Pauw geometry, using a standard low-frequency lock-in technique with an excitation current of 1 μA. The detailed van der Pauw procedure used to perform magnetotransport are discussed in chapter 2 (section 2.3.1). The temperature dependence of the sample resistance shows a low-temperature upturn, similar to that observed previously by *Brinkman et al.*[3] The sample was illuminated with light from a broad-band Xe-lamp (LSB521), which was filtered using a 30 cm single grating monochromator (Acton-SP2300) as well as longpass and bandpass filters, to tune the excitation energy. The obtained quasi monochromatic light ($\Delta\lambda \simeq 3$ nm) was brought to the sample via an optical fiber.

3.3 Experimental results and discussion

Fig. 3.1 shows the raw data of sample resistance as a function of time during light illumination in the energy range between 1.44 and 3.65 eV. Each step corresponds to a constant illumination with a specific energy during 1 minute (light ‘ON’). After illumination, we waited for 10 minutes to allow the resistance to reach a reasonably stable value (light ‘OFF’), before illuminating with the next photon energy. The influence of photons with different energy is clearly seen as a series of steps in the sample resistance. When the energy of illuminating photons is smaller than the band gap of STO (3.4 eV), a small resistance decrease is observed. This small change in the sample resistance can be due to the finite absorption of incident illumination by in-gap states present inside the STO band gap.[27,28] When the photon energy is approaching the band gap of STO, there is a gradual increase in the change of sample resistance. The largest drop in resistance (more than 50%), occurs when the photon energy (3.65 eV) exceeds the STO band gap energy (3.4 eV). This dramatically reduced resistance does not recover to the initial value after the illumination is turned off, and only returns to the previous value when the sample is heated to room temperature and cooled back to 4.2 K. Repeated thermal cycling of the sample gave reproducible results.

We also performed a control experiment on a STO [001] substrate, which was

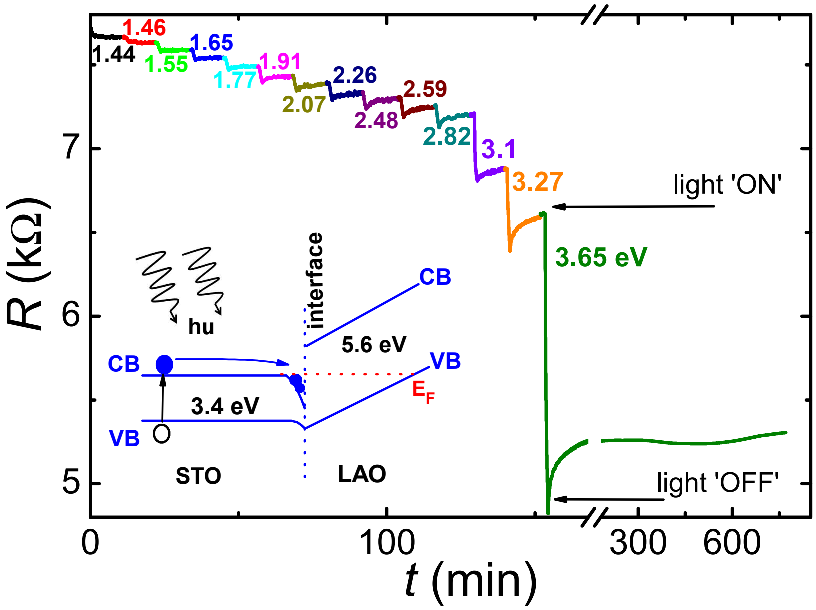

Figure 3.1: *Sample resistance as a function of time during the illumination with photons of energy from 1.44 to 3.65 eV at 4.2 K. Each change in the photon energy results in a pronounced step in the sample resistance; the photon energies, in eV, are shown beside each of the steps. The inset shows a schematic band diagram (CB-conduction band, VB-valence band and E_F-Fermi-level) for a LAO/STO heterostructure under illumination. Note the break on the time-axis showing the persistence of the resistance change*

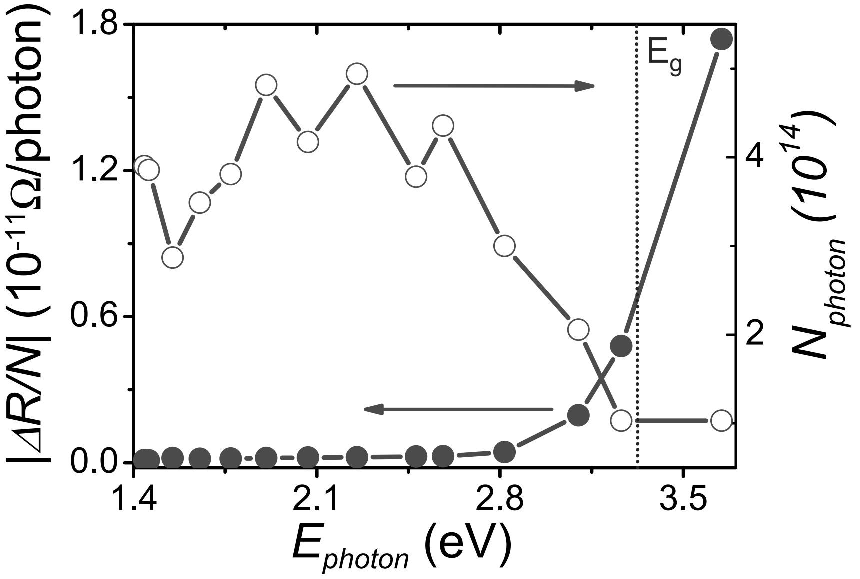

Figure 3.2: *Total number of photons at the sample as a function of photon energy is shown in open circles (right axis). Normalized sample resistance as a function of the energy of illuminating photons is shown in solid circles (left axis). The connecting lines are a guide to the eye.*

subjected to a similar chemical etching and annealing treatment (described in Ref. 26). The TiO_2-terminated bulk STO [001] substrate was heated to a temperature of 850°C at an oxygen pressure of 2×10^{-3} mbar in the PLD chamber, without depositing the LAO layer. When contacting this treated control sample with similar contact configuration as the LAO/STO interface, and illuminating it under similar illumination conditions as the interface, we found that it remains insulating for all photon energies. This proves that the persistent resistance decrease is a feature of the LAO/STO interface and not an effect from the treated bulk STO [001] substrate.

In Fig. 3.2, we show, as open circles (right axis), the variation in the number of illuminating photons as a function of photon energy, which is a consequence of the energy-dependent throughput of the optical set-up. The number of photons at the sample was calculated from the integration over time of the total power incident on the sample, normalized with the energy of a single photon. The solid circles (left axis) show the resistance change of the sample, normalized by the number of incident photons, at each photon energy. The most drastic change occurs when the photon energy is higher than the STO band gap, shown as the vertical dashed line in figure.

In order to explain these results, we propose the generation of additional, photo-excited carriers, as depicted in the inset of Fig. 3.1: Illuminating either the bulk STO (control sample) or the LAO/STO heterostructure with photon energy higher than the band gap of STO, creates electron-hole pairs in the STO substrate. In the case of bulk STO, the photo-excited electrons in the empty conduction band do not persist for a long time and recombine very quickly with holes in the valence band, or through other recombination centres. For the case of the LAO/STO heterostructure, the photo-excited electrons move to the interface potential well, where the holes remain trapped in the substrate. Owing to this spatial separation, electron and hole wavefunctions do not overlap and direct optical recombination is suppressed, leading to a persistent resistance change.

For the LAO/STO heterostructure, the confinement potential for photo-excited carriers lifts the degeneracy of the STO bulk bands (Ti-3d xy, yz and xz bands) and a further formation of 2D subbands is expected due to spin-orbit coupling and the internal electric field due to growth of LAO layers.[29] The 2D interface potential well gives a multi-subband character to the STO conduction band at the interface of LAO/STO.[11] Owing to this multi-subband structure of the interface, we propose that the photo-excited carriers occupy an initially unoccupied subband with a high mobility.

To study the nature of the persistent photo-excited carriers, we have performed magnetotransport experiments after illumination with an increasing total number of photons N_{tot}, controlled with neutral density filters, at a constant photon energy of 3.65 eV. In Fig. 3.3(a), we show the Hall resistance R_{xy} as a function of applied magnetic field B at 4.2 K, before illumination and after illuminating with four different values of N_{tot} (open symbols). The corresponding (longitudinal) magnetoresistance is shown in Fig. 3.3(b). Without any illumination, a linear Hall resistance and a small negative magnetoresistance are observed, in agreement with earlier observations on a similar sample.[3] After illumination, a distinctly non-linear Hall resistance and a large positive magnetoresistance appear. In order to explain the experimental data, we use the concepts of magnetotransport in the classical regime (section 2.3.2) as described in chapter 2.

We describe the linear Hall resistance using the conventional single-carrier model, and extract the carrier concentration ($n = B/R_{xy}e$) and mobility ($\mu = 1/\rho_0 en$) from the slope of the linear fit to the data - the fit is shown as a solid line in Fig. 3.3(a), where ρ_0 is the zero field sheet resistance, and e is the elec-

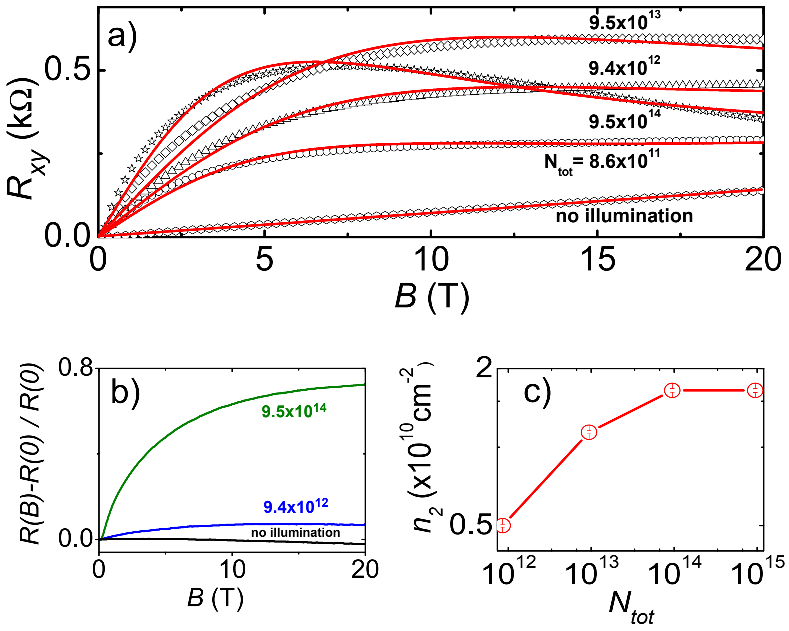

Figure 3.3: *(a) Hall resistance data as a function of the applied magnetic field, for illumination with different values of* N_{tot} *with energy of 3.65 eV at 4.2 K (open symbols). (solid lines) The two-band model (Eq. 3.1) fits to the experimental data. (b) (longitudinal) Magnetoresistance data as a function of the applied magnetic field and (c) carrier concentration of the second, high mobility band for illumination with different values of* N_{tot}.

tronic charge. This yields a carrier density $n_1 = 8.9 \times 10^{13}$ cm^{-2} and a mobility $\mu_1 = 3$ cm^2/Vs. This very low carrier mobility is similar to values previously observed in LAO/STO samples with comparable LAO layer thickness.[3,30]

In contrast, the non-linear Hall resistance after illumination cannot be explained within a single-carrier model, but rather suggests a multi-channel system. A similar non-linear Hall resistance was observed previously in LaTiO$_3$/SrTiO$_3$,[31,32] and explained in terms of two-channel conduction from electronic bands with different mobilities, μ_1 and μ_2, and carrier densities, n_1 and n_2. We use a similar, simple two-electron-band expression for R_{xy}, given by[33]

$$R_{xy} = \frac{B}{e}\frac{(n_1\mu_1^2 + n_2\mu_2^2) + (\mu_1\mu_2 B)^2(n_1 + n_2)}{(n_1\mu_1 + n_2\mu_2)^2 + (\mu_1\mu_2 B)^2(n_1 + n_2)^2}, \tag{3.1}$$

to model our Hall resistance data after illumination.

In this expression, we take n_1 and μ_1 to be the carrier density and mobility of the existing electron band without illumination, and n_2 and μ_2 are the carrier density and mobility of the persistent, photo-excited high mobility band. For low magnetic fields where $\mu_1 B \ll 1$ and $\mu_2 B \ll 1$, and for high magnetic fields where $\mu_1 B \gg 1$ and $\mu_2 B \gg 1$, expression (3.1) is linear in magnetic field; $R_{xy}(B)$ becomes non-linear where $\mu_2 B \simeq 1$. This simple two-band model is not able to reproduce all the details of the magnetotransport in our sample, but the fact that we observe a non-linear Hall resistance (as described in section 2.3.2) at a few Tesla clearly points towards the existence of an optically excited high mobility channel.

The results of our two-band analysis are shown in Fig. 3.3(a) as solid lines. We fitted the non-linear Hall resistance for $N_{tot} = 8.6 \times 10^{11}$, using n_2 and μ_2 as fit parameters, and with fixed values of $n_1 = 8.9 \times 10^{13}$ cm^{-2} and $\mu_1 = 3$ cm^2/Vs (as extracted from the linear Hall resistance before illumination): values of $n_2 = 0.5 \times 10^{10}$ cm^{-2} and $\mu_2 = 1200$ cm^2/Vs were obtained. For the higher values of N_{tot} we found that the quality of the fits was insensitive to small variations in μ_2 around this value of 1200 cm^2/Vs. We therefore fixed $\mu_2 = 1200$ cm^2/Vs and used only n_2 as a fit parameter for the higher values of N_{tot}. The values of n_2 extracted in this way are shown in Fig. 3.3(c). For the highest value of N_{tot}, a good fit to R_{xy} required a slightly increased value of n_1 from 8.9×10^{13} cm^{-2} to 1.19×10^{14} cm^{-2}, with an unchanged value of n_2 (as shown in Fig. 3.3(c)). This two-band analysis of the Hall resistance strongly suggests that we populate a second high mobility electron channel by illumination above the STO band-gap. This observed relatively high mobility (1200 cm^2/Vs) of the persistently photo-excited electrons is similar to the values previously observed in reduced or non-stoichiometric bulk STO.[28,34–36] The fact that we see comparable high mobility values for photo-excited carriers, suggest that the influence of interface defects is not so crucial in this case. A surface morphology study of the STO [001] substrate using an atomic force microscope (Fig. 2.2), prior to growth of the LAO layer did not reveal any macroscopic defects.

3.4 Summary and Outlook

In summary, we have measured magnetotransport in a LAO/STO heterostructure, with a 10 nm LAO film, after illumination with selective photon energy.

When the photon energy exceeds the STO band gap, the low-temperature resistance decreases by more than 50% and remains persistent at the lower value. We explain this effect in terms of optical excitation of an additional high mobility electron channel, which is spatially separated from the photo-excited holes, and confirm the presence of a second conducting electron band through measurement of a strongly non-linear Hall resistance after illumination. A two-carrier description of the Hall resistance data after illumination shows one low mobility (3 $\mathrm{cm}^2/\mathrm{Vs}$) band with a high carrier density ($\simeq 10^{14}$ cm^{-2}) corresponding to the original conduction band present before illumination, and one persistently photo-excited high mobility (1200 $\mathrm{cm}^2/\mathrm{Vs}$) band with a low carrier density ($\simeq 10^{10}$ cm^{-2}). We suggest that these persistently photo-excited carriers occupy one of the interface 2D subbands in STO, where these carriers have relatively higher mobility than the existing low mobility carriers without illumination.

We have shown that measuring magnetotransport properties after UV illumination is a simple measurement technique, and can be used to study the properties of the LAO/STO interface carriers and bandstructure in a way that gives results which are relatively easy to interpret and intuitive. It is therefore a promising way of examining these properties in other LAO/STO related heterostructures that shows different and interesting behaviour such as electric field-effect modulation of interface carrier density,[25] superconductivity[2] and Kondo effect.[3] A logical follow up of these experiments would be performing magnetotransport on field-effect devices based on LAO/STO heterostructures, analogous to the device configuration of the conventional metal-oxide semiconductor field effect transistor. In the field-effect devices the photo-excited interface carriers (after UV illumination) can be systematically tuned (addition or removal) by applying a backgate voltage (positive or negative) using the STO substrate as a gate dielectric. Such measurements could provide further information about the nature (electrons or holes) of interface charge carriers contributing to the transport. Another interesting property of LAO/STO interface is the on-off switching of its superconducting state as a function of the interface carrier density.[25] Using our present UV-illumination technique, we can systematically tune in the charge carrier density at such superconducting LAO/STO interface as a function of N_{tot}, and there by switching on-off the superconducting state in a simpler manner than earlier reports.[25] One of the interesting property of the LAO/STO interface is its magnetic nature in close resemblance to Kondo-effect. This effect arises typically in a metal due to the scattering of conduction electrons with the magnetic impurities. The emergence of the Kondo-effect at the LAO/STO interface found to be a function of the conduction charge carrier density,[19] similar behaviour is also observed for the surface 2-dimensional electron system present on bulk STO.[37] With our presented technique we can change charge carrier density systematically as a function of N_{tot}, and there by the its influence on the Kondo-effect. This kind of measurements could provide further information about the magnetic behaviour of LAO/STO interface.

References

[1] A. Ohtomo and H. Y. Hwang, Nature (London) **427**, 423 (2004).

[2] N. Reyren, S. Thiel, A. D. Caviglia, L. F. Kourkoutis, G. Hammerl, C. Richter, C. W. Schneider, T. Kopp, A. S. Ruetschi, D. Jaccard, M. Gabay, D. A. Muller, J.-M. Triscone, and J. Mannhart, Science **317**, 1196 (2007).

[3] A. Brinkman, M. Van Zalk, J. Huijben, U. Zeitler, J. C. Maan, W. G. Van der Wiel, G. Rijnders, D. H. A. Blank, and H. Hilgenkamp, Nature Mater. **6**, 493 (2007).

[4] M. Ben Shalom, C. W. Tai, Y. Lereah, M. Sachs, E. Levy, D. Rakhmilevitch, A. Palevski, and Y. Dagan, Phys. Rev. B **80**, 140403 (2009).

[5] Ariando, X. Wang, G. Baskaran, Z. Q. Liu, J. Huijben, J. B. Yi, A. Annadi, A. R. Barman, A. Rusydi, S. Dhar, Y. P. Feng, J. Ding, H. Hilgenkamp, and T. Venkatesan, Nature Comm. **2**, 188 (2011).

[6] D. A. Dikin, M. Mehta, C. W. Bark, C. M. Folkman, C. B. Eom, and V. Chandrasekhar, Phys. Rev. Lett. **107**, 056802 (2011).

[7] L. Li, C. Richter, J. Mannhart, and R. C. Ashoori, Nature Phys. **7**, 762 (2011).

[8] J. A. Bert, B. Kalisky, C. Bell, M. Kim, Y. Hikita, H. Y. Hwang, and K. A. Moler, Nature Phys. **7**, 767 (2011).

[9] M. Ben Shalom, A. Ron, A. Palevski, and Y. Dagan, Phys. Rev. Lett. **105**, 206401 (2010).

[10] A. D. Caviglia, S. Gariglio, C. Cancellieri, B. Sacepe, A. Fete, N. Reyren, M. Gabay, A. F. Morpurgo, and J.-M. Triscone, Phys. Rev. Lett. **105**, 236802 (2010).

[11] A. McCollam, S. Wenderich, M. K. Kruize, V. K. Guduru, H. J. A. Molegraaf, M. Huijben, G. Koster, D. H. A. Blank, G. Rijnders, A. Brinkman, H. Hilgenkamp, U. Zeitler, and J. C. Maan, Appl. Phys. Lett.: Materials **2**, 022102 (2014).

[12] N. Nakagawa, H. Y. Hwang, and D. A. Muller, Nature Mater. **5**, 204 (2006).

[13] K. Yoshimatsu, R. Yasuhara, H. Kumigashira, and M. Oshima, Phys. Rev. Lett. **101**, 026802 (2008).

[14] M. Sing, G. Berner, K. Goß, A. Müller, A. Ruff, A. Wetscherek, S. Thiel, J. Mannhart, S. A. Pauli, C. W. Schneider, P. R. Willmott, M. Gorgoi, F. Schäfers, and R. Claessen, Phys. Rev. Lett. **102**, 176805 (2009).

[15] W. Siemons, G. Koster, H. Yamamoto, W. A. Harrison, G. Lucovsky, T. H. Geballe, D. H. A. Blank, and M. R. Beasley, Phys. Rev. Lett. **98**, 196802 (2007).

[16] G. Herranz, M. Basleti, M. Bibes, C. Carretero, E. Tafra, E. Jacquet, K. Bouzehouane, C. Deranlot, A. Hamzi, J.-M. Broto, A. Barthelemy, and A. Fert, Phys. Rev. Lett. **98**, 216803 (2007).

[17] P. R. Willmott, S. A. Pauli, R. Herger, C. M. Schleptz, D. Martoccia, B. D. Patterson, B. Delley, R. Clarke, D. Kumah, C. Cionca, and Y. Yacoby, Phys. Rev. Lett. **99**, 155502 (2007).

[18] M. Huijben, A. Brinkman, G. Koster, G. Rijnders, H. Hilgenkamp, and D. H. A Blank, Adv. Mater. **21**, 1665 (2009).

[19] C. Bell, S. Harashima, Y. Hikita, and H. Y. Hwang, Appl. Phys. Lett. **94**, 222111 (2009).

[20] F. J. Wong, R. V. Chopdekar and Y. Suzuki, Phys. Rev. B **82**, 165413 (2010).

[21] A. Rastogi, A. K. Kushwaha, T. Shiyani, A. Gangawar, and R. C. Budhani, Adv. Mater. **22**, 4448 (2010).

[22] A. Rastogi, J. J. Pulikkotil, S. Auluck, Z. Hossain, and R. C. Budhani, Phys. Rev. B **86**, 075127 (2012).

[23] A. Tebano, E. Fabbri, D. Pergolesi, G. Balestrino, and E. Traversa, AcsNANO **6**, 1278 (2012).

[24] S. Thiel, G. Hammerl, A. Schmehl, C. W. Schneider, and J. Mannhart, Science **313**, 1942 (2006).

[25] A. D. Caviglia, S. Gariglio, N. Reyren, D. Jaccard, T. Schneider, M. Gabay, S. Thiel, G. Hammerl, J. Mannhart, and J.-M. Triscone, Nature (London) **456**, 624 (2008).

[26] G. Koster, B. L. Kropman, G. J. H. M. Rijnders, D. H. A. Blank, and H. Rogalla, Appl. Phys. Lett. **73**, 2920 (1998).

[27] J. Carrasco, F. Illas, N. Lopez, E. A. Kotomin, Yu. F. Zhukovskii, R. A. Evarestov, Yu. A. Mastrikov, S. Piskunov, and J. Maier, Phys. Rev. B **73**, 064106 (2006).

[28] A. Kalabukhov, R. Gunnarsson, J. Brjesson, E. Olsson, T. Claeson and D. Winkler, Phys. Rev. B **75**, 121404 (2007).

[29] A. F. Santander-Syro, O. Copie, T. Kondo, F. Fortuna, S. Pailhès, R. Weht, X. G. Qiu, F. Bertran, A. Nicolaou, A. Taleb-Ibrahimi, P. Le Fèvre, G. Herranz, M. Bibes, N. Reyren, Y. Apertet, P. Lecoeur, A. Barthélémy, and M. J. Rozenberg, Nature (London) **469**, 189 (2011).

[30] T. Hernandez, C. W. Bark, D. A. Felker, C. B. Eom, and M. S. Rzchowski1, Phys. Rev. B **85**, 161407 (2012).

[31] J. S. Kim, S. S. A. Seo, M. F. Chisholm, R. K. Kremer, H. U. Habermeier, B. Keimer, and H. N. Lee, Phys. Rev. B **82**, 201407 (2010).

[32] R. Ohtsuka, M. Matvejeff, K. Nishio, R. Takahashi, and M. Lippmaa, Appl. Phys. Lett. **96**, 192111 (2010).

[33] N. W. Ashcroft and N. D. Mermin, *Solid State Physics* (Harcourt Brace College Publishers, 1976) p 240.

[34] H. P. R. Frederikse, W. R. Thurber, and W. R. Hosler, Phys. Rev. **134**, A442 (1964).

[35] O. N. Tufte and P. W. Chapman, Phys. Rev. **155**, 796 (1967).

[36] Y. Kozuka, Y. Hikita, T. Susaki, and H. Y. Hwang, Phys. Rev. B **76**, 085129 (2007).

[37] M. Lee, J. R. Williams, S. Zhang, C. D. Frisbie, and D. Goldhaber-Gordon, Phys. Rev. Lett. **107**, 256601 (2011).

Chapter 4

Thermally excited multi-band conduction in $LaAlO_3/SrTiO_3$ heterostructures exhibiting magnetic scattering

Abstract

Magnetotransport measurements of charge carriers at the interface of a $LaAlO_3/SrTiO_3$ heterostructure with 26 unit cells of $LaAlO_3$ show Hall resistance and magnetoresistance which at low and high temperatures is described by a single channel of electron-like charge carriers. At intermediate temperatures, we observe non-linear Hall resistance and positive magnetoresistance, which show the presence of at least two electron-like channels with significantly different mobilities and carrier concentrations. These channels are separated by 6 meV in energy and their temperature dependent occupation and mobilities are responsible for the observed transport properties of the interface. We observe that one of the channels has a mobility that decreases with decreasing temperature, consistent with magnetic scattering in this channel.

This chapter is based on work published in: V. K. Guduru et al., Physical Review B: Rapid Communications **88**, 241301(R) (2013) and V. K. Guduru et al., Journal of the Korean Physical society **63**, 437 (2013).

4.1 Introduction

One of the many intriguing features[1–4] of the conducting interface between two band-insulating perovskite oxides $SrTiO_3$ (STO) and $LaAlO_3$ (LAO)[5] is that its magnetotransport properties closely resemble those of the conventional semiconductor heterostructures. Namely, the charge carriers in LAO/STO heterostructures display classical magnetotransport features such as positive magnetoresistance (MR), negative MR, and non-linear Hall resistance at low and intermediate temperatures[3,6–11] and also show quantum mechanical behaviour such as Shubnikov-de Haas effect at low temperatures.[12–14] Despite this familiar transport behaviour of this new LAO/STO oxide heterostructures, the exact origin and nature (electrons or holes) of the charge carriers at the interface is still not yet clear. The major difficulty in achieving consensus about the intrinsic electronic nature of the interfaces is due to the fact that their transport properties strongly depend on external factors such as the growth conditions of the LAO layer,[3] LAO layer thickness,[15,16] and the layers structure of the heterostructures.[14,17–19] In order to realize the full potential of LAO/STO heterostructures in technological applications,[20–22] the fundamental physical nature of the interface conductivity has to be understood thoroughly.

This chapter describes a study of the interface electronic structure of one specific type of LAO/STO heterostructure, which exhibits magnetic signatures.[3] We have performed transport experiments with the magnetic field oriented perpendicular and parallel to the interface, and measured the Hall resistance and sheet resistance in a wide temperature range and at high magnetic fields compared to previous magnetotransport reports.[3,6–11] We observed a strong, temperature-dependent, non-linear Hall resistance accompanied by a large positive magnetoresistance (MR)[23] at intermediate temperatures, and a negative MR at low-temperatures. We quantitatively analyse our data using a simple two-carrier model, considering two electron-like conduction channels with different densities and mobilities. Our interpretation is in line with the results described in chapter 3, which show that two-channel (electron-like) conduction can be realized in similar LAO/STO heterostructures by means of UV-illumination on the surface of the sample at low-temperature.[24] Furthermore, we show that the negative MR[3] at low temperatures is not a result of two-band conduction alone. Rather, we observe that one of the channels has a mobility that decreases with decreasing temperature, consistent with the previously suggested[3] magnetic scattering scenario in this channel. More detailed analysis of the negative MR and its magnetic nature is discussed in chapter 6.

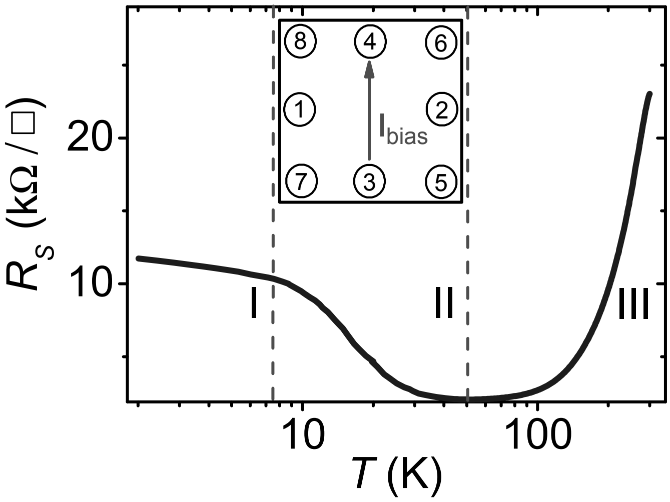

Figure 4.1: *The sheet resistance R_s of the sample as a function of temperature (on a logarithmic scale) between 2 K and 300 K, divided into three regimes by dashed lines. The units Ω / □ (square) represents the R_s of square sample regardless of its dimensions. The inset shows the schematic top-view of the sample, with the contact configuration indicated as circles and the bias current I_{bias} with an arrow.*

4.2 Sample preparation and experimental details

The sample used for our measurements was grown by pulsed laser deposition using a single-crystalline $LaAlO_3$ target. The 10 nm (26 unit cells) LAO film was deposited on a 5 mm × 5 mm TiO_2-terminated single crystal STO [001] substrate,[25] at a substrate temperature of 850°C and an oxygen pressure of 2×10^{-3} mbar. The growth of the LAO film was monitored using in-situ reflection high-energy electron diffraction, indicating that layer-by-layer growth of individual LAO unit cells (uc) is preserved up to 26 uc (Fig. 2.4(c)). After the growth, the sample was cooled to room temperature with the oxygen pressure remaining at 2×10^{-3} mbar.

The sample was mounted on a ceramic chip carrier and electrical contacts were made by ultrasonically bonding aluminium wires. The sample resistance was measured with the contacts as schematically depicted in the inset of Fig. 4.1:

we denote the resistance as $R_{ij,kl}$, where current is passed through the contacts i and j, and the voltage drop is measured between k and l. For a homogeneous sample, the sheet resistance R_s is calculated from $R_{34,56}$ using the relation $R_s = 1.5 \times R_{34,56}$. Here we have determined the numeric ratio between R_s and $R_{34,56}$ by van der Pauw measurements on different contact configurations where we find similar values for R_s.

The magnetotransport measurements were performed in a temperature controlled ^{4}He flow cryostat and in a pumped ^{3}He system at magnetic fields up to 30 T. The sheet resistance and Hall resistance ($R_{xy} = R_{34,12}$) were measured for both positive and negative magnetic field directions, using a standard, low-frequency lock-in technique with an excitation current of 1 μA. In order to exclude admixtures of R_s in R_{xy} or vice versa we always show the antisymmetrised Hall resistance data and symmetrized sheet resistance data in the remainder of this chapter. The results we present here have been reproduced on several similar samples.

4.3 Experimental results and discussion

The measured sheet resistance R_s is shown as a function of temperature between 2 K and 300 K in Fig. 4.1. Three distinct regimes can be observed in $R_s(T)$: In region (I), from 2 K to 7.5 K, the sheet resistance decreases logarithmically as temperature increases up to 7.5 K, which is attributed to the Kondo effect originating from the scattering of mobile carriers off localized magnetic moments;[3, 27] in region (II), from 7.5 K to 50 K, further increase of temperature leads to a sharp decrease of resistance with a minimum value around 50 K; in region (III), above 50 K, the sample resistance increases monotonically with temperature, which can be attributed to electron-phonon scattering.

Figs. 4.2(a) and 2(b) show the Hall resistance and sheet resistance data, respectively, for the applied magnetic field orientated perpendicular to the LAO/STO interface, for temperatures between 0.3 K (region I) and 65 K (region III): the data points are shown as open symbols. At low-temperatures, below 7.5 K, the Hall resistance is linear and independent of temperature, and the sheet resistance decreases as a function of magnetic field, resulting in a strong negative MR. At intermediate temperatures, from 7.5 K to 50 K, the Hall resistance is strikingly non-linear and the sheet resistance increases strongly as a function of magnetic field, resulting in a large positive MR. At high-temperatures, above 50 K, the Hall resistance is linear and the sheet resistance increases slightly as a function of magnetic field, resulting in a negligible positive MR. We also observed a similar non-linear Hall resistance accompanied by a large positive

MR, in several other LAO/STO samples with different thickness (results are shown in appendix A) of LAO film at low-temperature (4.2 K).

Observations of a temperature dependent MR (positive and/or negative) and (non-linear/anomalous) Hall resistance have been well documented in many different materials. For example, in doped conventional semiconductors such as n-type Ge, GaAs, InSb and Mn doped GaAs,[28–32] in noble metals doped with transition elements, such as Au doped with Co,[33] and in (magnetic) semiconductor heterostructures (AlGaAs/GaAs, InMnAs/GaAlSb),[34–36] as well as in perovskite oxide heterostructures ($LaTiO_3/SrTiO_3$, $LaVO_3/SrTiO_3$).[37–39] A temperature dependent crossover from negative to positive MR has also been observed in doped semiconductors (In doped CdS)[40] and in magnetic semiconductor heterostructures (InMnAs/GaAlSb).[32,36] The general consensus is that positive MR and non-linear Hall resistance arise due to the contribution to transport of two parallel channels of charge carriers with different mobility. The change in resistance is attributed to the change of electron distribution and mobility in these two channels, caused by the temperature or magnetic field. Negative MR is largely attributed to scattering of conduction charge carriers with localized magnetic moments: the external magnetic field reduces this scattering and results in a decrease of resistance.[40]

Fig. 4.2(c) shows the sheet resistance data when the applied magnetic field orientation is parallel to the LAO/STO interface, for temperatures between 0.3 K (region I) and 40 K (region II). At low-temperatures, the sheet resistance decreases as a function of magnetic field, resulting in a strong negative MR. The MR below 4.2 K is independent of the field orientation, at odds with an interpretation in terms of weak localization, and consistent with electron spin scattering off localized magnetic moments.[3] The decrease in magnitude of the negative MR with increased temperature can be attributed to the depolarization of magnetic moments by thermal excitation at higher temperatures.[8,41] At intermediate temperatures, the sheet resistance is almost field independent. At low temperatures MR is negative and independent of magnetic field orientation. The relation between this behaviour and the magnetic nature of the interface carriers is discussed in chapter 6.

In order to understand our experimental data, we use the concepts of magnetotransport in the classical regime as described in chapter 2 (section 2.3.2). The linear Hall resistance below 7.5 K (region I) and above 50 K (region III) can be described using the conventional single-carrier model. The carrier concentration ($n_s = B/R_{xy}e$) and mobility ($\mu = 1/R_s(0)en_s$) are extracted from the slope of the linear Hall resistance data and zero field sheet resistance $R_s(0)$ with e as the electronic charge. The values obtained for n_s and μ by the single-carrier model are shown in Figs. 4.3(a) and 3(b).

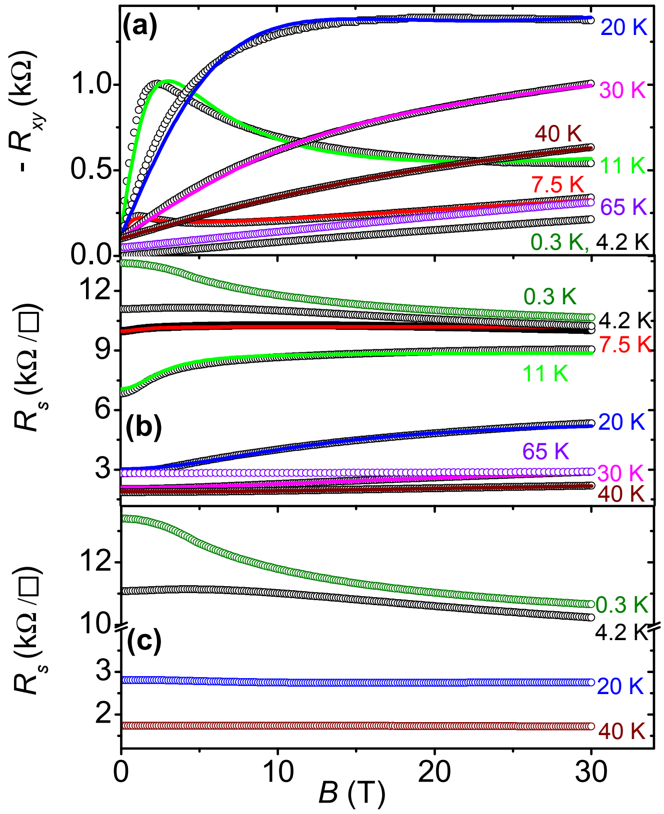

Figure 4.2: *(a) Hall resistance R_{xy} and (b) sheet resistance R_s with the magnetic field-oriented perpendicular to the LAO/STO interface for temperatures between 0.3 K and 65 K, shown as open circles. Solid lines in (a) and (b) are the results obtained after simultaneously fitting the R_{xy} and R_s data using a simple two-carrier model. The R_{xy} curves are offset vertically for clarity. (c) Sheet resistance R_s for the applied magnetic field-oriented parallel to the LAO/STO interface for temperatures between 0.3 K and 40 K, shown as open circles. The y-axis is cut between 4 and 10 kΩ.*

In contrast, the non-linear Hall resistance and the positive MR between 7.5 K and 50 K (region II) cannot be explained within a single-carrier model, but rather suggest a multi-channel system. A similar non-linear Hall resistance and positive MR were observed previously in LaTiO$_3$/SrTiO$_3$,[39] and explained in terms of two-channel conduction from electronic bands with different mobilities, $\mu_{1,2}$ and carrier densities, $n_{1,2}$. We use similar two-electron-band expressions,[42]

$$R_{xy}(B) = \frac{B}{e}\frac{(n_1\mu_1^2 + n_2\mu_2^2) + (\mu_1\mu_2 B)^2(n_1+n_2)}{(n_1\mu_1 + n_2\mu_2)^2 + (\mu_1\mu_2 B)^2(n_1+n_2)^2}, \tag{4.1}$$

$$R_s(B) = R_s(0)\left[1 + \frac{(n_1\mu_1 n_2\mu_2(\mu_1-\mu_2)^2 B^2)}{(n_1\mu_1 + n_2\mu_2)^2 + ((n_1+n_2)\mu_1\mu_2 B)^2}\right], \tag{4.2}$$

to model our non-linear Hall resistance $R_{xy}(B)$ and sheet resistance $R_s(B)$ data as a function of magnetic field.

In this expression (4.1 and 4.2), we take n_1, μ_1 to be the carrier density and mobility of the existing electron band at low-temperatures and n_2, μ_2 are the carrier density and mobility of the thermally activated second electron band. For low magnetic fields, where $\mu_1 B$, $\mu_2 B \ll 1$, $R_{xy}(B)$ shows B-linear behaviour, and $R_s(B)$ shows quadratic dependency on B. For high magnetic fields, where $\mu_1 B$, $\mu_2 B \gg 1$, $R_{xy}(B)$ shows B-linear behaviour, and $R_s(B)$ saturates. In an intermediate regime, where either $\mu_1 B \simeq 1$ or $\mu_2 B \simeq 1$, $R_{xy}(B)$ becomes non-linear.

Fits of the Hall resistance and sheet resistance to this two-band model are shown in Figs. 4.2(a) and 2(b) as solid lines. The non-linear Hall resistance $R_{xy}(B)$ and sheet resistance $R_s(B)$ at each temperature were fitted simultaneously, using n_1, n_2 and μ_1, μ_2 as fit parameters. The fits are in good agreement with the experimental data and the model is able to nicely reproduce the details of the magnetotransport ($R_{xy}(B)$ and $R_s(B)$) in the temperature region between 7.5 K to 50 K, where the data cannot be described within a single carrier model.

The results of our analysis of the magnetotransport data in the three temperature regions are shown in Fig. 4.3. The obtained values for the fit parameters n_1, n_2 are shown in Fig. 4.3(a) and μ_1, μ_2 are shown in Fig. 4.3(b).

For temperatures below 7.5 K (region I), transport is dominated by a low mobility electron band with a constant, high, sheet density of $n_1 = 8.7 \times 10^{13}$ cm^{-2}. The mobility of electrons in this band increases from $\mu_1 = 3$ cm^2/Vs to 5 cm^2/Vs with an increase in temperature from 0.3 K to 4.2 K. We observe that the negative magnetoresistance is not due to the two-band effects, but is due to the properties of the low mobility band. The temperature dependence of the mobility of this band at low-temperatures is consistent with electron scattering off localized magnetic moments. In detail, at low-temperatures, in zero magnetic field, the increased scattering of the conduction carriers with the localized magnetic moments results in the further decrease of carrier mobility (as

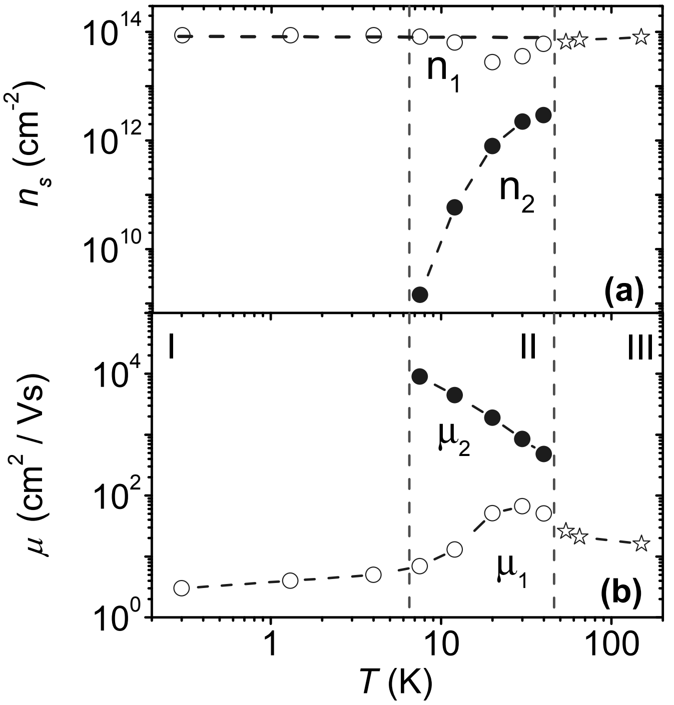

Figure 4.3: *The temperature-dependence of sheet carrier density n_s and mobility μ obtained from the analysis of experimental data in Figs. 4.2(a) and (b). (a) The sheet carrier density n_s for region I & II are shown as open circles (n_1), filled circles (n_2) and for region III are shown as stars. (b) The carrier mobility μ for region I & II is shown as open circles (μ_1), filled circles (μ_2) and for region III is shown as stars. The connecting dashed lines between the data points are guides to the eye.*

shown in region I of Fig. 4.3(b)). The temperature dependence of the mobility indirectly related to the negative magnetoresistance. For the case of applied magnetic field, the localized magnetic moments are aligned with field resulting in reduced scattering of the conduction carriers at Fermi-level. This results in increased mobility and conductivity of the conduction carriers and causes a negative magnetoresistance, shown in the Figs. 4.2(b) and (c).

For temperatures between 7.5 K and 50 K (region II), electrons are thermally activated into a second electron band (n_2, μ_2) in addition to the existing low mobility electron band (n_1, μ_1). The carrier density n_1 in the low mobility electron band stays almost temperature independent while the mobility μ_1 increases by about an order of magnitude from 7 cm^2/Vs to 50 cm^2/Vs. The carrier density n_2 in the second electron band shows a strong temperature dependence and increases by a few orders of magnitude from 1.4×10^9 cm^{-2} to 2.9×10^{12} cm^{-2}, the mobility μ_2 decreases by an order of magnitude from 8980 cm^2/Vs to 440 cm^2/Vs. The decrease in mobility of μ_2 as the temperature increases is likely to be the result of increased electron-phonon scattering. At low temperature μ_1 is dominated by magnetic scattering, which is expected to decrease with increasing temperature leading to the observed increase in μ_1. As the temperature is further increased, electron-phonon scattering also begins to strongly affect the lower energy conduction channel, so that μ_1 reaches a maximum (at $\sim$ 30 K) and then decreases at higher temperatures.

This thermal activation of electrons into a second, energetically higher, channel is visualized in Fig. 4.4(a). The activation energy of carriers ε is related to the concentration in the second electron channel by the Arrhenius relation, $n_2 \propto e^{(-\varepsilon/k_B T)}$, where k_B is the Boltzmann constant and T is temperature. The linear slope of $\ln(n_2)$ versus $1/T$ gives $\varepsilon = 6$ meV. For temperatures above 50 K (region III), the mobilities of the two electron channels become comparable and the two channels no longer give distinguishable contributions to the transport (see expressions 4.1 and 4.2). The *total* carrier concentration and mobility can then be obtained from a single band calculation. The total carrier concentration remains temperature independent at the value $n_s = 8.7 \times 10^{13}$ cm^{-2} and the average mobility further decreases to $\mu = 16$ cm^2/Vs at 150 K.

We explain our results by tentatively considering two simplified interface electronic states (D_1 and D_2) as schematically depicted in Fig. 4.4(b). The oxygen vacancies in STO (each oxygen vacancy donates two free electrons) and/or the electronic reconstruction (half an electron transfer from LAO to STO) give a reservoir of charge carriers at the interface, which includes both localized and mobile carriers. At finite (low) temperature (region I), the charge carriers are present in a lower energy level (D_1) which has a low mobility (μ_1) and high electron density (n_1). These carriers are responsible for the observed Kondo type behaviour (i.e., logarithmic increase of sheet resistance accompanied by the decrease of carrier mobility for decreasing temperature down to 0.3 K), negative MR and linear Hall resistance. The observed negative MR resides at the low mobility channel and is consistent with magnetic scattering. On increasing the temperature through region II, broadening of the Fermi function results in the thermal excitation of charge carriers into a higher energy level (D_2) separated from the lower level by 6 meV, which has a high mobility (μ_2) and low electron density (n_2). Both the low and high mobility bands contribute to the transport in region II and are responsible for the observed large, positive MR and non-linear Hall resistance. In this case, as given by Eq. 4.2 of $R_s(B)$, the term accounts for difference in the mobilities of the two electronic channels gives predominantly higher contribution to the MR, which eventually resulting very strong positive MR. When the temperature is further increased above 50 K (region III), the mobilities of these two conduction channels become similar. As a result we can not distinguish the two band conduction any longer, which eventually gives rise to a linear Hall resistance and a negligible positive MR.

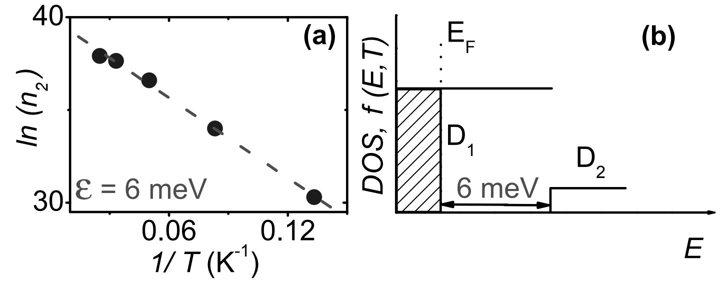

Figure 4.4: *(a) The Arrhenius plot of the thermally excited carrier density n_2. The slope of the dashed line gives ε = 6 meV. (b) Schematic representation of the 2D level structure with constant density of states for the two parallel electron-like conduction channels at the interface. At T = 0 K, the level D_1 is occupied up to the Fermi energy E_F (dotted line); at T = 60 K, broadening (6 meV) of the Fermi function results in the occupation of level D_2.*

Our results and analysis strongly suggest that at least two channels of electron-like carriers at the interface are responsible for the observed transport behaviour in these LAO/STO heterostructures exhibiting magnetic scattering, but they do not allow us to determine the exact physical origin of these interface conduction channels. However, from similarities between our results and available information in the literature, we can propose a few possibilities for the origin of the observed electron bands.

It has been predicted theoretically[43,44] and shown experimentally[45] that the magnetism in LAO/STO originates from the t_{2g} band of Ti-3d orbitals, specifically from the energy level formed from d_{xy} orbitals with Ti^{3+} character. This suggests that in our sample the observed energy level (D_1) associated with the low mobility carriers (n_1, μ_1) and responsible for magnetic effects (Kondo effect, negative MR), could originate from these d_{xy} orbitals. The observed energy level (D_2) associated with the high mobility carriers (n_2, μ_2) is separated by 6 meV from the low mobility level in our sample; this activation energy is strikingly similar to values found in earlier observations of carrier activation in $SrTiO_3/LaAlO_3/SrTiO_3$ heterostructures,[17, 18] and comparable to La doped $SrTiO_3$.[46] There is evidence from previous work that the higher energy conduction channel we observe is likely to have primarily $d_{xz/yz}$ character.[47–49] This seems to be a reasonable assumption for our sample, based on the energy separation of the conduction channels and the carrier density involved.[49, 50]

We have also performed similar measurements on LAO/STO samples with thinner LAO layers (20, 15, 10, 5 uc of LAO) where we observe 2-channel conduction of a high mobility and a low mobility channel, which in contrast to the 26 LAO system, is present down to the lowest temperatures. We interpret this observation by a different energetic alignment of the two channels. This coexistence at low temperature precludes a clear distinction of their individual contribution to magnetotransport as compared to the 26 LAO system where the two channels are well separated.

A primary aim of this work was to understand the interface conductivity in 26 LAO/STO, which shows magnetic effects at a particular configuration. It is also important to understand/investigate the sensitivity of the interface conductivity to the sample structure/configuration. Why does only samples with 26 LAO/STO layers show these magnetic effects. We have measured several of these and they all show the same behaviour.

We now concentrate on samples with lesser number of monolayers. We have measured several other LAO/STO heterostructures with different layers structure. As part of it, we performed temperature-dependent magnetotransport measurements on heterostructures with different layers structure (depicted in Fig.1 of appendix A), such as 10 LAO/STO (10 unit cells of $LaAlO_3$ film grown on $SrTiO_3$ substrate), 2 STO/10 LAO/STO (10 unit cells of $LaAlO_3$ film grown on $SrTiO_3$ substrate, capped by two monolayers of $SrTiO_3$), and 2 STO/1 SCO/10 LAO/STO (10 monolayers of $LaAlO_3$ grown on a $SrTiO_3$ substrate, capped by one monolayer of $SrCuO_3$ (SCO) and two monolayers of $SrTiO_3$). We have observed similar non-linear Hall resistance and positive MR, in the temperature range between 20 K and 65 K, but no negative MR at low temperatures for these three other samples with different layers structure. We are able to describe the positive MR and non-linear R_{xy} using the simple two-carrier model (as described in earlier in this chapter) at intermediate temperatures (above 20 K), and the results are shown in appendix A. This means that also in these samples there exist (at least) two separate electronic channels with significantly different mobilities and densities at the LAO/STO interface, irrespective of the layers structure of the heterostructure, like in the 26 monolayer sample showing magnetic scattering.

In the samples with layers structure as STO/SCO/LAO/STO, i.e. the only one having an SCO layer in the middle, the low-temperature transport is dominated by the high mobility channel resulting in quantum oscillations in resistivity, which we will discuss in chapter 5.

4.4 Summary

In summary, our experimental results show that the low-temperature regime ($T \leq 4.2$ K) is dominated by single charge carrier type with a low carrier mobility, yielding a linear Hall resistance and negative MR. Increasing temperature above 4.2 K leads to a significant decrease of the resistance, a strong positive MR appears and the Hall resistance becomes distinctly non-linear. Our observations are quantitatively explained by thermal excitation of an additional high mobility electron channel situated 6 meV above the low mobility channel. Our results can be understood by considering the interface electronic structure consists of at least two electron-like channels responsible for the observed magnetotransport behaviour. We suggest that the two electron channels are possibly originated from the t_{2g} band of Ti-3d orbitals.

In conclusion we have found that all samples, irrespective of their layer thickness show the same two-channel (one high mobility and one low mobility) conduction at intermediate temperatures. The thick sample (26 monolayers of LAO) show magnetic scattering at low temperatures in the low mobility channel, whereas the thin ones (1 monolayer of SCO and 2 monolayers of STO) show quantum oscillations at low temperatures associated with the high mobility channel.

References

[1] S. Thiel, G. Hammerl, A. Schmehl, C. W. Schneider, and J. Mannhart, Science **313**, 1942 (2006).

[2] N. Reyren, S. Thiel, A. D. Caviglia, L. F. Kourkoutis, G. Hammerl, C. Richter, C. W. Schneider, T. Kopp, A. S. Ruetschi, D. Jaccard, M. Gabay, D. A. Muller, J.-M. Triscone, and J. Mannhart, Science **317**, 1196 (2007).

[3] A. Brinkman, M. Van Zalk, J. Huijben, U. Zeitler, J. C. Maan, W. G. Van der Wiel, G. Rijnders, D. H. A. Blank, and H. Hilgenkamp, Nature Mater. **6**, 493 (2007).

[4] A. D. Caviglia, S. Gariglio, N. Reyren, D. Jaccard, T. Schneider, M. Gabay, S. Thiel, G. Hammerl, J. Mannhart, and J.-M. Triscone, Nature (London) **456**, 624 (2008).

[5] A. Ohtomo and H.Y. Hwang, Nature **427**, 423 (2004).

[6] M. Ben Shalom, C. W. Tai, Y. Lereah, M. Sachs, E. Levy, D. Rakhmilevitch, A. Palevski, and Y. Dagan, Phys. Rev. B **80**, 140403 (2009).

[7] Ariando, X. Wang, G. Baskaran, Z. Q. Liu, J. Huijben, J. B. Yi, A. Annadi, A. R. Barman, A. Rusydi, S. Dhar, Y. P. Feng, J. Ding, H. Hilgenkamp, and T. Venkatesan, Nature Commun. **2**, 188 (2011).

[8] X. Wang, W. M. Lü, A. Annadi, Z. Q. Liu, K. Gopinadhan, S. Dhar, T. Venkatesan, and Ariando, Phys. Rev. B **84**, 075312 (2011).

[9] C. Bell, S. Harashima, Y. Kozuka, M. Kim, B. G. Kim, Y. Hikita, and H. Y. Hwang, Phys. Rev. Lett. **103**, 226802 (2009).

[10] R. Pentcheva, M. Huijben, K. Otte, W. E. Pickett, J. E. Kleibeuker, J. Huijben, H. Boschker, D. Kockmann, W. Siemons, G. Koster, H. J. W. Zandvliet, G. Rijnders, D. H. A. Blank, H. Hilgenkamp, and A. Brinkman, Phys. Rev. Lett. **104**, 166804 (2010).

[11] T. Hernandez, C. W. Bark, D. A. Felker, C. B. Eom, and M. S. Rzchowski, Phys. Rev. B **85**, 161407 (2012).

[12] M. Ben Shalom, A. Ron, A. Palevski, and Y. Dagan, Phys. Rev. Lett. **105**, 206401 (2010).

[13] A. D. Caviglia, S. Gariglio, C. Cancellieri, B. Sacepe, A. Fete, N. Reyren, M. Gabay, A. F. Morpurgo, and J.-M. Triscone, Phys. Rev. Lett. **105**, 236802 (2010).

[14] A. McCollam, S. Wenderich, M. K. Kruize, V. K. Guduru, H. J. A. Molegraaf, M. Huijben, G. Koster, D. H. A. Blank, G. Rijnders, A. Brinkman, H. Hilgenkamp, U. Zeitler, and J. C. Maan, Appl. Phys. Lett.: Materials **2**, 022102 (2014).

[15] C. Bell, S. Harashima, Y. Hikita, and H. Y. Hwang, Appl. Phys. Lett. **94**, 222111 (2009).

[16] F. J. Wong, R. V. Chopdekar, and Y. Suzuki, Phys. Rev. B **82**, 165413 (2010).

[17] M. Huijben, G. Koster, M. K. Kruize, S. Wenderich, J. Verbeeck, S. Bals, E. Slooten, B. Shi, H. J. A. Molegraaf, J. E. Kleibeuker, S. van Aert, J. B. Goedkoop, A. Brinkman, D. H. A. Blank, M. S. Golden, G. van Tendeloo, H. Hilgenkamp, and G. Rijnders, Adv. Funct. Mater. **23**, 5240 (2013).

[18] M. Huijben, G. Rijnders, D. H. A Blank, S. Bals, S. van Aert, J. Verbeeck, G. van Tendeloo, A. Brinkman, and H. Hilgenkamp, Nature Mater. **5**, 556 (2006).

[19] M. Huijben, A. Brinkman, G. Koster, G. Rijnders, H. Hilgenkamp, and D. H. A Blank, Adv. Mater. **21**, 1665 (2009).

[20] J. Mannhart and D. G. Schlom, Science **327**, 1607 (2010).

[21] H. Y. Hwang, Y. Iwasa, M. Kawasaki, B. Keimer, N. Nagaosa, and Y. Tokura, Nature Mater. **11**, 103 (2012).

[22] E. Assmann, P. Blaha, R. Laskowski, K. Held, S. Okamoto, and G. Sangiovanni, Phys. Rev. Lett. **110**, 078701 (2013).

[23] V. K. Guduru, A. McCollam, S. Wenderich, M. K. Kruize, A. Brinkman, M. Huijben, G. Koster, D. H. A. Blank, G. Rijnders, H. Hilgenkamp, J. C. Maan, and U. Zeitler, J. Kor. Phys. Soci. **63**, 437 (2013).

[24] V. K. Guduru, A. Granados del Aguila, S. Wenderich, M. K. Kruize, A. McCollam, P. C. M. Christianen, U. Zeitler, A. Brinkman, G. Rijnders, H. Hilgenkamp, and J. C. Maan, Appl. Phys. Lett. **102**, 051604 (2013).

[25] G. Koster, B. L. Kropman, G. J. H. M. Rijnders, D. H. A. Blank, and H. Rogalla, Appl. Phys. Lett. **73**, 2920 (1998).

[26] G. J. H. M. Rijnders, G. Koster, D. H. A. Blank, and H. Rogalla, Appl. Phys. Lett. **70**, 1888 (1997).

[27] J. Kondo, Prog. Theor. Phys. **32**, 37 (1964).

[28] W. Sasaki and R. De Bruyn Ouboter, Physica **27**, 877 (1961).

[29] J. F. Woods and C. Y. Chen, Phys. Rev. **135**, A1462 (1964).

[30] Y. Katayama and S. Tanaka, Phys. Rev. **153**, 873 (1967).

[31] L. Halbo and R. J. Sladek, Phys. Rev. **173**, 794 (1968).

[32] F. Matsukura, H. Ohno, A. Shen, and Y. Sugawara, Phys. Rev. B **57**, R2037 (1998).

[33] A. N. Gerritsen, Physica **25**, 489 (1959).

[34] H. van Houten, J. G. Williamson, M. E. I. Broekaart, C. T. Foxon, and J. J. Harris, Phys. Rev. B **37**, 2756 (1988).

[35] S. J. Battersby, F. M. Selten, J. J. Harris, and C. T. Foxon, Solid-State Electronics **31**, 1083 (1998).

[36] A. Oiwa, A. Endo, S. Katsumoto, Y. Iye, H. Ohno, and H. Munekata, Phys. Rev. B **59**, 5826 (1999).

[37] Y. Hotta, T. Susaki, and H. Y. Hwang, Phys. Rev. Lett. **99**, 236805 (2007).

[38] R. Scherwitzl, S. Gariglio, M. Gabay, P. Zubko, M. Gibert, and J.-M. Triscone, Phys. Rev. Lett. **106**, 246403 (2011).

[39] J. S. Kim, S. S. A. Seo, M. F. Chisholm, R. K. Kremer, H. U. Habermeier, B. Keimer, and H. N. Lee, Phys. Rev. B **82**, 201407 (2010).

[40] R. P. Khosla and J. R. Fischer, Phys. Rev. B **2**, 4084 (1970).

[41] M. Lee, J. R. Williams, S. Zhang, C. D. Frisbie, and D. Goldhaber-Gordon, Phys. Rev. Lett. **107**, 256601 (2011).

[42] N. W. Ashcroft and N. D. Mermin, *Solid State Physics* (Harcourt Brace College Publishers, 1976) p 240.

[43] R. Pentcheva and W. E. Pickett, Phys. Rev. B **74**, 035112 (2006).

[44] R. Pentcheva and W. E. Pickett, Phys. Rev. Lett. **99**, 016802 (2007).

[45] J.-S. Lee, Y. W. Xie, H. K. Sato, C. Bell, Y. Hikita, H. Y. Hwang, and C.-C. Kao, Nature Mater. **12**, 703 (2013).

[46] T. Okuda, K. Nakanishi, S. Miyasaka, and Y. Tokura, Phys. Rev. B **63**, 113104 (2001).

[47] M. Salluzzo, J. C. Cezar, N. B. Brookes, V. Bisogni, G. M. De Luca, C. Richter, S. Thiel, J. Mannhart, M. Huijben, A. Brinkman, G. Rijnders, and G. Ghiringhelli, Phys. Rev. Lett. **102**, 166804 (2009).

[48] G. Berner, M. Sing, H. Fujiwara, A. Yasui, Y. Saitoh, A. Yamasaki, Y. Nishitani, A. Sekiyama, N. Pavlenko, T. Kopp, C. Richter, J. Mannhart, S. Suga, and R. Claessen, Phys. Rev. Lett. **110**, 247601 (2013).

[49] G. Khalsa and A. H. MacDonald, Phys. Rev. B **86**, 125121 (2012).

[50] L. W. van Heeringen, G. A. de Wijs, A. McCollam, J. C. Maan, and A. Fasolino, Phys. Rev. B **88**, 205140 (2013).

Chapter 5

Two-dimensional quantum oscillations of the electron gas at the $LaAlO_3/SrTiO_3$ interface

Abstract

Low-temperature mobility of a 2D electron gas of the order of few thousands cm^2/Vs can be realized at the interface of $LaAlO_3/SrTiO_3$ heterostructures by capping it with one monolayer of $SrCuO_2$ and two monolayers of $SrTiO_3$. The magnetotransport performed on such high-mobility interfaces shows Shubnikov-de Haas (SdH) oscillations at high magnetic fields and low-temperatures. Fourier transform analysis of the SdH results reveals four or five frequencies corresponding to multiple 2D conduction subbands present at the interface. The spacing of subbands is in the order of few meV with the lowest energy subband lying at less-than 6 meV below the Fermi energy. Measurements as a function of magnetic field orientation confirm the two-dimensional character of the Fermi surface, and also show a negative magnetoresistance step, indicative of the depopulation of higher energy subbands in a parallel magnetic field.

This chapter is based on work published in: A. McCollam, S. Wenderich, M. K. Kruize, V. K. Guduru et al., Applied Physics Letters: Materials 2, 022102 (2014).

5.1 Introduction

The conducting interface[1] realized in $LaAlO_3/SrTiO_3$ heterostructures hosts a wide variety of physical phenomena, such as superconductivity[2] and magnetism (chapter 6 of this thesis),[2–8] not present in other semiconductor heterostructures such as GaAs/AlGaAs. The 2D nature of the conducting interface is evidenced by the substrate termination dependence of the conductivity,[1] the abrupt onset of the conductivity above a critical thickness of the $LaAlO_3$ layer,[1,9] the nature of the superconducting phase transition,[2] and the 2D character of the observed SdH oscillations.[1,10–12] Three main mechanisms, i.e. electronic reconstruction, oxygen vacancies and cationic intermixing are suggested to be responsible for the interface conductivity (more description of these mechanisms is given in chapter 1). However, the exact physical origin and nature of the 2D conduction electrons and the details of the electronic band structure at the interface are not yet understood.

In order to address these issues, we have performed magnetotransport on $LaAlO_3/SrTiO_3$ heterostructures capped with one monolayer of $SrCuO_2$ and two monolayers of $SrTiO_3$, as a function of temperature and in a range of magnetic field orientations, from perpendicular to parallel to the interface plane. We have measured the SdH oscillations in resistivity of the high-mobility 2D electron systems, at low-temperatures and in higher magnetic fields as compared to previous reports.[1,10,11] These measurements enabled us to identify and obtain the characteristic features of several 2D conduction subbands. The subbands are very closely spaced by a few meV, and have different effective masses, carrier densities and mobilities. These characteristics of the 2DEG that we observed at the $LaAlO_3/SrTiO_3$ interface are different to previous reports on the oxide heterostructures (ZnO/ZnMgO and $LaAlO_3/SrTiO_3$), where only a single subband of carriers contributing to the transport could be clearly resolved.[10,11,13]

This chapter describes the growth conditions of the high-mobility $LaAlO_3/SrTiO_3$ samples used for the magnetotransport, experimental details and results, analysis of the results together with discussion and concluding remarks. The analysis of the SdH results presented here are performed by A. McCollam. In order to explain the experimental data and to shed some light on the fundamental understanding of electronic transport of this new oxide conducting interface, we have used the concepts of magnetotransport in the quantum regime of 2D electron systems, as described in chapter 2 (section 2.3.3).

5.2 Samples and experimental details

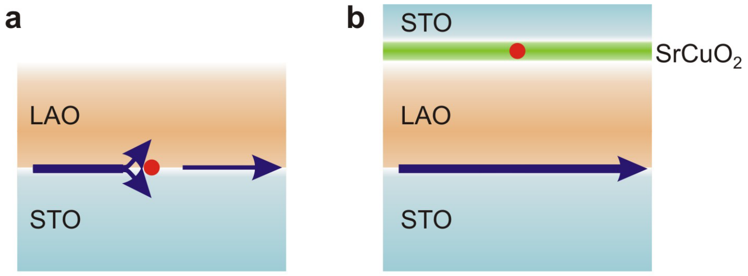

Figure 5.1: *(a) Schematic drawing of impurity scattering of conduction carriers at $LaAlO_3/SrTiO_3$ interface, and (b) schematic of $SrTiO_3/SrCuO_2/LaAlO_3/SrTiO_3$ heterostructure where the effective scattering of carriers is suppressed by the introduction of a SrCuO2 layer, which is believed to act as a preferred site for oxygen vacancies. Carrier transport is indicated by (blue) arrows, while the oxygen vacancies are represented by (red) filled circles.*[22]

We have used two slightly different layers structure of $SrTiO_3/SrCuO_2/LaAlO_3/SrTiO_3$ heterostructures, labelled as sample S2 and sample S3 for our measurements (sample S1 was measured previous to this work). These samples are grown by pulsed laser deposition (PLD) using stoichiometric and single-crystalline $LaAlO_3$ (LAO), $SrCuO_2$ (SCO) and $SrTiO_3$ (STO) targets. These two samples have the same basic structure, as illustrated in Fig. 5.1(b), but differ slightly in the number of LAO layers deposited and the background oxygen pressure during the growth. The samples consist of nine (S2) or ten (S3) monolayers of LAO deposited on a good quality TiO_2-terminated single crystal STO [001] substrate,[14] and then capped by a monolayer of SCO and two monolayers of STO. For sample S2, 9 monolayers of LAO are deposited at 2×10^{-3} mbar oxygen pressure, and for sample S3, 10 monolayers of LAO are grown at reduced oxygen pressure of 1×10^{-5} mbar, while keeping the same substrate temperature at 850°C for both S2 and S3. The samples were cooled from 850°C to 600°C in the LAO layer growth pressure, and a monolayer of SCO and two monolayers of STO were then deposited at 600°C in 6×10^{-2} mbar of oxygen. The growth of atomically-sharp layers from each of the materials was monitored in-situ using reflection high-energy electron diffraction (RHEED).[15] The other general PLD deposition parameters like fluence of laser pulse, spot size, repetition rate and details about the in situ RHEED monitoring procedure were discussed in chapter 2. After the growth, the samples were cooled to room temperature in the deposition pressure of the STO monolayers, at a rate of 10°C/min.

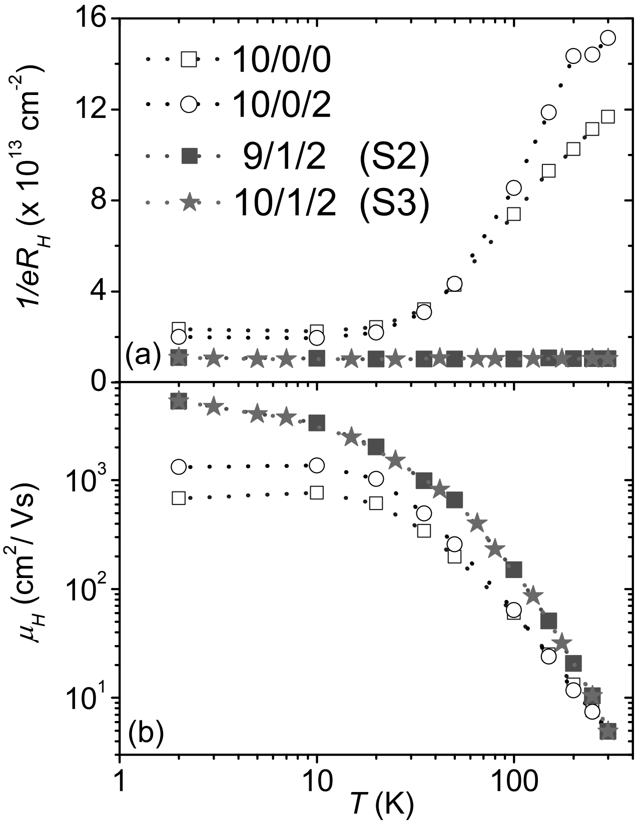

Figure 5.2: *Transport properties of* $LaAlO_3/SrTiO_3$ *heterostructures with (closed symbols) or without (open symbols) a* $SrCuO_2$ *layer performed in a magnetic field up to 2 T. (a) Temperature dependence of inverse Hall coefficient* $1/R_He$*, indicating the carrier density, and (b) Hall mobility* μ_H*. Various heterostructures layers structure are given, for example 9/1/2 represents a 9 u.c.* $LaAlO_3$ *with a 1 u.c.* $SrCuO_2$ *and a 2 u.c. thick* $SrTiO_3$ *top layer, the dotted lines are guides to the eye.*

5.2.1 Influence of capping layers

It is known that the properties of the LAO/STO interface depends on external factors such as the growth conditions of the LAO layers,[3] the LAO layer thickness,[9,16,17] and any treatment of the LAO surface.[18] It is therefore to be expected that capping layers affect the interface properties. Both theoretical (bandstructure calculations) and experimental results reported previously show that STO capping layers significantly modify the bandgap at the LAO/STO interface.[19–21] As a result of this band structure modification, the LAO/STO interface becomes conducting for the growth of 2 LAO layers, which is below the critical thickness of 4 LAO layers usually necessary for conductivity without STO capping layers.[20] Additionally, STO capping also serves to protect the LAO surface by reducing its sensitivity to surface adsorbates or defects. In the present case with S2 and S3, we introduce an additional SCO layer between the LAO and STO top layers and we study its influence on the transport properties of the LAO/STO interface.

The influence of capping layers (STO and SCO) on the transport properties of the LAO/STO interface, performed in a magnetic field up to 2 T in a physical properties measurement system, were reported by Huijben et al.[22] Measurements we performed on other similar samples reproduced same results, and these are presented in Fig. 5.2. Fig. 5.2(a) shows the comparison of the temperature dependence of the inverse Hall coefficient $1/R_H e$ (related to the carrier density by $R_H = B/n\,|e|$) and the Hall mobility μ_H of the carriers for LAO/STO interfaces with and without capping layers. The LAO/STO sample (Fig. 5.1(a)) without any cap (□) shows strong carrier freeze out on cooling, from $\sim 1.2 \times 10^{14}$ cm^{-2} at 300 K to $\sim 2.4 \times 10^{13}$ cm^{-2} at 2 K. The LAO/STO with only an STO cap (○) shows still a carrier freeze out from $\sim 1.5 \times 10^{14}$ cm^{-2} at 300 K to $\sim 2 \times 10^{13}$ cm^{-2} at 2 K, whereas the LAO/STO samples (S2 and S3) with SCO and STO caps (closed symbols) show a temperature independent carrier density of $\sim 1 \times 10^{13}$ cm^{-2} between 2 K and 300 K. Therefore the presence of the SCO layer greatly reduces the carrier freeze-out compared to the samples prepared in an identical way, but without an SCO layer.

It is also evident from Fig. 5.2(b) that the presence of an SCO layer increases the Hall mobility of the carriers at the LAO/STO interface compared to samples without an SCO layer.[22] The lower values for Hall mobility of the LAO/STO interface without an SCO capping layer might be due to additional scattering of conduction carriers (blue arrow) by the oxygen vacancies (filled red circles) as illustrated in Fig. 5.1(a). The increase in the Hall mobility of the interface carriers after introduction of a monolayer of SCO has been attributed to the effective elimination of oxygen vacancies from the conduction path of carriers, as illustrated in Fig. 5.1(b).[22] We also observed that samples S2 and S3 are also less dependent on the growth conditions of the LAO layer, especially to the oxygen pressure during deposition, compared the uncapped LAO/STO samples.[3, 12, 19–22]

We performed magnetotransport experiments on such high-mobility samples (S2 and S3) at low-temperatures, down to 70 mK, in high magnetic fields up to 30 T. These measurements were performed in a pumped ^{3}He system and in a dilution refrigerator with a rotatable sample stage, using samples of dimensions $5 \times 5 \times 0.5$ mm^3. The samples were mounted on a ceramic chip carrier and electrical contacts were made by ultrasonically wire-bonded aluminium wires. The longitudinal resistivity (ρ_{xx}) and Hall resistivity (ρ_{xy}) were measured in van der Pauw geometry following the similar procedure explained in chapter 2 (section 2.3.1). The reminder of this chapter describes our magnetotransport results on these high-mobility samples.

5.3 Experimental results

Figs. 5.3(a) and (c) show the ρ_{xx} data of samples S2 and S3 at various temperatures, for the applied magnetic field orientation perpendicular to the LAO/STO interface. Figs. 5.3(b) and (d) show the same data as in (a) and (c), but after removing a smooth background. The process of background subtraction for both the samples is exemplified as a dashed line in the insets of figures 3(b) and (d). SdH oscillations with strongly temperature-dependent amplitudes are evident for both the samples. The oscillations clearly do not come from a single frequency but rather suggests a superposition of multiple frequencies.

Figs. 5.3(e) and (f) show ρ_{xy} of samples S2 and S3 at various temperatures, which is found to be approximately linear in field and temperature independent with signs of oscillations. After subtraction of the approximately linear background from ρ_{xy} clear quantum oscillations are observed, similar to those in ρ_{xx}. The SdH oscillations observed in ρ_{xy} for the sample S3 are shown in inset of Fig. 5.3(e). Apart from the oscillation amplitudes, ρ_{xy} is largely temperature independent. Similar ρ_{xy} behaviour in field is also observed for sample S2. We performed the usual antisymmetrization procedure on the Hall effect data, by measuring ρ_{xy} in both positive and negative field polarities. From that we exclude crosstalk between ρ_{xx} in ρ_{xy} or vice versa as the possible source of oscillations in ρ_{xy}. The observed quantum oscillations in ρ_{xy} can be explained from the contribution of several subbands similar to the oscillations as in ρ_{xx}.[23] These several subbands also contribute to Hall conductivity σ_{xy} which, via the tensor inversion, gives rise to the SdH effect in ρ_{xy}.

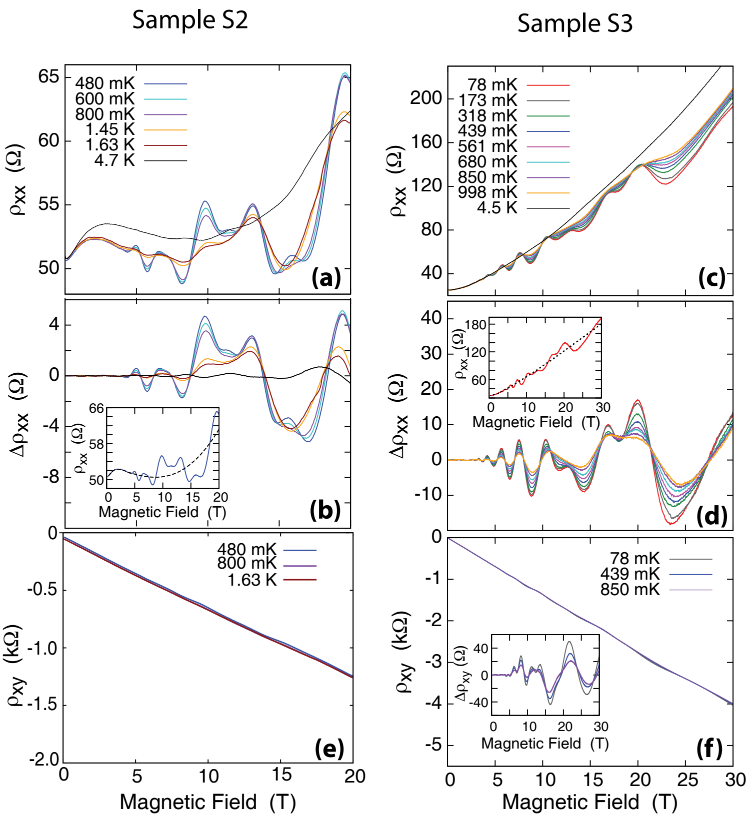

Figure 5.3: *(a)-(d): Longitudinal resistivity ρ_{xx} raw data (a,c) and the oscillations $\Delta\rho_{xx}$ with background removed (b,d) of the samples S2 and S3, with the magnetic field-orientated perpendicular to the oxide layers. An example of the background subtracted in each case is shown as dashed line in the insets of b and d. (e)-(f): Hall resistivity of samples S2 and S3. The inset in (f) shows the quantum oscillations after subtraction of the linear background.*[12]

Figs. 5.4(a) and (b) show the angle dependence of SdH oscillations in ρ_{xx} for a range of magnetic field orientations, from perpendicular to parallel to the oxide layers for S2 and S3. The angle θ is between the magnetic field direction and normal to the plane of the LAO/STO interface (as shown in Fig. 5.4(c)). The SdH oscillation amplitudes are strongly suppressed along with an irregular change in their periodicity, as the sample is tilted to higher angles (away from perpendicular field, $\theta = 0^o$) in the magnetic field. For sample S2, ρ_{xx} changes from positive to negative, with a pronounced step-like feature in parallel magnetic field ($\theta = 90^o$) at ∼11 T. For S3, tilting the sample in magnetic field to higher angles up to 30^o has a similar influence as in S2.

5.4 Data analysis and discussion

In order to perform analysis of the magnetotransport (ρ_{xx}) results from samples S2 and S3 in the perpendicular magnetic field orientation ($\theta = 0^o$), we use the concepts discussed in chapter 2 (section 2.3.3). From the results for S2 and S3 (Figs. 5.3(a) and (c)), it is evident that the SdH oscillation amplitude in the raw data of ρ_{xx} is only about 10% of the total background resistivity. For a 2D electron system with fully quantized Landau-levels the oscillatory component

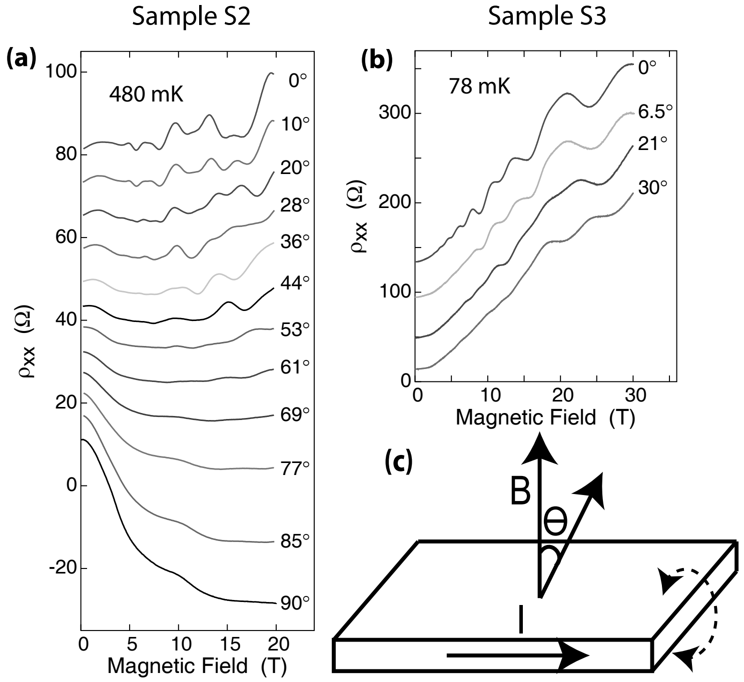

Figure 5.4: *Dependence of SdH oscillations on magnetic field-orientation. The angle θ between the magnetic field direction and the normal to the interface is shown beside each of the curves. (a) SdH oscillations at different tilt angles for sample S2, (b) SdH oscillations at different tilt angles for sample S3. The curves in both the figures are offset on the y-axis for clarity.*[12] *(c) Schematic of sample rotation (θ) for magnetic field-orientation-dependent magnetotransport measurements (B-magnetic field and I-bias current).*

of ρ_{xx} becomes zero and the component of ρ_{xy} shows plateaus (Quantum Hall effect) at high magnetic fields. This is not the case with our ρ_{xx} and ρ_{xy} measurements for S2 and S3, which means that the Landau-levels are not fully resolved, i.e., there still exists considerable overlap of the levels (high m^*, see equation 2.16). Due to the presence of such Landau-level structure, the SdH oscillations are sinusoidal in inverse magnetic field 1/B, and are described by the general expression obtained from equation 2.17 (section 2.3.3) of chapter 2,[23, 24]

$$\Delta\rho_{xx}(B,T) \propto \sum_i \exp(-\alpha_i T_{D_i}) \frac{\alpha_i T}{\sinh(\alpha_i T)} \ \sin\left(\frac{2\pi f_i}{B} + \phi_i\right), \tag{5.1}$$

where T is the temperature, and f and ϕ are the frequency and phase of the oscillations. The amplitude factors contain the term $\alpha = 2\pi^2 k_B m^*/\hbar e B$, and allow the effective mass m^*, and Dingle temperature T_D of the charge carriers to be extracted from the temperature and magnetic field dependence of the signal.[23] T_D is a measure of quantum mobility μ_i, and can expressed as $T_D = (e\hbar/2\pi k_B)(1/m^*\mu_i)$.

After carefully subtracting the smooth background from each curve of the ρ_{xx} raw data, we have obtained the pure oscillatory $\Delta\rho_{xx}(B,T)$ component as shown in Figs. 5.3(b) and (d). We have performed Fourier transforms (FTs) on $\Delta\rho_{xx}(B,T)$ in the inverse magnetic field, and the results are shown in Figs. 5.5(a) and (b). The resulting Fourier spectra for S2 shows four peaks and for S3 shows five peaks, corresponding, to respectively, four and five distinct frequencies of SdH oscillations. This means that four (S2) and five (S3), high-mobility conduction subbands contribute to the transport in these samples in the quantum regime. The difference in the number of subbands between the samples S2 and S3 could be due to the smaller magnetic field range used for S2 (up to 20 T) or difference in the oxygen growth pressure or number of LAO layers.

The temperature dependence of the amplitude of the FT peaks is fitted with the α_iT/sinh(α_iT) as shown in Figs. 5.5(c) and (d). For both the samples S2 and S3, the experimental temperature dependence of all the frequencies is well described by theoretical curves. The resulting carrier effective masses m^* extracted from the fits are given in Figs. 5.5(c) and (d), the errors in the m^* come from the uncertainties involved in Fourier transforming over a wide magnetic field range, rather than the quality of the fits. The obtained frequencies f_i and carrier effective masses m_i^* of the multiple subbands for S2 and S3 are given in the table 5.1.

To check our Fourier analysis, we directly calculated the oscillatory $\Delta\rho_{xx}(B,T)$ of sample S2 with expression (5.1) using the frequencies f_i (Fig. 5.5(a)), the

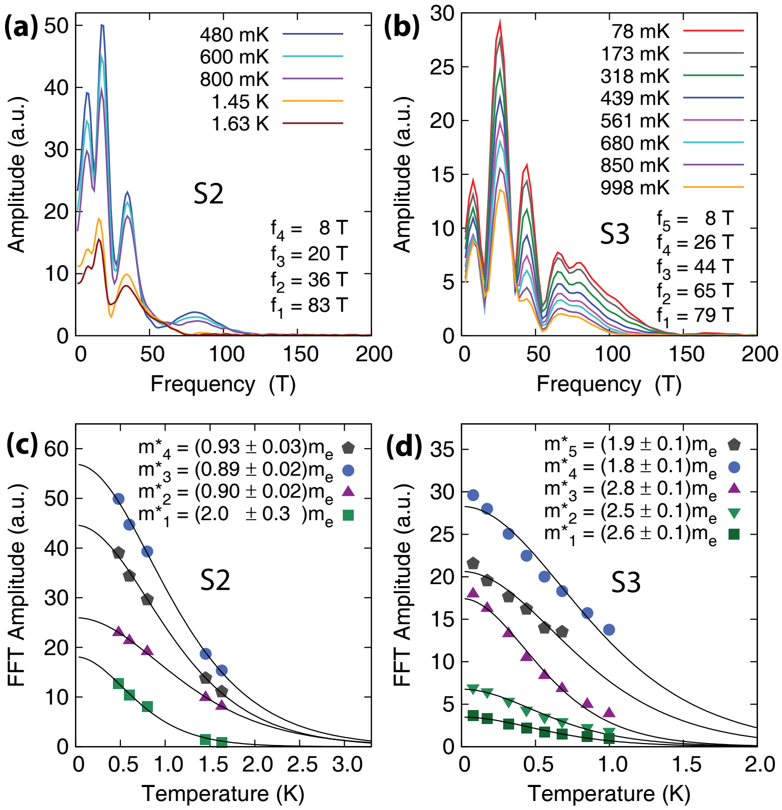

Figure 5.5: *(a) Fourier transform between 4 and 20 T for S2. (b) Fourier transform between 4 and 30 T for S2. (c)-(d) Temperature-dependence of the oscillation amplitudes with values of m^* in units of m_e. The solid lines are fits to $\alpha_i T/\sinh(\alpha_i T)$. Some of the data are rescaled so that all the data for both the samples can be shown clearly on a single plot.*[12]

carrier effective masses m_i^* (Fig. 5.5(c)) and the Dingle temperatures T_{Di} from four subbands. The overall field-independent amplitude R_1 and $R_2 = R_3 = R_4$ (since $m_2 = m_3 = m_4$) are the only two fit parameters used, while keeping phase of oscillations fixed at $\phi_i = \pi/4$. The fit is shown in Fig. 5.6 as a solid line, and reproduces the experimental data of sample S2 very well except at very low field. For the case of sample S3, the SdH oscillations start to appear just below 2 T, that means the mobility of at-least one subband is higher than in S2. In this situation, the overlap of adjacent Landau-levels is either very small or non-existent, this gives rise to SdH oscillations in 1/B, where the expression

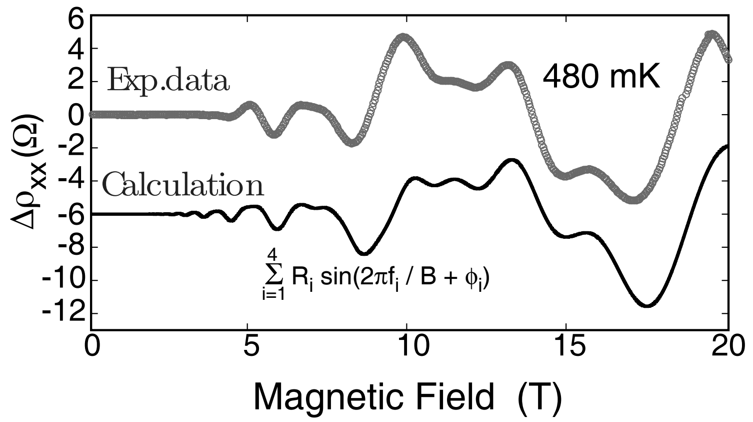

Figure 5.6: *Fit of expression (5.1) to $\Delta\rho_{xx}$ for the sample S2 using f_i, m_i^* and T_{Di} from the Fourier transforms. The (blue) circles show the measured data, and the solid line represent the calculation.*[12]

(5.1) is no longer valid.

The SdH oscillation results of samples S2 and S3 provide sufficient confirmation of the 2D nature of the conduction subbands at the LAO/STO interface, which we will discuss later in this chapter. For a 2D electron system with parabolic conduction bands and circular cross-sections of the Fermi surface, from the frequency of SdH oscillations can be used to calculate, the carrier density (n_i) in a given subband using the relation, $n_i = N_v N_s e f_i / h$. The corresponding subband energies with respect to the Fermi energy can be calculated using the relation, $E_F - E_i = n_i \pi \hbar^2 / m_i^*$. The obtained values for n_i and $E_F - E_i$ for different subbands of the samples S2 and S3 are given in the table 5.1.

The total carrier density that is contributing to the SdH oscillations is similar for both S2 and S3: $n_{SdH} = \sum\limits_i n_i \sim 1 \times 10^{13}$ cm^{-2}. The obtained carrier density n_{SdH} for S2 and S3 is higher than the previously measured values in LAO/STO without capping layers,[10,11] where the SdH oscillations were originating from a single occupied interface subband. Similar carrier densities of 1×10^{13} cm^{-2} with several occupied subbands a few meV below the Fermi energy has been observed for the electric-field-induced surface 2DEGs in bulk pristine STO single crystals.[38] The quantum oscillations measured from δ-doped STO reveal frequencies and effective masses in a similar range to those we observe in LAO/STO, and imply a similar energy scale for the subband structure.[39,40]

Fig. 5.7 shows the calculated subband energies ($E_F - E$) versus the density states for both of our samples. The notable aspect of these subband structures is the small energy scale involved. The lowest energy subband edge is only a few meV below the Fermi energy in both the samples, and the separation between the subbands is ~ 1 meV or less. Our experimental observation of several conduction subbands is in agreement with theoretical predictions of multiple subband occupancy at the interface of LAO/STO heterostructures.[34] However, our observations of a small energy scale of few meV is in disagreement with the theoretical calculations related to the interface bandstructure, which predict subband energy separations in the range of tens to hundreds of meV.[31,32] The observed relatively weak confining interface potential implied by the few meV subband energies may also be responsible for the observed lower than expected conducting interface Ti-2p core-level shifts in photoemission spectroscopic studies.[34–37]

Now we focus on ρ_{xx} measured in tilted magnetic fields for samples S2 and S3. The measurements of ρ_{xx} for S2 as the magnetic field-orientation is rotated from perpendicular ($\theta = 0^o$) to parallel ($\theta = 90^o$) to the LAO/STO interface are shown in Fig. 5.4(a). The SdH oscillations are strongly suppressed as θ is increased to higher angles, which means that the conduction electrons are confined to the interface plane.

Table 5.1: *Subband properties derived from analysis of SdH oscillations in two samples S2 and S3: SdH frequency f; effective mass m^*; carrier density n; subband energy relative to the Fermi energy $E_F - E$.*

Sample	m^* (m_e)	n (10^{12}cm^{-2})	$E_F - E$ (meV)
S2			
$f_1 = 83$ T	2 (±0.3)	4.0	4.8
$f_2 = 36$ T	0.9 (±0.1)	1.7	4.5
$f_3 = 20$ T	0.9 (±0.1)	1.0	2.6
$f_4 = 8$ T	0.9 (±0.1)	0.4	1.0
S3			
$f_1 = 79$ T	2.6 (±0.2)	3.8	3.5
$f_2 = 65$ T	2.5 (±0.2)	3.1	3.0
$f_3 = 44$ T	2.8 (±0.2)	2.1	1.8
$f_4 = 26$ T	1.8 (±0.2)	1.3	1.7
$f_5 = 8$ T	1.9 (±0.2)	0.4	0.5

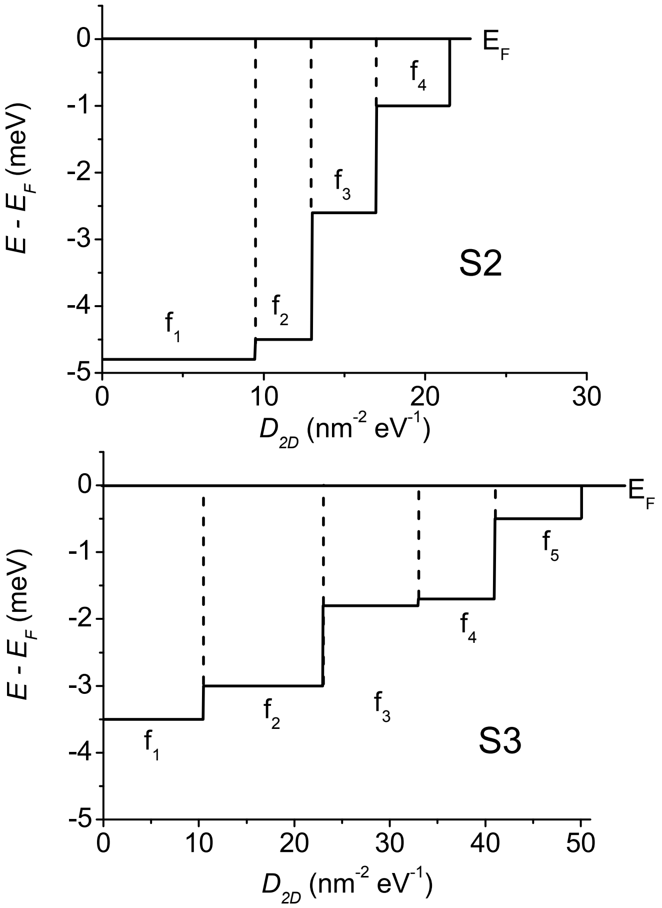

Figure 5.7: *Density of states $D_{2D}(E)$ for the multi-subband 2DEG in our two samples S2 and S3 extracted from the analysis of the SdH oscillations.*[12]

This shows that the SdH oscillations are arising only due to the perpendicular magnetic field component, and is a clear indication of the 2D nature of the interface carriers. For a 2D electron system, the period of the SdH oscillations is expected to scale with $1/\cos(\theta)$, since the Landau-level degeneracy depends only on the perpendicular magnetic field component as illustrated in chapter 2 (Fig. 2.9). When multiple 2D subbands are occupied and Landau levels are not fully resolved, the scaling of the SdH oscillations deviates from $1/\cos(\theta)$, and becomes more complex with the tilted field. This complex behaviour is a consequence of anti-crossing of the discrete levels from different subbands as the field is tilted.[25] As a result the Landau-level energies show complicated field dependence and corresponding modification of SdH oscillations in the tiled magnetic fields. Our results on S2 and S3 show the periodicity of oscillations do not scale with $1/\cos(\theta)$, rather shows complex dependence of the periodicity as θ is increased. This further confirms the contribution of multiple occupied 2D subbands to the magnetotransport.

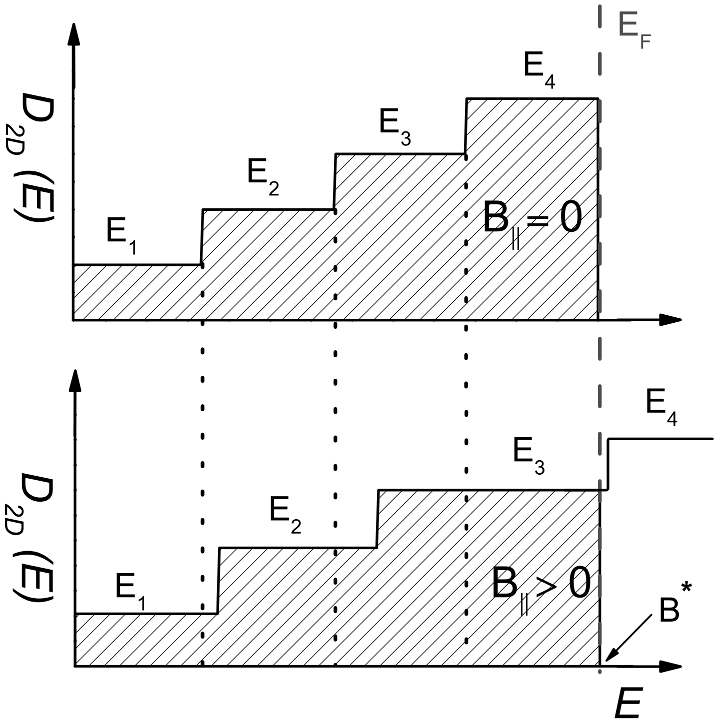

Figure 5.8: *Schematic of four occupied subband E_i density of states $D_{2D}(E)$ up to the Fermi energy E_F (vertical dashed line) for the magnetic field-oriented perpendicular $B_\parallel = 0$ to the interface, and depopulation of highest subband at B^* for the applied magnetic field is oriented parallel $B_\parallel > 0$ to the interface. The individual subband edges move to higher energy (see Eq. 5.2) with the in-plane magnetic field $B_\parallel > 0$, indicated as vertical dotted lines.*

Fig. 5.4(a) shows that in parallel magnetic field ($\theta = 90^o$), ρ_{xx} of sample S2 decreases as a function of magnetic field, giving rise to a significant drop of the resistance accompanied by a step like feature at $\sim$ 11 T. Similar behaviour is observed in conventional semiconductor 2D electron systems with multiple subbands occupied.[25,26] This is a consequence of the shifting of confinement energies for 2D electrons, called 'diamagnetic shift'ΔE_n with the increase in the parallel field component at higher tilt angles ($\theta > 0$), and is given by:

$$\Delta E_n = \frac{e^2 B_{\parallel}^2}{2m_n^*} \mid <z_n^2> - <z_n>^2 \mid , \tag{5.2}$$

where the final term is the square of the electron wavefunction in the confinement direction for the n^{th} subband.[26] We explain the step like decrease of the resistance in parallel magnetic field by tentatively considering a simplified subband structure for the 2DEG in sample S2, as schematically depicted in Fig. 5.8. When no in-plane magnetic field is applied $B_{\parallel} = 0$, four subbands are occupied up to the Fermi energy E_F (vertical dashed line). For the case of parallel magnetic field $B_{\parallel} > 0$, at a certain value of magnetic field B^* the highest occupied subband is moved across E_F and the carriers are accumulated in the three lower subbands (Fig. 5.8). As a result of the highest occupied subband shifting across the Fermi energy, it depopulates completely and is not accessible to scattering processes (increase in carrier mobility). This leads to the reduction of the contribution of inter-subband scattering to the total resistance giving rise to a step-like decrease of ρ_{xx}.[27,28]

Now we focus on the results of ρ_{xy}. When multiple subbands are contributing to the transport, it is not straightforward to extract the total carrier density from the Hall effect data to compare with the densities obtained from SdH results. However it is possible to calculate the expected Hall effect in a multi-subband system from the carrier densities (n_i) and mobilities (μ_i) of each subband using the following expression,[29] which is an extension of the Hall effect formula used for the two subbands of carriers contributing to the transport discussed in chapters 3 and 4 :

$$\rho_{xy}(B) = \frac{B}{e} * \frac{\left(\frac{n_1\mu_1^2}{1+(\mu_1 B)^2} + \frac{n_2\mu_2^2}{1+(\mu_2 B)^2} + ...\right)}{\left(\frac{n_1\mu_1}{1+(\mu_1 B)^2} + \frac{n_2\mu_2}{1+(\mu_2 B)^2} + ...\right)^2 + B^2\left(\frac{n_1\mu_1^2}{1+(\mu_1 B)^2} + \frac{n_2\mu_2^2}{1+(\mu_2 B)^2} + ...\right)^2}. \tag{5.3}$$

The calculated $\rho_{xy}(B)$ from expression (5.3) using the n_i and μ_i of four different subbands obtained from the SdH results for the sample S2 is shown in Fig. 5.9, as a dotted line. It is evident from Fig. 5.9, that there is some discrepancy between the calculated and the experimental data of $\rho_{xy}(B)$ over the full magnetic field range. However, the disagreement between the carrier den-

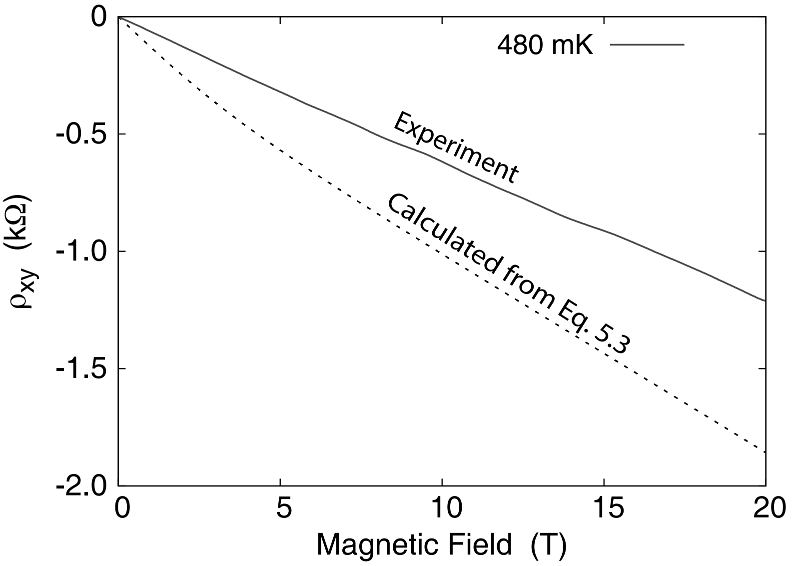

Figure 5.9: *Hall effect at 480 mK for S2 shown as solid line. The dotted line show the expected Hall effect for S2 calculated using the multi-band model (Eq. 5.3), the carrier densities n_i and mobilities μ_i for the four subbands (given in the table 5.1) are extracted from the SdH oscillations analysis.*

sity obtained from SdH oscillations in this work, and the Hall effect is small compared to previous results.[10,11] The discrepancy we observe could mean that there are fewer occupied subbands contributing to the SdH oscillations compared to $\rho_{xy}(B)$ in the measured magnetic field range. Otherwise the inter-subband scattering contribution should be taken into consideration in order to fully explain the Hall effect data of S2 and S3,[30] which is beyond the scope of this work. These experimental observations of the multi-subband occupancy at the interface of LAO/STO heterostructures are in agreement with theoretical predictions.[31,32] The results summarised in the table 5.1 show that there are small differences between the samples S2 and S3, which could be due to the slight difference in the growth conditions of LAO layers or in their number.

It is well established that the bulk STO conduction bandstructure consists of three degenerate bands originating from the Ti-3d xy, yz and xz orbitals with a minimum at Γ-point of the Brillouin zone. The degeneracy of these bulk bands is lifted due to low temperature structural transition and spin-orbit coupling.[41] Further formation of 2D subbands is expected at the LAO/STO interface due to the confinement potential, and arises from the compensation for internal electric field with the growth of polar-LAO layers.[42]

Earlier theoretical work based on a high interface carrier density of 3.4×10^{14} cm^{-2} (based on full electronic reconstruction scenario) revealed that the interface subbands derived from d_{xy} orbitals, have light masses with circular Fermi surfaces symmetric in the interface plane. The subbands derived from d_{yz} or d_{xz} have heavy masses with elliptical Fermi-surfaces weakly dispersing in one-of the interface planes.[31,32]

Recent band structure calculations by Khalsa and MacDonald,[33] and van Heeringen et al.,[34] shows clearly how the energy spacing (and ordering) of the subbands depends largely on the confinement potential at the interface, which in turn depends on the carrier density of the system. These calculations show that for low carrier density 1×10^{13} cm^{-2} the 2D interface subbands are much more closely spaced with separation in the order of few meV between the lowest occupied subbands. At the same time the 2D subbands hybridise at the interface so that many of them have mixed orbital character and are not pure d$_{xy}$ or d$_{yz/xz}$.

The carrier densities we observe experimentally for the samples S2 and S3 are $\sim 1 \times 10^{13}$ cm^{-2}, and indicate closely spaced 2D subbands. Similarly, the electron effective masses we observe for the samples (S2 and S3) are in the range from $\sim$ 1-3 m_e, and indicate that we are measuring masses of hybridised subbands with mixed orbital character resulting in masses between light and heavy. The difference in the masses observed for different subbands in S2 and S3, could be due to the difference in degree of hybridization in a specific sample.

The theoretical work by van Heeringen el al.,[34] is in good agreement with our experimental observations reported in this chapter for sample S2. These calculations were performed by assuming a low carrier density of 7.2×10^{12} cm^{-2}, a resulting weak interface confining electric field of 0.1 meV/Å and meV spaced subbands. They found out that several non-parabolic, anisotropic 2D subbands at the interface are occupied, having mixed orbital character, and separated by a few meV, with different effective masses. The effective masses (1.5 m_0, 0.5 m_0, 0.5 m_0, 0.5 m_0) calculated are in the similar order of magnitude observed experimentally (table 5.1) in the sample S2 (Fig. 5.5(c)) with decreasing frequency (Fig. 5.5(a)).

5.5 Summary

We have performed magnetotransport on SrTiO$_3$/SrCuO$_2$/LaAlO$_3$/SrTiO$_3$ heterostructures with high-mobility interface carriers and measured the SdH oscillations in $\rho_{xx}(B)$. The STO and SCO capping layers increase the electronic quality of the LAO/STO interface by increasing the carrier mobility and making it less sensitive to the oxygen growth pressure, compared to the uncapped LAO/STO interfaces. The analysis of our SdH results reveals multiple 2D conduction subbands with different effective masses and mobilities present at the LAO/STO interface are contributing to the quantum transport. This is confirmed by the complex magnetic field-orientation-dependent SdH oscillations. By comparing our effective mass results ($\sim$ 1-3 m_e) with the recent theoretical work by van Heeringen el al., we say that the hybridization of the subbands at the interface with mixed Ti $3d$ orbital character is responsible for the observed interface electronic properties.

References

[1] A. Ohtomo and H. Y. Hwang, Nature (London) **427**, 423 (2004).

[2] N. Reyren, S. Thiel, A. D. Caviglia, L. F. Kourkoutis, G. Hammerl, C. Richter, C. W. Schneider, T. Kopp, A. S. Ruetschi, D. Jaccard, M. Gabay, D. A. Muller, J.-M. Triscone, and J. Mannhart, Science **317**, 1196 (2007).

[3] A. Brinkman, M. Van Zalk, J. Huijben, U. Zeitler, J. C. Maan, W. G. Van der Wiel, G. Rijnders, D. H. A. Blank, and H. Hilgenkamp, Nature Mater. **6**, 493 (2007).

[4] M. Ben Shalom, C. W. Tai, Y. Lereah, M. Sachs, E. Levy, D. Rakhmilevitch, A. Palevski, and Y. Dagan, Phys. Rev. B **80**, 140403 (2009).

[5] Ariando, X. Wang, G. Baskaran, Z. Q. Liu, J. Huijben, J. B. Yi, A. Annadi, A. R. Barman, A. Rusydi, S. Dhar, Y. P. Feng, J. Ding, H. Hilgenkamp, and T. Venkatesan, Nature Comm. **2**, 188 (2011).

[6] D. A. Dikin, M. Mehta, C. W. Bark, C. M. Folkman, C. B. Eom, and V. Chandrasekhar, Phys. Rev. Lett. **107**, 056802 (2011).

[7] L. Li, C. Richter, J. Mannhart, and R. C. Ashoori, Nature Phys. **7**, 762 (2011).

[8] J. A. Bert, B. Kalisky, C. Bell, M. Kim, Y. Hikita, H. Y. Hwang, and K. A. Moler, Nature Phys. **7**, 767 (2011).

[9] S. Thiel, G. Hammerl, A. Schmehl, C. W. Schneider, and J. Mannhart, Science **313**, 1942 (2006).

[10] M. Ben Shalom, A. Ron, A. Palevski, and Y. Dagan, Phys. Rev. Lett. **105**, 206401 (2010).

[11] A. D. Caviglia, S. Gariglio, C. Cancellieri, B. Sacepe, A. Fete, N. Reyren, M. Gabay, A. F. Morpurgo, and J.-M. Triscone, Phys. Rev. Lett. **105**, 236802 (2010).

[12] A. McCollam, S. Wenderich, M. K. Kruize, V. K. Guduru, H. J. A. Molegraaf, M. Huijben, G. Koster, D. H. A. Blank, G. Rijnders, A. Brinkman, H. Hilgenkamp, U. Zeitler, and J. C. Maan, Appl. Phys. Lett.: Materials **2**, 022102 (2014).

[13] A. Tsukazaki, A. Ohtomo, T. Kita, Y. Ohno, H. Ohno, and M. Kawasaki, Science **315**, 1388 (2007).

[14] G. Koster, B. L. Kropman, G. J. H. M. Rijnders, D. H. A. Blank, and H. Rogalla, Appl. Phys. Lett. **73**, 2920 (1998).

[15] G. J. H. M. Rijnders, G. Koster, D. H. A. Blank, and H. Rogalla, Appl. Phys. Lett. **70**, 1888 (1997).

[16] C. Bell, S. Harashima, Y. Hikita, and H. Y. Hwang, Appl. Phys. Lett. **94**, 222111 (2009).

[17] F. J. Wong, R. V. Chopdekar, and Y. Suzuki, Phys. Rev. B **82**, 165413 (2010).

[18] Y. Xie, Y. Hikita, C. Bell, and H. Y. Hwang, Nature Comm. **2**, 494 (2011).

[19] R. Pentcheva, M. Huijben, K. Otte, W. E. Pickett, J. E. Kleibeuker, J. Huijben, H. Boschker, D. Kockmann, W. Siemons, G. Koster, H. J. W. Zandvliet, G. Rijnders, D. H. A. Blank, H. Hilgenkamp, and A. Brinkman, Phys. Rev. Lett. **104**, 166804 (2010).

[20] M. Huijben, G. Rijnders, D. H. A Blank, S. Bals, S. van Aert, J. Verbeeck, G. van Tendeloo, A. Brinkman, and H. Hilgenkamp, Nature Mater. **5**, 556 (2006).

[21] M. Huijben, A. Brinkman, G. Koster, G. Rijnders, H. Hilgenkamp, and D. H. A Blank, Adv. Mater. **21**, 1665 (2009).

[22] M. Huijben, G. Koster, M. K. Kruize, S. Wenderich, J. Verbeeck, S. Bals, E. Slooten, B. Shi, H. J. A. Molegraaf, J. E. Kleibeuker, S. van Aert, J. B. Goedkoop, A. Brinkman, D. H. A. Blank, M. S. Golden, G. van Tendeloo, H. Hilgenkamp, and G. Rijnders, Adv. Funct. Mater. **23**, 5240 (2013).

[23] D. Shoenberg *Magnetic Oscillations in Metals* (Cambridge University Press, 1984).

[24] I. M. Lifshitz and A. M. Kosevich, Sov. Phys. JETP **2**, 636 (1956).

[25] J. C. Maan, in *Springer Series in Solid State Sciences 53*, edited by G. Bauer, F. Kuchar, and H. Heinrich (Springer Berlin, 1984) p 183.

[26] W. Beinvogl, A. Kamgar, and J. F. Koch, Phys. Rev. B **14**, 4274 (1976).

[27] T. Englert, J. C. Maan, D. C. Tsui, and A. C. Gossard, Solid State Commun. **45**, 989 (1983).

[28] J. C. Portal, R. J. Nicholas, M. A. Brummell, A. Y. Cho, K. Y. Cheng, and T. P. Pearsall, Solid State Commun. **43**, 907 (1982).

[29] N. W. Ashcroft and N. D. Mermin, *Solid State Physics* (Harcourt Brace College Publishers, 1976) page number 240.

[30] E. Zaremba, Phys. Rev. B **45**, 14143 (1992).

[31] Z. S. Popović, S. Satpathy, and R. M. Martin, Phys. Rev. Lett. **101**, 256801 (2008).

[32] W.-j. Son, E. Cho, B. Lee, J. Lee, and S. Han, Phys. Rev. B **79**, 245411 (2009).

[33] G. Khalsa and A. H. MacDonald, Phys. Rev. B **86**, 125121 (2012).

[34] L. W. van Heeringen, G. A. de Wijs, A. McCollam, J. C. Maan, and A. Fasolino, Phys. Rev. B **88**, 205140 (2013).

[35] K. Yoshimatsu, R. Yasuhara, H. Kumigashira, and M. Oshima, Phys. Rev. Lett. **101**, 026802 (2008).

[36] M. Takizawa, S. Tsuda, T. Susaki, H. Y. Hwang, and A. Fujimori, Phys. Rev. B **84**, 245124 (2011).

[37] E. Slooten, Z. Zhong, H. J. A. Molegraaf, P. D. Eerkes, S. de Jong, F. Massee, E. van Heumen, M. K. Kruize, S. Wenderich, J. E. Kleibeuker, M. Gorgoi, H. Hilgenkamp, A. Brinkman, M. Huijben, G. Rijnders, D. H. A. Blank, G. Koster, P. J. Kelly, and M. S. Golden, Phys. Rev. B **87**, 085128 (2013).

[38] K. Ueno, S. Nakahara, H. Shimotani, A. Ohtomo, N. Kimura, T. Nojima, H. Aoki, Y. Iwasa, and M. Kawasaki, Nat. Mater. **7**, 855 (2008).

[39] Y. Kozuka, M. Kim, C. Bell, B. G. Kim, Y. Hikita, and H. Y. Hwang, Nature **462**, 487 (2009).

[40] M. Kim, C. Bell, Y. Kozuka, M. Kurita, Y. Hikita, and H. Y. Hwang, Phys. Rev. Lett. **107**, 106801 (2011).

[41] L. F. Mattheiss, Phys. Rev. B **6**, 4740 (1972).

[42] A. F Santander-Syro, O. Copie, T. Kondo, F. Fortuna, S. Pailhès, R. Weht, X. G. Qiu, F. Bertran, A. Nicolaou, A. Taleb-Ibrahimi, P. Le Fèvre, G. Herranz, M. Bibes, N. Reyren, Y. Apertet, P. Lecoeur, A. Barthélémy, and M. J. Rozenberg, Nature (London) **469**, 189 (2011).

Chapter 6

Magnetic scattering in $LaAlO_3/SrTiO_3$ heterostructures measured by a negative magnetoresistance

Abstract

We have performed magnetotransport measurements to investigate the nature of magnetic scattering in $LaAlO_3/SrTiO_3$ *heterostructures in high magnetic fields (up to 30 T), at temperatures below 4 K. The low-temperature sheet resistance shows a logarithmic temperature-dependence accompanied by a large negative magnetoresistance. We attribute the origin of negative magnetoresistance to the scattering of conduction charge carriers from localized magnetic moments: the external magnetic field orients these moments thereby reducing scattering, which results in a decrease of resistance. The analysis of our results indicates the presence of magnetic moments, which are coupled antiferromagnetically via the interface conduction electrons at an energy scale of 40* μ*eV.*

Part of this chapter has been submitted as correspondence to the earlier work published by A. Brinkman et al., in Nature Materials 6, 493 (2007).

6.1 Introduction

Some fundamental properties of the conducting interface[1] between the two band-insulating perovskite oxides $SrTiO_3$ (STO) and $LaAlO_3$ (LAO), such as tunable switching of high mobility interface conductivity by means of UV-illumination and temperature (chapters 3 and 4), and quantum oscillations with 2D character (chapter 5) are discussed earlier in this thesis. Here we focus on the magnetic behaviour, which was first reported by Brinkman et al.,.[2] Though superconductivity[3] and SdH oscillations[4] can be realized by doping bulk pristine $SrTiO_3$, neither LAO nor STO in bulk form exhibit ferromagnetism. A number of recent magnetotransport, magnetization and spectroscopic investigations[2,5–10] confirmed ferromagnetic behaviour of the conducting interface. A negative magnetoresistance (MR) observed in the magnetotransport with a field and temperature dependence is like a paramagnet and therefore attributed to magnetic behaviour. The origin and nature of this magnetism is still under debate.

In order to gain more understanding about the type of scattering process influencing the interface carriers, we have performed magnetotransport on a LAO/STO heterostructure in the temperature range between 0.3 K and 4.2 K, as a function of magnetic field-oriented perpendicular and parallel to the interface. The data show a temperature-independent linear Hall resistance, temperature-dependent negative MR and a hysteretic behaviour. The observed negative MR is found to be independent of the orientation of the magnetic field for all temperatures. Our low-temperature negative MR results can be understood with the spin scattering model proposed earlier by Brinkman et al.,.[2] Finally, we show that the observed hysteresis in LAO/STO is an artefact of the experimental setup, and is not an intrinsic property of the interface.

6.2 Sample preparation and experimental set-up

Our sample was grown by pulsed laser deposition, as described in chapter 2 (section 2.2). The 10 nm (26 unit cells) LAO film was deposited on a 5 mm × 5 mm TiO_2-terminated single crystal STO [001] substrate, at a substrate temperature of 850°C and an oxygen pressure of 2×10^{-3} mbar. The specific growth conditions of LAO layer are similar to the ones described in chapter 3 (section 3.2). The temperature dependent magnetotransport measurements are performed in van der Pauw geometry following the procedure described in chapter 4 (section 4.2).

6.3 Experimental results and discussion

Fig. 6.1(a) shows the sheet resistance R_s as a function of temperature between 0.3 K and 4.2 K, corresponding to region I in Fig. 4.1. R_s decreases logarithmically when increasing the temperature. A similar behaviour in the sheet resistance was observed previously in LAO/STO,[2, 11–13] in $LaVO_3/SrTiO_3$, and in $LaNiO_3/SrTiO_3$ oxide heterostructures.[14, 15] This low-temperature logarithmic increase of resistance is usually attributed to the Kondo effect, arising from the scattering of conduction charge carriers from localized magnetic moments.[2] However also a non-magnetic origin has been evoked, i.e. weak localization. An effect arising from destructive interference of conduction channels leading to back-scattering at low-temperatures.[12, 13, 15, 16] The very strong, magnetic field-orientation-independent negative magnetoresistance R_s(B), which is observed to very high magnetic fields (Fig. 6.2) is difficult to explain with the weak localization model and we will not consider this model further.

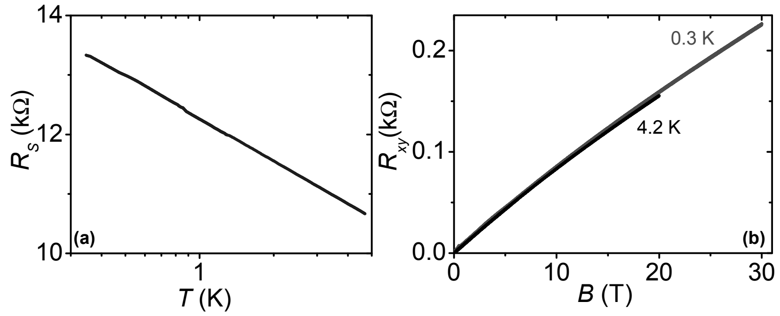

Figure 6.1: *(a) Sheet resistance R_s as a function of temperature (on a logarithmic scale) between 0.3 K and 4.2 K. (b) Hall resistance R_{xy} as a function of the applied magnetic field, at 0.3 K and 4.2 K.*

Fig. 6.1(b) shows the Hall resistance R_{xy} of the sample as a function of the applied magnetic field, at 0.3 K and 4.2 K. The R_{xy} measured is almost linear and temperature independent, which is described by a single band of charge carriers contributing to the transport, similar to chapters 3 and 4. The carrier concentration ($n_s = B/R_{xy}e$) and mobility ($\mu = 1/R_s(0)en_s$) are extracted from the data, resulting in $n_s = 8.7 \times 10^{13}$ cm^{-2} and $\mu_{4.2\ K} = 5$ cm^2 / Vs. The carrier concentration n_s remains constant for temperatures below 4.2 K. However, the increase in R_s for temperatures below 4.2 K (Fig. 6.1(a)) implies that, the carrier mobility decreases to $\mu_{0.3\ K} = 3$ cm^2 / Vs, and this effect can be attributed to increased carrier scattering from 'frozen' carriers (localized magnetic moments) and defects at low temperatures. This very low carrier mobility is similar to values previously observed in LAO/STO samples with comparable LAO layer thickness.[2,12] The low-temperature dependence of the mobility of this single band of charge carriers (Fig. 4.3(b)) is discussed earlier in chapter 4, and attributed to electron scattering off localized magnetic moments.

6.3.1 Negative magnetoresistance

Fig. 6.2 shows the sheet resistance R_s with the magnetic field-oriented perpendicular to the LAO/STO interface for temperatures between 0.3 K and 4.2 K as solid lines. For temperatures between 1 K and 4.2 K, R_s shows a negative MR with a dip close to zero magnetic field. R_s between 0.3 K and 1 K shows a slight hysteresis at low fields (below 3 T) and a pronounced negative MR at high fields (above 3 T extending to 30 T), its magnitude increases with decreasing T. The inset of Fig. 6.2 shows R_s data measured for the applied magnetic field-orientation perpendicular ($\theta = 0^o$) and parallel ($\theta = 90^o$) to the LAO/STO interface at 0.3 K.

We now concentrate on the negative MR at higher field, ignoring the minimum and the hysteresis near zero field for the moment. This negative MR is independent of the magnetic field-orientation for all the temperatures between 0.3 K and 4.2 K. This observation is in disagreement with previously reported magnetic field orientation dependent negative MR for LAO/STO heterostructures. However these samples had a thinner LAO film, and were fabricated at different deposition conditions compared to our sample.[16,23] In those samples the negative MR was attributed to 2D weak localization phenomena. This effect arises from orbital effect and depends on the perpendicular magnetic field as reported previously for the LAO/STO interface.[16,23]

The negative MR we observed for the LAO/STO agrees with the magnetic moment spin scattering phenomena reported in various semiconducting and metallic materials, such as doped conventional semiconductors (In doped CdS and Mn doped GaAs),[17,18] noble metals doped with transitions elements (Au doped with Co),[19] magnetic semiconductor heterostructures (InMnAs/GaAlSb),[20] and perovskite oxide heterostructures ($LaNiO_3/SrTiO_3$).[15] For all these systems, the negative MR is attributed to scattering of conduction charge carriers with localized magnetic moments and follow a Brillouin type field and temperature dependence. The external magnetic field reduces this scattering since at high fields and low temperatures all spins become aligned which suppresses scattering and results in a decrease of resistance.[17]

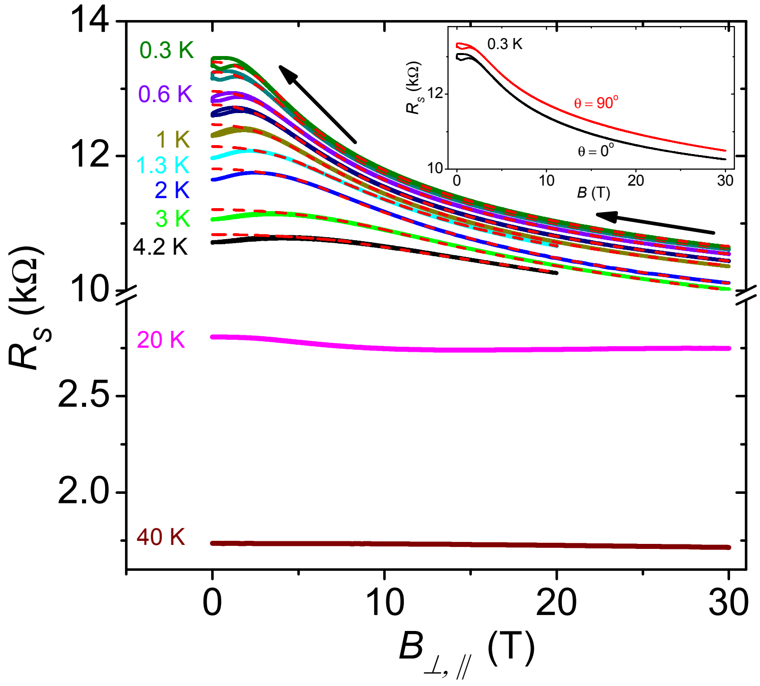

Figure 6.2: *Sheet resistance R_s with the magnetic field-oriented perpendicular ($B_\perp$) to the LAO/STO interface for temperatures between 0.3 K and 4.2 K, and R_s data with the magnetic field-oriented parallel ($B_{||}$) to the interface for temperatures at 20 K and 40 K, shown as solid lines. Dotted lines are parametrization (see text) of the negative MR data, the arrows indicate the direction of the magnetic field sweep. The y-axis is cut between 3 and 10 kΩ. The inset shows comparison of sheet resistance R_s data for the applied magnetic field-oriented both perpendicular ($\theta = 0^o$) and parallel ($\theta = 90^o$) to the interface at 0.3 K. In the Inset, R_s curves are offset vertically by 0.3 kΩ for clarity.*

Fig. 6.2 also shows the negative MR data measured with magnetic field oriented parallel to the LAO/STO interface for intermediate temperatures at 20 K and 40 K. With the magnetic field in the plane of interface, we have zero Hall resistance, and also exclude the contribution of the orbital MR (positive) which arises due to the two-channel conduction effects (at intermediate temperatures,

Fig. 4.3). Therefore, we only measure the spin related contribution to the MR (negative). The magnitude of the negative MR strongly deceases from 50% at 50 mK[24] to 20% at 0.3 K and further down to 2% at 40 K as T increases, and becomes negligible above 40 K. This behaviour is consistent with spin polarization.

To study the influence of LAO layer thickness and of the capping layers, we performed temperature-dependent magnetotransport on three other samples with different layers structure (as schematically depicted in Fig. 1 of appendix A), namely: 10 LAO/STO (10 unit cells of $LaAlO_3$ film grown on $SrTiO_3$ substrate), 2 STO/10 LAO/STO (10 unit cells of $LaAlO_3$ film grown on $SrTiO_3$ substrate, capped by two monolayers of $SrTiO_3$), and

2 STO/1 SCO/10 LAO/STO (10 monolayers of $LaAlO_3$ grown on a $SrTiO_3$ substrate, capped by one monolayer of $SrCuO_3$ (SCO) and two monolayers of $SrTiO_3$). In all the three samples we have observed a temperature-dependent negative MR behaviour (as shown in Fig. 1 of appendix B), which is qualitatively similar to the one shown in Fig. 6.2. Therefore the negative MR observed in parallel field is a very robust phenomenon and does not depend on the layers structure of the LAO/STO heterostructures. A similar decrease in magnitude of negative MR with increasing temperature has been observed by the other groups in LAO/STO samples grown at similar deposition conditions[21] and for 2D electron systems on the surface of $SrTiO_3$,[22] and was attributed to the depolarization of magnetic moments by thermal excitation.[21, 22]

6.3.2 Parametrization of negative magnetoresistance

We parameterized the R_s (negative MR) data up to 30 T at different temperatures below 4.2 K, ignoring the contribution of low-field positive MR and the hysteretic behaviour of R_s for the time being. Using the function $(-A_1{*}B^2{+}R_1)$ at low fields ($< 5\ T$) and a single exponential decay function $(A_2{*}e^{-B/\beta}{+}R_2)$ at high-fields ($> 5\ T$); where A_1 and A_2 are resistance amplitudes, B is the applied magnetic field, β is a resistance decay field. R_1 is the extrapolated zero field resistance of the low-field parametrization and R_2 is the high-field saturation value for $B > \beta$. The parametrization of the negative MR is shown as dashed lines in Fig. 6.2. Both functions used for the parametrization of negative MR for low-fields ($< 5\ T$) and high-fields ($> 5\ T$), represented as $(-A_1 * 5^2 + R_1)$ $= (A_2 * e^{-5/\beta} + R_2)$ and are continuous. Fig. 6.3 shows the parameters used in the parabolic (Fig. 6.3(a)) and exponential functions (Figs. 6.3(b) and (c)) to reproduce the negative MR data. The parameters A_1, A_2, and R_1, R_2 have similar (logarithmic) T-dependence, whereas β behaves differently, increasing with temperature from 0.3 K to 4.2 K. Therefore the parameters A_1, A_2, and

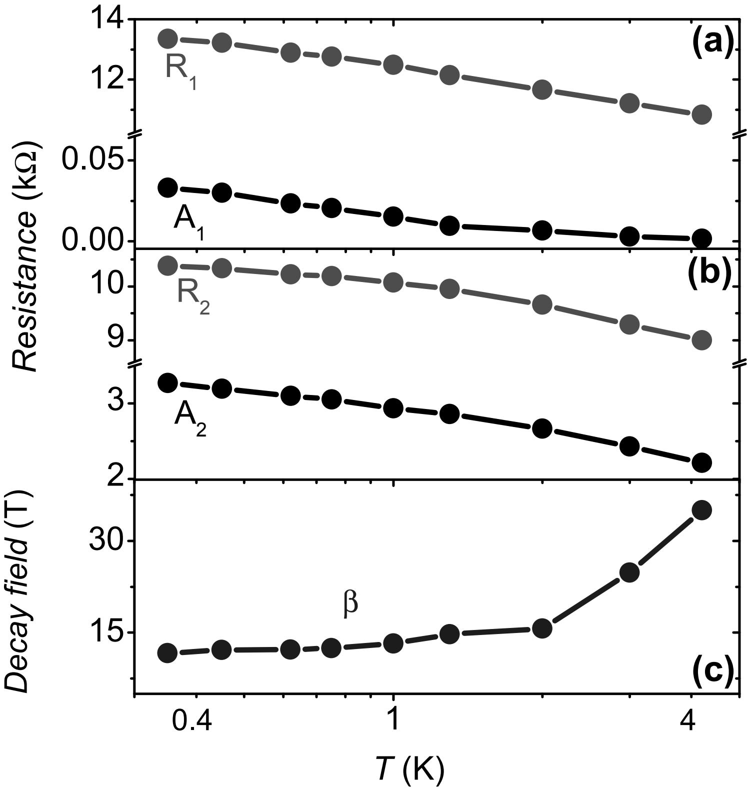

Figure 6.3: *Parameters A_1, A_2, and R_1, R_2, β used for the parametrization of the (a) low field (< 5 T), and (b) and (c) high field (> 5 T) data shown as dashed lines in Fig. 6.2, as a function of temperature (on a logarithmic scale). The resistance axes is cut between 0.065 to 10.25 kΩ in (a), and 3.5 to 8.6 kΩ in (b).*

R_1, R_2 behave similarly to R_s as a function of temperature (Fig. 6.1(a)). The resistance decay field β is an indication of how fast the negative MR changes its slope towards saturation in the applied magnetic field, and shifts towards higher fields with increase in temperature as shown in Fig. 6.3(c).

We use this parameterized negative MR data to perform the analysis of our results by following the procedure reported by Brinkman et al.[2] With the picture of negative MR originating from reduced spin scattering of conduction

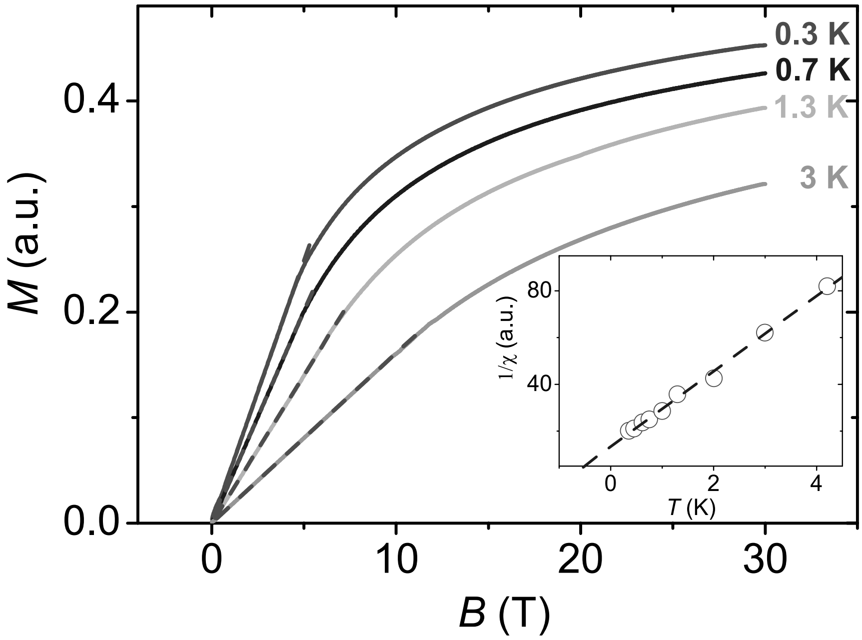

Figure 6.4: *Magnetization M obtained from the spin-scattering model as a function of magnetic field, shown as solid lines, for clarity we only show M curves of four temperatures. Linear fit (dotted lines) of the low-field part of the curve gives the susceptibility ($\chi = dM/dH$). The inset shows the inverse susceptibility as a function of temperature as a open symbols and fit of the Curie-Weiss law, shown as dotted line.*

electrons, the observed negative MR can be related to the global magnetization (M) by:[26]

$$M(B) \propto -\sqrt{\frac{R_s(B) - R_s(0)}{R_s(0)}}. \tag{6.1}$$

We use this formula to calculate the magnetization from our parameterized negative MR data, and show the results in Fig. 6.4. The slope of the linear part of the magnetization curve gives the low-field susceptibility, $\chi = dM/dH$.

The inverse susceptibility as a function of temperature is plotted in the inset of Fig. 6.4, from which a Curie-Weiss dependence $\chi = C/(T+\Theta)$ is found, where C is a constant and $\Theta = 0.5$ K is the Néel temperature, characteristic for antiferromagnetic coupling at an energy scale of $k_B\Theta = 40$ μeV. The magnetization curves at low-temperatures down to 0.3 K or even at 50 mK[24] do not show saturation in high magnetic fields, instead they depend linearly on B up to 30 T. This means either that the localized magnetic spin system does not completely align in the applied external magnetic field, or the spin scattering model we propose here is too simple to capture the saturation magnetization/full spin alignment.

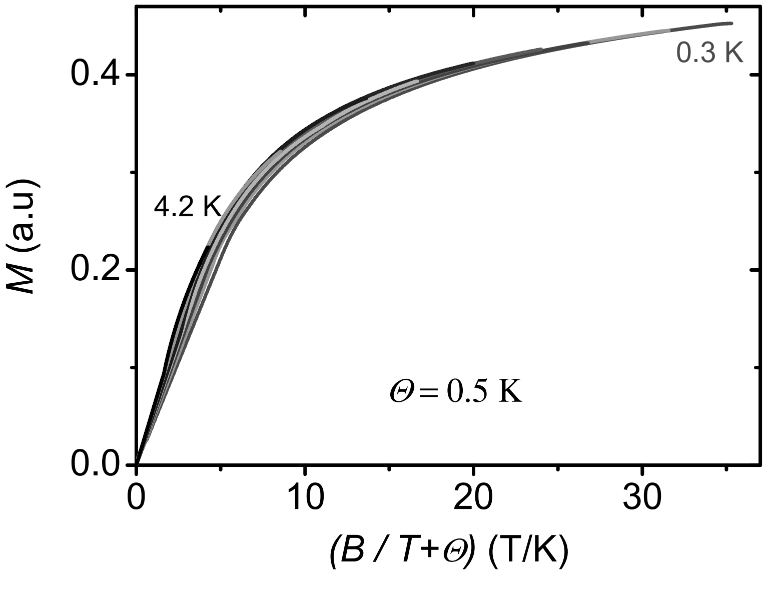

Figure 6.5: *Magnetization M obtained from the spin-scattering model as a function of $B/(T+\Theta)$, with a Néel temperature $\Theta = 0.5$ K.*

In Fig. 6.5, we plot the magnetization M curves from Fig. 6.4 as a function of $B/(T+\Theta)$, where $\Theta = 0.5$ K is the Néel temperature obtained from the Curie-Weiss dependence of the low-field susceptibility (inset of Fig. 6.4) obtained from our negative MR data. For low magnetic fields all the magnetization curves do not exactly coincide with each other, which could be due to small uncertainties in the parametrization of the low field part of the negative MR. For high magnetic fields the magnetization curves do coincide with each other in agreement with the Curie-Weiss dependence of magnetization. Considering the simplicity of the spin-scattering model we have used for analysis of the negative MR data, the agreement of magnetization with the Curie-Weiss dependence at different temperatures is notable.

For temperatures lower than the Néel temperature (0.5 K), the conduction charge carriers are localized in Ti-3d orbitals, resulting in Ti^{3+}-valence with a single unpaired localized spin. These localized carriers are antiferromagnetically coupled via the mobile carriers. In the presence of an applied magnetic field, the localized moments start to align resulting in reduced scattering with the itinerant charge carriers at the Fermi-level. This occurs due to finite Zeeman splitting between the spin-up and spin-down levels of the localized moments. It is evident from the analysis of our results that this simple spin-scattering model, i.e. the proportionality between the magnetization and the magnetoresistance (Eq. 6.1) does not hold for all the temperature and magnetic field range. However, the observed logarithmic increase of R_s for low-temperatures and analysis of the magnetic field-orientation-independent of negative MR in the order of few tens of percentage, clearly points towards the presence of localized moments antiferromagnetically coupled via the mobile carriers.

6.3.3 Hysteretic effects

Finally, we focus on the magnetic hysteresis behaviour we observed at low field (below 3 T). Fig. 6.6(a) shows R_s as a function of magnetic field, for two different sweep rates, fast (40 mT/s) and slow (5 mT/s) at 0.3 K. R_s measured for fast sweep rate shows hysteresis at low fields. Similar hysteretic behaviour in R_s was reported previously for LAO/STO and $GdTiO_3/SrTiO_3$ heterostructures.[2,27] From systematic testing, we found that the observed hysteretic behaviour is an experimental artefact, rather than an intrinsic feature of the interface itself.

Hysteresis as a function of magnetic field is generally observed in magnetic materials. It mainly indicates two types of physical phenomena, one is a change in the magnetic state of the underlying spin system, such as a phase transition from paramagnetic to ferromagnetic state. The second possibility could come from the change in temperature of the magnetic spin system at adiabatic conditions as a function of magnetic field, known as the magnetocaloric effect. The hysteretic behaviour observed in LAO/STO is strongly dependent on the magnetic field sweep rate as shown in Fig. 6.6(a). For the slow magnetic field sweep rate (5 mT/s) the hysteresis disappears completely. For the fast sweep rate (40mT/s), the underlying magnetic spin system we are measuring shows strong

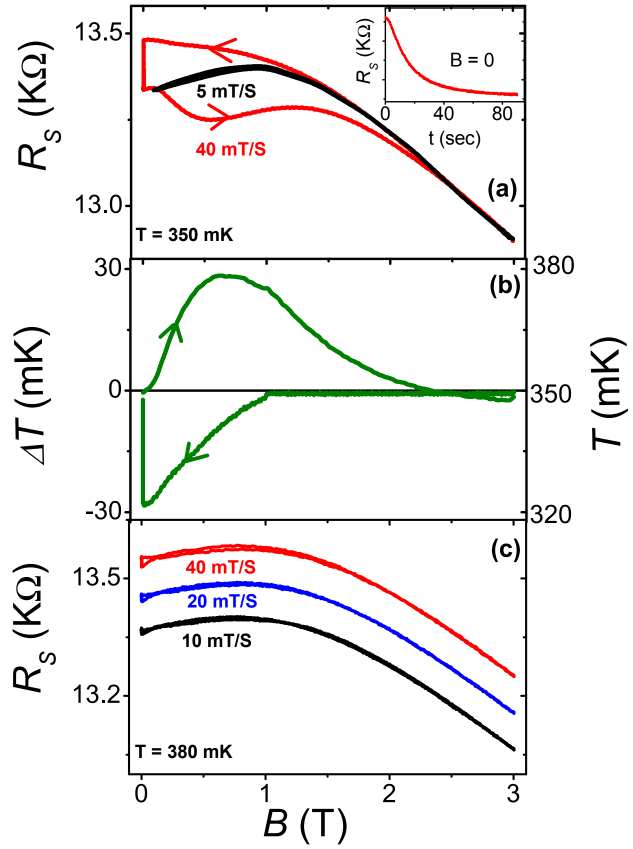

Figure 6.6: *(a) Sheet resistance R_s at 350 mK as a function of magnetic field for up- and down-sweeps with two sweep rates (40 mT/s and 5 mT/s). Arrows indicate the sweep direction, the inset shows the relaxation time of R_s after a magnetic field sweep down to $B = 0$ with 40 mT/s sweep rate. (b) Temperature change of the interface electrons deduced from the hysteresis observed in (a) at 40 mT/s and the temperature dependence of the resistance shown in Fig. 6.1(a). (c) Sheet resistance at 380 mK measured on a similar sample without the standard chip carrier (sample holder) for up- and down-sweeps as a function of magnetic field with three different sweep rates at 10, 20, 40 mT/s. No hysteresis is observable. The traces are shifted for clarity.*

hysteretic behaviour. The observed hysteresis shows a peculiar magnetic field sweep rate dependence and it has an unconventional butterfly shape, which is symmetric in positive and negative magnetic field polarity. These observations are in contradiction with the hysteresis observed in conventional ferromagnetic materials such as iron or nickel. From these physical characteristics of the hysteretic behaviour we cannot reliably attribute its origin to a magnetic phase transition of the spin system we are measuring in LAO/STO.

In that case, another possible explanation for the hysteresis could come from the magnetocaloric effect. According to this phenomenon, the magnetic spin system we are measuring is no longer in thermal equilibrium with surroundings when we sweep the magnetic field, resulting in the hysteretic behaviour in R_s. In particular, when the magnetic field is swept faster there is not sufficient time for the underlying spin system to relax back to the equilibrium state which results in a hysteresis in R_s (Inset of Fig. 6.6(a)). For the slow magnetic field sweep rate, the magnetic spin system has sufficient time to relax back to the equilibrium state and it remains in thermal equilibrium with the surroundings as a function of magnetic field, resulting in no hysteretic behaviour in R_s (Fig. 6.6(a)).

This resistance change or hysteresis observed in R_s during the fast field sweep (Fig. 6.6(a)) can be converted into an absolute temperature change of the magnetic spin system from equilibrium temperature using the R_s vs T curve of the sample (Fig. 6.1(a)). This change in temperature, corresponding to the hysteresis in R_s, during the fast field sweep (40 mT/s) relative to the equilibrium curve (slow sweep rate, 5 mT/s) at 0.3 K is shown in Fig. 6.6(b). It indicates that during the fast sweep, the temperature of the magnetic spin system increases by $\sim$ 30 mK between 0 and 3 T, and decreases by the same amount during the sweep to zero field. It thus seems quite reasonable to consider that we have observed the magnetocaloric effect of the magnetic spin system present in the LAO/STO interface.

In order to confirm the possible magnetocaloric effect phenomenon of the conducting LAO/STO interface we performed additional experiments. We measured the sample without the standard chip carrier sample holder that we used in the earlier measurements. The R_s results of the measurements without the chip carrier, as a function of magnetic field, for sweep rates of 10, 20 and 40 mT/s, is shown in Fig. 6.6(c). The results reveal that the hysteresis effect completely disappeared for all magnetic field sweep rates. This means that the hysteresis behaviour measured from the sample in the presence of the standard (slightly magnetic) chip carrier is due to the magnetocaloric effect of the chip carrier itself, rather than the intrinsic property of the LAO/STO sample. At the same time, we also measured the negative MR with a small dip around zero field similar to the measurements performed in the presence of the chip carrier.

After critical analysis of our experimental results we clarify that the hysteresis effects measured in the sample in the presence of chip carrier are an experimental artefact and the negative MR is an intrinsic property of the conducting LAO/STO interface.

6.4 Summary

In summary, our low-temperature experimental results show strong temperature dependent negative MR which is independent of the magnetic field-orientation, accompanied by a magnetic hysteresis at low-fields. Analysis of our negative MR, using the procedure proposed by Brinkman et al., reveals the presence of magnetic moments which are antiferromagnetically coupled via the itinerant charge carriers, in agreement with earlier reports.[2] The strong decrease of the magnitude of negative MR as the temperature is increased above 4.2 K is observed in four different LAO/STO heterostructures, and is attributed to the depolarization of magnetic moments by thermal excitation. We clarify that the origin of the magnetocaloric effect lies in the standard (slightly magnetic) chip carrier rather than from the intrinsic LAO/STO interface. Though our experimental results clearly point to the presence of magnetic moments at the interface, the interpretation we make from the simple spin-scattering model is still tentative.

References

[1] A. Ohtomo and H.Y. Hwang, Nature **427**, 423 (2004).

[2] A. Brinkman, M. Van Zalk, J. Huijben, U. Zeitler, J. C. Maan, W. G. Van der Wiel, G. Rijnders, D. H. A. Blank, and H. Hilgenkamp, Nature Mater. **6**, 493 (2007).

[3] J. F. Schooley, W. R. Hosler, and M. L. Cohen, Phys. Rev. Lett. **12**, 474 (1964).

[4] H. P. R. Frederikse, W. R. Hosler, W. R. Thurber, J. Babiskin, and P. G. Siebenmann Phys. Rev. **158**, 157 (1967).

[5] M. Ben Shalom, C. W. Tai, Y. Lereah, M. Sachs, E. Levy, D. Rakhmilevitch, A. Palevski, and Y. Dagan, Phys. Rev. B **80**, 140403 (2009).

[6] Ariando, X. Wang, G. Baskaran, Z. Q. Liu, J. Huijben, J. B. Yi, A. Annadi, A. R. Barman, A. Rusydi, S. Dhar, Y. P. Feng, J. Ding, H. Hilgenkamp, and T. Venkatesan, Nature Commun. **2**, 188 (2011).

[7] D. A. Dikin, M. Mehta, C. W. Bark, C. M. Folkman, C. B. Eom, and V. Chandrasekhar, Phys. Rev. Lett. **107**, 056802 (2011).

[8] L. Li, C. Richter, J. Mannhart, and R. C. Ashoori, Nature Phys. **7**, 762 (2011).

[9] J. A. Bert, B. Kalisky, C. Bell, M. Kim, Y. Hikita, H. Y. Hwang, and K. A. Moler, Nature Phys. **7**, 767 (2011).

[10] J.-S. Lee, Y. W. Xie, H. K. Sato, C. Bell, Y. Hikita, H. Y. Hwang, and C.-C. Kao, Nature Mater. **12**, 703 (2013).

[11] C. Bell, S. Harashima, Y. Hikita, and H. Y. Hwang, Appl. Phys. Lett. **94**, 222111 (2009).

[12] T. Hernandez, C. W. Bark, D. A. Felker, C. B. Eom, and M. S. Rzchowski1, Phys. Rev. B **85**, 161407 (2012).

[13] F. J. Wong, R. V. Chopdekar, and Y. Suzuki, Phys. Rev. B **82**, 165413 (2010).

[14] Y. Hotta, T. Susaki, and H. Y. Hwang, Phys. Rev. Lett. **99**, 236805 (2007).

[15] R. Scherwitzl, S. Gariglio, M. Gabay, P. Zubko, M. Gibert, and J.-M. Triscone, Phys. Rev. Lett. **106**, 246403 (2011).

[16] A. D. Caviglia, M. Gabay, S. Gariglio, N. Reyren, C. Cancellieri, and J.-M. Triscone, Phys. Rev. Lett. **104**, 126803 (2010).

[17] R. P. Khosla and J. R. Fischer, Phys. Rev. B **2**, 4084 (1970).

[18] F. Matsukura, H. Ohno, A. Shen, and Y. Sugawara, Phys. Rev. B **57**, R2037 (1998).

[19] A. N. Gerritsen, Physica **25**, 489 (1959).

[20] A. Oiwa, A. Endo, S. Katsumoto, Y. Iye, H. Ohno, and H. Munekata, Phys. Rev. B **59**, 5826 (1999).

[21] X. Wang, W. M. Lü, A. Annadi, Z. Q. Liu, K. Gopinadhan, S. Dhar, T. Venkatesan, and Ariando, Phys. Rev. B **84**, 075312 (2011).

[22] M. Lee, J. R. Williams, S. Zhang, C. D. Frisbie, and D. G.-Gordon, Phys. Rev. Lett. **107**, 256601 (2011).

[23] A. D. Caviglia, S. Gariglio, N. Reyren, D. Jaccard, T. Schneider, M. Gabay, S. Thiel, G. Hammerl, J. Mannhart, and J.-M. Triscone, Nature (London) **456**, 624 (2008).

[24] M. van Zalk, Ph.D. Thesis, *In between matters, Interfaces in complex oxides* (University of Twente, 2009) p 100.

[25] G. Bergmann, Phys. Rep **107**, 1 (1984).

[26] A. C. Hewson, *The Kondo Problem to Heavy Fermions* Cambridge Univ. Press, Cambridge (1993).

[27] P. Moetakef, J. R. Williams, D. G. Ouellette, A. P. Kajdos, D. Goldhaber-Gordon, S. J. Allen, and S. Stemmer, Phys. Rev. X **2**, 021014 (2012).

Appendix A

Multi-band conduction in $LaAlO_3/SrTiO_3$ heterostructures with different layers structure

A.1 Samples

In addition to the magnetotransport measurements on the 26 LAO/STO sample discussed in chapter 4, we also performed temperature-dependent magnetotransport measurements on three other LAO/STO heterostructures with different layers structure as illustrated in Fig. A.1. These are, 10 LAO/STO (10 unit cells of $LaAlO_3$ film grown on $SrTiO_3$ substrate), 2 STO/10 LAO/STO (10 unit cells of $LaAlO_3$ film grown on $SrTiO_3$ substrate, capped by two monolayers of $SrTiO_3$), and 2 STO/1 SCO/10 LAO/STO (10 monolayers of $LaAlO_3$ grown on a $SrTiO_3$ substrate, capped by one monolayer of $SrCuO_3$ (SCO) and two monolayers of $SrTiO_3$). The LAO film in all the four samples was deposited on a TiO_2-terminated single crystal STO [001] substrate, at a substrate temperature of 850°C and an oxygen pressure of 2×10^{-3} mbar. This procedure is similar to the deposition of the LAO layer for the earlier discussed 26 LAO/STO sample in chapter 4. The details of the growth conditions for the heterostructure 2 STO/1 SCO/10 LAO/STO discussed here are similar to the sample S2 (2 STO/1 SCO/9 LAO/STO) mentioned in chapter 5.

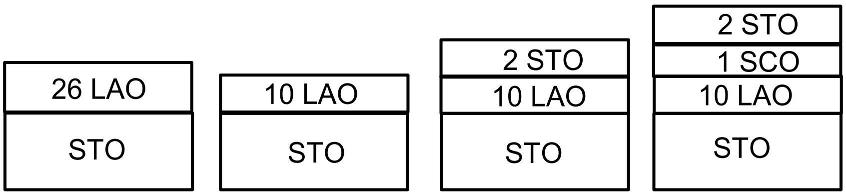

Figure A.1: *Schematic of LAO/STO heterostructures with four different layers structure.*

A.2 Experimental results and discussion

Figs. A.2(a) and (c) show the relative magnetoresistance (MR), Figs. A.2(b) and (d) show the Hall resistance of the samples 10 LAO/STO and 2 STO/10 LAO/STO, respectively, as a function of magnetic field, for temperatures between 4.2 K and 65 K. The observed strongly non-linear Hall resistance and positive MR for temperatures above 22 K can be quantitatively explained using a similar two band model analysis described in chapter 4. The two band model fits to the Hall resistance (Figs. A.2(b) and (d)) and positive MR (Figs. A.2(a) and (c)) are shown as solid lines in Fig. A.2.

The two band model fits are in good agreement with the experimental curves

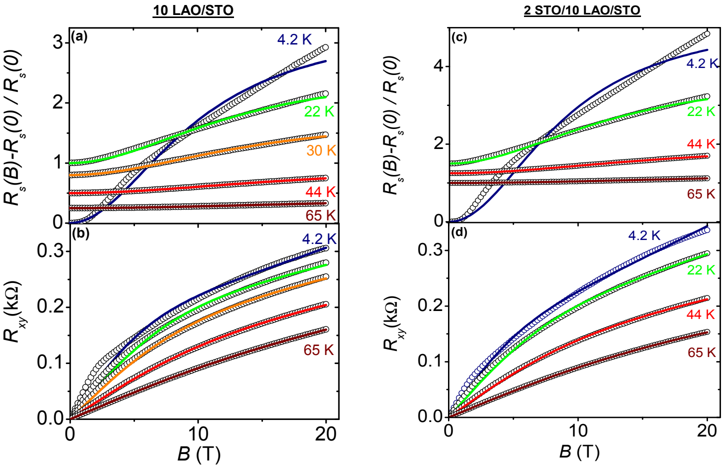

Figure A.2: *(a) and (c) Relative magnetoresistance (MR), (b) and (d) Hall resistance data with magnetic field-orientation perpendicular to the interface, for the samples 10 LAO/STO, and 2 STO/10 LAO/STO, respectively, up to 30 T, between 4.2 K and 65 K shown as open circles. The MR curves are shifted vertically for clarity, solid lines are two-carrier model fits to the experimental data.*

of non-linear Hall resistance and positive MR at high temperatures (above 22 K). The obtained values for the fit parameters n_1, n_2 are shown in Fig. A.3(a) and the fit parameters μ_1, μ_2 are shown in Fig. A.3(b) for the temperatures between 30 K and 65 K.

For the low-temperatures between 4.2 K and 22 K, this simple two carrier model does not describe all the details of the positive MR and non-linear Hall resistance as shown in Fig. A.2. The two band model fits are performed by supposing that all the four fit parameters are to be magnetic field independent. For the low-temperatures, we have observed strong negative MR and its origin has been attributed to the scattering off the conduction carriers with the localized magnetic moments as we discussed in chapters 4 and 6. Therefore it is reasonable to consider that the charge carriers mobility could be magnetic field dependent, including such magnetic field dependent fit parameters might improve the fits at low-temperatures.

For the case of 10 LAO/STO and 2 STO/10 LAO/STO samples, the thermal

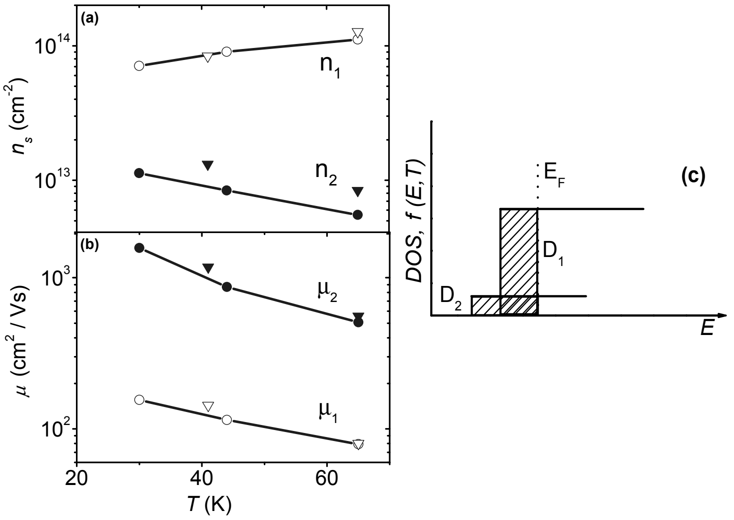

Figure A.3: *(a) The temperature-dependence of carrier density (n_1(open circles, open triangles), n_2(filled circles, filled triangles)), and (b) mobility (μ_1(open circles, open triangles), μ_2(filled circles, filled triangles)) values used to model the experimental data with two-carrier model. The open (filled) circles are fit parameters of the 10 LAO/STO data and the open (filled) triangles are fit parameters of the 2 STO/10 LAO/STO data showed in Fig. A.2. The connecting solid lines between the data points are guides to the eye. (c) Schematic representation of the 2D level structure with constant density of states for the two parallel electron-like conduction channels (D_1 and D_2) at the interface. At T = 0 K, both level D_1 and D_2 are occupied up to the Fermi energy E_F (dotted line); at higher T, broadening of the Fermi function results in the further increase in occupation of level D_1.*

activation of the high-mobility carriers (n_2) is suppressed, instead the carrier density is slightly decreased for the temperature range from 30 K to 65 K (Fig. A.3(a)). The carrier density (n_1) in the low-mobility channel increased from $\sim 5 \times 10^{13}$ to $\sim 1 \times 10^{14}$ cm^{-2} for the same temperature range. This might be due to the thermal depopulation of n_2 into n_1. The mobilities (μ_1 and μ_2) of both electron channels is slightly decreased for the temperature range from 30 K to 65 K. In these two samples, the mobility values (Fig. A.3(b)) of the low-mobility channel (μ_1) are slightly higher compared to the 26 LAO/STO sample (Fig. 4.3(b) in chapter 4). It should be noted that the fit parameters for these two LAO/STO samples with and without STO capping layer are very similar. This means that the addition of a STO capping layer to the LAO/STO heterostructure does not effect the interface electronic structure.

As already introduced in chapters 3 and 4, we explain results of these two samples by tentatively considering two simplified interface electronic states with a constant 2D density of states D_1 and D_2 as schematically depicted in Fig. A.3(c). At finite (low) temperature, the charge carriers occupy both electronic channels D_1, D_2 and contribute to the transport. The two electronic channels co-exist at the similar energy, as a result of change in the position of the high-mobility channel with respect to the low-mobility channel (compared to Fig. 4.4(b)). Therefore, the electronic properties of these two samples are influenced by the combination of contributions from both high-mobility and low-mobility channels due to similar carrier densities in the both channels, even at the lowest temperatures.

Fig. A.4(a) and (b) shows the positive MR and Hall resistance data of the sample 2 STO/1 SCO/10 LAO/STO, as a function of magnetic field for temperatures between 1.2 K and 65 K (open symbols). The two-band model fits to the Hall resistance (Fig. A.4(b)) and positive MR (Fig. A.4(a)) are shown as solid lines. The two-band model fits are in good agreement with the experimental curves of both non-linear Hall resistance and positive MR for higher temperatures (above 22 K). The obtained values for the fit parameters n_1, n_2 are shown in Fig. A.4(c) and the fit parameters μ_1, μ_2 are shown in the Fig. A.4(d) for the temperatures at 42 K and 65 K. The carrier density of the high-mobility carriers (n_2) is higher than the low-mobility carriers (n_1) as shown in the Fig. A.4(c). The total carrier density is around $\sim 1 \times 10^{13}$ cm^{-2} and is one order of magnitude smaller than compared to the other three samples. As increase in the temperature from 40 K to 65 K only changes the mobility of the two-channels rather than their carrier density (Fig. A.4(d)). Using this simple two carrier model we could not describe all the details of the MR at low-temperatures between 1.2 K and 22 K.

We explain our results of 2 STO/1 SCO/10 LAO/STO sample, by tentatively considering two simplified interface electronic states with a constant 2D density of states D_1 and D_2 as schematically depicted in Fig. A.4(e). At finite (low) temperature, the charge carriers first occupy the high-mobility electronic channel D_2. As a result, the ground state of the this system is dominated by the high-mobility (μ_2) carriers which are relatively high in number. At low temperatures below 4.2 K, we observe quantum oscillations in the longitudinal magnetoresistance (chapter 5), with this two-carrier model based on Drude formalism we cannot describe the quantum oscillations. The detailed description and analysis of the quantum oscillations measured in this type of samples is

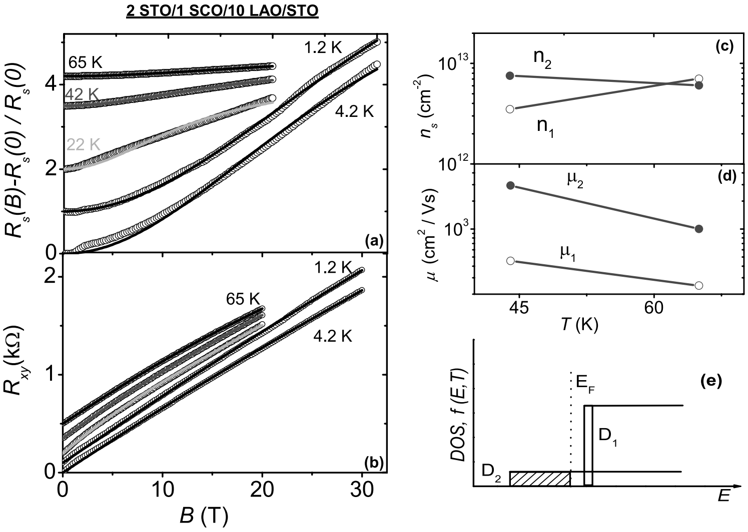

Figure A.4: *(a) Relative magnetoresistance and (b) Hall resistance data for magnetic field orientation perpendicular to the LAO/STO interface up to 30 T, between 4.2 K and 65 K (open circles), for the sample 2 STO/1 SCO/10 LAO/STO. (solid lines) Two-carrier model fits to the experimental data, the curves are shifted vertically for clarity. (c) and (d) The temperature-dependence of carrier density (n_1 and n_2), and mobility (μ_1 and μ_2) values used to model the experimental data with two-carrier model at high temperatures (42 K and 65 K). The connecting solid lines between the data points are guides to the eye. (e) Schematic representation of the 2D level structure with constant density of states for the two parallel electron-like conduction channels at the interface. At $T = 0$ K, the high-mobility level D_2 is occupied up to the Fermi energy E_F (dotted line); at higher T, broadening of the Fermi function results in the occupation of the low-mobility level D_1 (inverted with respect to the electronic structure described in chapter 4, Fig. 4.4(b)).*

given in chapter 5.

The magnetotransport results from four different samples (including the 26 LAO/STO sample from chapter 4), clearly shows the presence of at least two-electron like channels, one with high-carrier density (n_1) and low-mobility (μ_1) and a second one with low-carrier density (n_2) and high-mobility (μ_2), influencing the transport properties at the LAO/STO interface. The energetic alignment (Fig. 4.4(b), Fig. A.3(c) and Fig. A.4(e)) of both the electronic channels depends on the sample structure. The relative contribution of each channel to the transport in different samples (26 LAO/STO, 10 LAO/STO, 2 STO/10

LAO/STO and 2 STO/1 SCO/10 LAO/STO) defines the ground state magnetotransport properties of the interface.

From our analysis of the magnetotransport data of these four samples (Fig. A.1) using simple two-carrier model we cannot determine the exact physical origin of these interface conduction channels. However, we could suggest that for intermediate and high temperatures, there are at least two parallel electronic channels with different mobility are contributing transport are responsible for the observed magnetotransport behaviour at the LAO/STO interface.

Appendix B

Negative magnetoresistance in $LaAlO_3$/$SrTiO_3$ heterostructures with different layers structure

In chapter 6 we describe the magnetotransport measurements performed to investigate the nature of magnetic scattering in LaAlO$_3$/SrTiO$_3$ heterostructures, with 10 nm LAO film, in high magnetic fields and at various temperatures. In addition, in order to study the influence of LAO layer thickness and the influence of capping layers on the negative MR in parallel magnetic fields, we performed temperature-dependent magnetotransport on three other samples with different configurations (as schematically depicted in Fig. 1 of appendix A). The details of the growth conditions for these samples are discussed in appendix A.

Fig. B.1 shows the relative magnetoresistance data for the magnetic field-oriented parallel to the interface for the samples 10 LAO/STO (Fig. B.1(a)), 2 STO/10 LAO/STO (Fig. B.1(b)), and 2 STO/1 SCO/10 LAO/STO (Fig. B.1(c)). As we have discussed in chapter 6, the origin of observed negative MR is attributed to scattering of conduction charge carriers with localized magnetic moments. The external magnetic field reduces this scattering and results in a decrease of resistance.

Though we can tentatively explain the negative MR, we still do not understand the origin of positive MR and other features observed in parallel magnetic field for these three samples. This could be due to the fact that at finite (low) temperature, the charge carriers occupy two electronic channels (high mobility and low mobility) and contribute to the transport (as depicted in Fig. A.3(c) and Fig. A.4(e) of appendix A). The electronic properties of these samples are influenced by the combination of contributions from these two channels, starting from the lowest temperatures. As a result, these two band effects influence the magnetotransport in the parallel magnetic field might result in the positive MR. Further understanding of these MR features in the parallel magnetic field is for the future work on LAO/STO heterostructures.

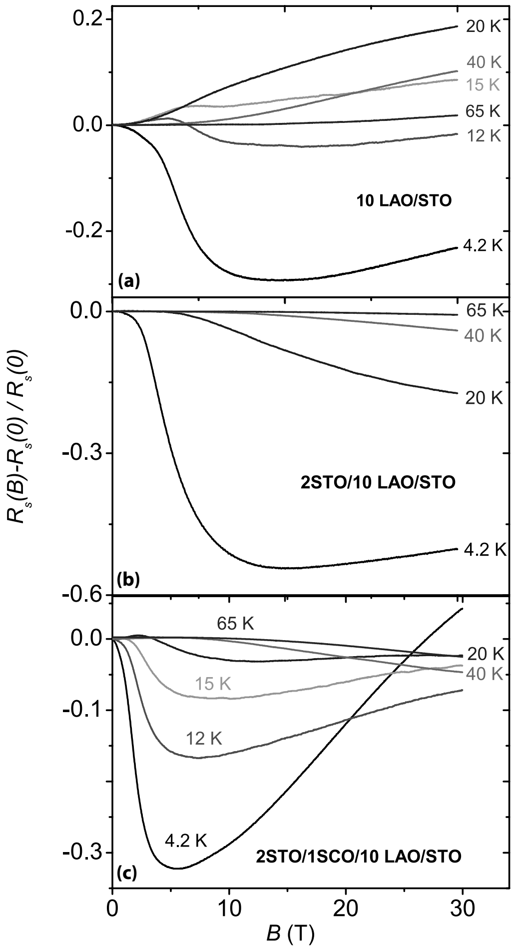

Figure B.1: *(a)-(c) Relative magnetoresistance data for magnetic field-oriented parallel to the interface for the samples 10 LAO/STO, 2 STO/10 LAO/STO, and 2 STO/1 SCO/10 LAO/STO up to 30 T, between 4.2 K and 65 K shown as solid lines.*

Summary

This thesis presents experimental investigations concerning magnetotransport properties of the two-dimensional electron system (2DES) formed in $LaAlO_3/SrTiO_3$ (LAO/STO) heterostructures. We concentrated on two seemingly quite different systems, namely 26 monolayers of LAO directly grown on STO and 10 monolayers of LAO grown on STO with an additional SrCuO2 (SCO)/STO cap. In the former system a high-concentration, low-mobility 2DES exhibiting magnetic scattering is observed, whereas the latter forms a high-mobility, low concentration 2DES displaying Shubnikov-de Haas oscillations. A core finding of our work is that both these channels can coexist in LAO/STO hetorostructures albeit with their energetic alignment depending on the growth conditions.

The thesis starts with a general chapter 1, which briefly introduces the conducting interface formed between two band insulating oxides STO and LAO and expounds the three main proposed mechanisms to explain the origin of a conducting 2DES at the LAO/STO interface. Secondly, we provide a general motivation why it is interesting and essential to understand the fundamental physical properties of this new type of oxide heterostructures, in particular in the view of their promising technological applications.

The specific growth procedures used for the fabrication of oxide heterostructures and the general transport properties of two-dimensional electron systems are then described in chapter 2. In particular we introduce in some detail to the van der Pauw procedure used to perform magnetotransport on all our LAO/STO samples. We review the theoretical concepts used to explain magnetotransport properties of semiconductor heterostructures in the classical and in the quantum-mechanical regime. These general concepts are of specific relevance to the following chapters.

One of the central messages of this thesis is experimental observation of multi-

band conduction in LAO/STO heterostructures. In chapters 3 and 4 we specifically show that (at least) two electron channels are contributing to the transport in the conducting interfaces. In chapter 3 we do this by (permanently) modifying the electronic properties of the 2DES using illumination with UV light. Here, the appearance of a pronounced positive magnetoresistance accompanied by a strongly non-linear Hall resistance is explained in terms of optical excitation of an additional high mobility electron channel, which is not visible prior to illumination.

The presence of this high-mobility channel is further confirmed by temperature dependent magnetotransport experiments presented in chapter 4. Subjecting the samples to temperatures above 4.2 K leads to a significant decrease of its resistance, a strong positive magnetoresistance appears and the Hall resistance becomes distinctly non-linear. We again can explain these results by embracing the existence of a second high-mobility channel in the structure. Furthermore, our experimental results put this channel energetically 6 meV above the low mobility channel. Interestingly, the coexistence of two electron channels with significantly different mobilities is also observed on LAO/STO samples with thinner LAO layers (20, 15, 10, 5 unit cells of LAO, see chapter 4 and appendix A). Due to a different energetic alignment the channels mostly coexist in these types of samples, even at the lowest temperatures, and as a consequence, a clear distinction of their individual contribution to magnetotransport is no longer possible.

In chapter 5 we concentrate on the high-mobility channel alone where we describe magnetotransport experiments on LAO/STO interfaces with 9 or 10 layers of LAO caped with 1 monolayer of SCO and 2 monolayers of STO. The addition of these capping layers increases the mobility of the 2DES formed at the interface by an order of magnitude which enables us to observe quantum oscillations in the magnetoresistance and the Hall resistance. Further analyses of these oscillations reveal that several 2D subbands with different effective masses and mobilities are present within the interface 2DES. By comparing our experimental results with recent theoretical work, we suggest that the hybridisation of the subbands at the interface with mixed Ti-3d orbital character is responsible for the observed interface electronic properties.

Finally, in chapter 6, we turn back to the 26 LAO/STO system. Its low temperature ($T \leq 4.2$ K) resistance is dominated by a single, low-mobility / high-concentration electron channel with a very pronounced negative magnetoresistance which is independent on the orientation of the magnetic field. This effect can be explained by spin scattering on antiferromagnetically coupled localised magnetic moments. Specifically, our experiments then allow determining the spin-orientation of these localised moments and the strong decrease of the magnitude of the negative magnetoresistance with increasing temperature can be attributed to their thermally induced depolarisation.

Samenvatting

Dit proefschrift beschrijft experimenteel onderzoek van magnetische transport eigenschappen in twee dimensionale elektron systemen (2DES) gevormd in $LaAlO_3/SrTiO_3$ (LAO/STO) heterostrukturen. We concentreren ons op twee schijnbaar tamelijk verschillende systemen, namelijk 26 enkellaags LAO gegroeid op STO en 10 enkellaags LAO gegroeid op STO met een aanvullende SrCuO2 (SCO)/STO toplaag. In het eerste systeem, een hoog geconcentreerd zwak mobiel 2DES, is magnetische verstrooiing waargenomen. Het tweede systeem met een hoge mobiliteit en lage concentratie 2DES, laat Shubnikov- de Haas oscillaties zien. Een voornaam resultaat van ons werk is dat beide kanalen tegelijk kunnen bestaan in een LAO/STO heterostruktuur, waarbij the energetische eigenschappen afhangen van de groeicondities.

Het proefschrift begint met een algemeen hoofdstuk 1, waarin kort het gevormde geleidende grensvlak beschreven wordt tussen twee oxide isolator banden STO en LAO. Daarnaast worden de drie voornaamste mechanismen toegelicht welke de oorsprong vormen van het geleidende 2DES LAO/STO grensvlak. Daarnaast geven we een algemene motivatie wraarom het intressant en belangrijk is om de fundamentele fysische eigenschappen van dit nieuwe type heterostructuur te begrijpen, in het bijzonder met het oog op veelbelovende technologische toepassingen.

De specifieke groei procedure die gebruikt is om de geoxideerde heterostrukturen te maken en de algemene transport eigenschappen van twee dimensionale elektron systemen zijn beschreven in hoofdstuk 2. In het bijzonder beschrijven we de Van der Pauw procedure om magnetische transport te meten in alle LAO/STO samples. We bespreken de theoretisch concepten die gebruikt worden om de magnetische transport eigenschappen van halfgeleiders te beschrijven in het klassieke en het kwantummechanische regime. Deze algemene concepten zijn relevant voor de volgende hoofdstukken.

Een van de centrale boodschappen in dit proefschrift is de experimentele observatie van multiband geleiding in LAO/STO heterostrukturen. In hoofdstuk 3 en 4 laten we specifiek zien dat (op zijn minst) twee elektronen kanalen bijdragen aan het transport in het geleidende grensvlak. In hoofdstuk 3 laten we dit zien door de elektronische eigenschappen van de 2DES (permanent) te wijzigen met behulp van UV belichting. De verschijning van een duidelijk positieve magnetische weerstand, begeleid met een sterke niet lineare Hall weerstand, wordt verklaard in termen van de optische excitatie van aanvullende sterk mobiele elektronenkanalen, welke niet zichtbaar waren voorafgaand aan de belichting.

De aanwezigheid van deze sterk mobiele kanalen is verder bevestigd door de temperatuur afhankelijke magnetische transport experimenten die gepresenteerd worden in hoofdstuk 4. Het onderwerpen van samples aan temperaturen groter dan 4.2 K leidt tot een significante daling van de weerstand, een sterke positieve magnetische weerstand verschijnt en de Hall weerstand wordt (onderscheidbaar) niet linear. Opnieuw kunnen we deze resultaten verklaren met behulp van het bestaan van een tweede sterk mobiele kanaal in de struktuur. Daarnaast laten onze experimenten zien dat dit kanaal 6 meV boven het zwak mobiele kanaal ligt. Het is interessant dat de aanwezigheid van twee kanalen ook is geobserveerd in LAO/STO samples met dunnere LAO lagen (20, 15, 10, 5 eenheidscellen van LAO, zie hoofdstuk 4 en appendix A). Vanwege een verschillende energetische uitlijning bestaan beide kanalen gelijktijdig in dit type samples, zelfs bij de laagste temperaturen. Daaruit volgt dat een duidelijk onderscheid in de individuele bijdragen van de magnetische transport eigenschappen niet meer mogelijk is.

In hoofdstuk 5 concentreren we ons enkel op het sterke mobiele kanaal, hier beschrijven we de magnetische transport experimenten van LAO/STO grensvlakken met 9 of 10 lagen van LAO met een laag SCO en twee lagen STO er bovenop. Het toevoegen van deze toplagen laat de mobiliteit van de gevormde 2DES op het grensvlak toenemen met een orde van grootte. Zodoende kunnen quantum oscillaties in de magnetische weerstand en Hall weerstand gemeten worden. Een aanvullende analyse van deze oscillaties onthult dat verschillende 2D subbanden, met verschillende effective massas en mobiliteiten, aanwezig zijn binnen het 2DES grensvlak. Door onze experimentele resultaten te vergelijken met recentelijk theoretisch werk, denken we dat de kruising van de subbanden op het grensvlak met het gemixte orbital karakter van Ti-3d verantwoordelijk is voor de geobserveerde elektronische eigenschappen op het grensvlak.

Tot slot keren we terug naar het 26 LAO/STO systeem in hoofdstuk 6. De lage temperatuur ($T \leq 4.2$ K) weerstand van het systeem wordt gedomineerd door een enkele, zwak mobiel/sterk geconcentreerd elektronen kanaal met een sterk negatieve magnetische weerstand die onafhankelijk is van het magneetveld. Dit effect kan uitgelegd worden met behulp van spin verstrooiing in antiferromagnetisch gekoppelde gelocaliseerde magnetische momenten. Om precies te zijn kunnen onze experimenten de spin orientatie bepalen van deze gelocaliseerde momenten en kan de sterke daling van de grootte van de negatieve magnetische weerstand met toenemende temperatuur toegewezen worden aan de thermisch geinduceerde depolarisatie.

Acknowledgements

The work presented in this thesis is an outcome of ongoing cooperation between High Field Magnet Laboratory (HFML) and MESA+ Institute for Nanotechnology. I am happy to have had taken part in this research programme during the past four years. This thesis would have never been possible without the direct (indirect) scientific, technical and social support I have received from numerous colleagues, friends and family. I would like to personally thank them in this acknowledgement section.

First of all, I would like thank my daily supervisors. Alix, thank you for introducing me to the good practice of handling cryogenics, very clean way of soldering contacts and for learning the procedures to perform magnetotransport experiments. You always have few minutes for me to talk about the experiments and for discussing the results. I have really appreciated your patience in correcting my (not so good) English in magnet time proposals, conference abstracts, publications and in this thesis.

Uli, thank you for your openness that I could walk into your office any time and ask for help or discuss about the experiments and results. On top of that, I enjoyed the flexibility you allowed in my Ph.D., which enabled me to work on other interesting topics like magnetization (VSM) and magneto-optics. I am really grateful to your helpful attitude in solving the issues with the installation several times in the nights/earlymornings. I clearly remember one such incident of answering phone call and coming immediately to HFML at 2:30 am on a Saturday morning.

The measurements in this thesis would not have been possible without the technical support from the respective staff at HFML. I would like to thank Harry, Stef, Jos P., Hung, Jos R., Frits, Frans, and Arjen for their support with the smooth running of the installation. And Lijnus, Jos R., Jos van V. and Michel support with the making/fixing inserts and cryogenic equipments. Hung, it was nice learning experience for me to work with you on improvements of vibrating sample magnetometer (VSM), thank you for staying some days until late in the evening and coming to the lab on some weekends to fix problems.

I am also grateful to Ine, and Martin, Annette (FOM) en Maria (FOM) that you are always willing to help me with many practical issues especially in dealing with Dutch bureaucracy (making appointments and filling forms), that helped me a lot to start and during my stay at HFML without much administrative troubles.

Further I would like to acknowledge my fellow PhDs, Post-Docs, students and staff who made all the lunch, coffee breaks, social activities *borrels en lab uitstapjes* as memorable ones, as well as babysitting for my measurements during the weekends and nights: Alan, Andreas, Andres, Andries, André, Arend, Alessandro, Bhawana, Erik K., Erik van E., Francesca, Frans, Genia, Giorgio, Hans E., Harmen, Ineke, Jan, Jonas, Masumeh, Laurens, Lennart, Papori, Peter A., Peter C., Peter van R., Peter R., Roger, Steffen, Stevan, Thomas, Dima, Wei, Suruchi, Szymon, en Victor. Special mention of few of them Erik van E., though I am not working in graphene, thank you for learning me how to setup a magnetotransport experiment using lock-in amplifier and you are always ready to help with experiments and preparation for seminars. Andres, our measurements of three days resulted in a publication and is chapter of this thesis. Apart from that, It was really nice time travelling to conferences, and summer schools. Thanks also for your patience for listening to me and supporting me also on a personal level. Andreas, scientific discussions that we had during the preparation two-band analysis paper were very much helpful and thank you for also reading and commenting on the paper, which is also a chapter in this thesis. Peter van R., it was nice to have as my office mate and your help with making Dutch summary of thesis and it was nice to organize borrels together I liked it. Peter R., for proof reading the parts of this thesis. Szymon, for your help with matlab script for two-channel model, which is very helpful in the analysis of the experimental data (chapter 4) presented in this thesis.

I would like to thank Peter C. for his scientific inputs on magneto-optics measurements on LAO/STO samples and subsequently during the preparation of publication based on those measurements. And also for your feedback on my group seminars regarding improvements which resulted even in my presentation skills.

A special thanks to our collaborators Sander, Michelle, Alexander, and Hans H. at the University of Twente. Sander, I am indebted to you for the great job you did in making nice samples and also for your patience in explaining the procedures to make conducting LAO/STO heterostructures during my visit to Enschede. On top of that, we spent many long measurement nights and weekends together with the mixed experiences of some times exciting and some times not so encouraging results. All those results contributed significantly to this thesis, I would also like to wish you all the best with finalising your thesis. Alexander, scientific discussions with you helped a lot to improve my understanding on this topic and was also helpful when I wrote the publications. Hans en Alexander, special thanks for your timely feedback and comments on the publications that we prepared together, I think those comments were very much helpful in making our papers acceptable in the scientific journals.

Though I didn't have much possibility to make many friends in Nijmegen, there are some friends who made a difference for my stay in Nijmegen. I would like to remember few of them here: Raj, Suruchi, Papori, Roy, Davide, Els, Raj Kishore, Chandan, Ashim, Patsy, Arun, Abul. Raj, thanks a lot for your help with making some nice schematics for this thesis, I wish you all the best with your post-doc in USA. Arun, I am glad for your support during the past four years as my house mate. Abul, thanks for your help in the beginning of my stay here in Nijmegen. I am also grateful to my long time friend, Raj Kishore, for his friendship, guidance and suggestions in dealing with the various situations in both professional and personal level. Few families who always treated me one among them, I am grateful for their friendship: family of Robert Hoste, Michael Eijgenraam, Andrew Eijgenraam and Antal Zuurman. From Stockholm, I am glad to know the family of Farhat, Lalit, Snellman and van der Waal for their friendship and support they gave me from the past few years. Patrik, thank for visiting me few times in Nijmegen and I enjoyed all the time we spent talking and trips we travelled together. Els, thanks for the time you spent in listening to me despite your busy schedules in the past four years and I value all those conversations.

Last but not least, I am grateful for my family who always allowed and supported me to do whatever I liked, though it was not always easy for them. I am grateful for my mother, Rajeswari, for my father, Sambasiva rao, for my grandmother, Koteswaramma for their love and understanding (though I could only visit home only two times in the past seven years). I am also indebted to my brother, Nandeep, who took care of things back home during my absence and always stayed whole time with me whenever I visited my home.

List of Publications

1. A. McCollam, S. Wenderich, M. K. Kruize, V. K. Guduru, H. J. A. Molegraaf, M. Huijben, G. Koster, D. H. A. Blank, G. Rijnders, A. Brinkman, H. Hilgenkamp, U. Zeitler, and J. C. Maan, *Quantum oscillations and subband properties of the two-dimensional electron gas at the* $LaAlO_3/SrTiO_3$ *interface*, Applied Physics Letters: Materials 2, 022102 (2014).
2. V. K. Guduru, A. McCollam, A.Jost, S. Wenderich, A. Brinkman, H. Hilgenkamp, J. C. Maan, and U. Zeitler, *Thermally excited multiband conduction in* $LaAlO_3/SrTiO_3$ *heterostructures exhibiting magnetic scattering*, Physical Review B: Rapid Communications **88**, 241301(R) (2013).
3. V. K. Guduru, A. McCollam, J. C. Maan, U. Zeitler, S. Wenderich, M. K. Kruize, A. Brinkman, M. Huijben, G. Koster, D. H. A. Blank, G. Rijnders, and H. Hilgenkamp, *Multi-band conduction behaviour at the interface of* $LaAlO_3/SrTiO_3$ *heterostructures*, Journal of the Korean Physical society **63**, 437 (2013).
4. V. K. Guduru, A. Granados del Aguila, S. Wenderich, M. K. Kruize, A. McCollam, P. C. M. Christianen, U. Zeitler, A. Brinkman, G. Rijnders, H. Hilgenkamp, and J. C. Maan, *Optically excited multiband conduction in* $LaAlO_3/SrTiO_3$ *heterostructures*, Applied Physics Letters **102**, 051604 (2013).
5. S. Fabretti, I.-M. Imort, T. Kuschel, T. Dahm, V. K. Guduru, U. Zeitler, and A. Thomas, *Magnetic anisotropy of thin sputtered* MgB_2 *films on MgO substrates in high magnetic fields*, AIP Advances **4**, 037115 (2014).
6. V. Hutanu, A. P. Sazonov, M. Meven, G. Roth, A. Gukasov, H. Murakawa, Y. Tokura, D. Szaller, S. Bordács, I. Kézsmárki, V. K. Guduru, L. C. J. M. Peters, U. Zeitler, J. Romhanyi, and B. Náfrádi, *Evolution of the 2D antiferromagnetism with temperature and magnetic field in multiferroic* $Ba_2CoGe_2O_7$, Physical Review B 89, 064403 (2014).

7. M. Petrushevsky, E. Lahoud, A. Ron, E. Maniv, I. Diamant, I. Neder, S. Wiedmann, V.K. Guduru, F. Chiappini, U. Zeitler, J. C. Maan, K. Chashka, A. Kanigel, and Y. Dagan, *Probing the surface states in* Bi_2Se_3 *using the Shubnikov-de Haas effect*, Physical Review B **86**, 045131 (2012).

8. M. Veldhorst, M. Snelder, M. Hoek, T. Gang, V. K. Guduru, X. L. Wang, U. Zeitler, W. G. van der Wiel, A. A. Golubov, H. Hilgenkamp, and A. Brinkman, *Josephson supercurrent through a topological insulator surface state*, Nature Materials **11**, 417 (2012).

9. E. Marins, V. K. Guduru, A. Samantilleke, F. Cerqueira, and P. Alpuim, *High-rate deposition of nanocrystalline silicon thin films on plastics*, Physica Status Solidi C **8**, 846 (2011).

10. A. Sugunan, V. K. Guduru, A. Uheida, G. K. Rajarao, M. S. Toprak, and M. Muhammed, *Radially Oriented ZnO Nanowires on Flexible Poly-L-Lactide Nanofibers for Continuous-Flow Photocatalytic Water Purification*, Journal of American Ceramic Society **93**, 3740 (2010).

11. O. D. Jayakumar, A. Vinu, V. K. Guduru, T. Sakuntala, and A. K. Tyagi, *Room temperature ferromagnetism in* $Ce_{1-x}Fe_xO_{2-\delta}$ *(x = 0.0, 0.05, 0.10, 0.15 and 0.20) nanoparticles synthesized by combustion method*, Journal of Nanoscience and Nanotechnology **10**, 2299 (2010).

12. A. K. Nayak, M. Nicklas, S. Chadov, A. Kalache, P. Khuntia, C. Shekhar, M. Baenitz, Y. Skourski, V. K. Guduru, A. Puri, U. Zeitler, J. M. D. Coey, and C. Felser, *Design of compensated ferrimagnetic Heusler alloys for giant tunable exchange bias* (submitted).

13. A. Jost, V. K. Guduru, S. Wiedmann, S. Wenderich, A. Brinkman, H. Hilgenkamp, U. Zeitler, and J. C. Maan, *Transport and thermoelectric properties of the* $LaAlO_3/SrTiO_3$ *interface* (in preparation),

Curriculum Vitae

Veerendra kumar Guduru was born on the 26^{th} of August 1984 in Guntur, Andhra Pradesh, India. He completed his secondary school studies in Lutheran Model high school at Guntur. He obtained Bachelor of sciences (B.Sc) degree with profiles Mathematics, Physics and Chemistry from Acharya Nagarjuna University at Guntur in March 2004.
He received Master of science (M.Sc) in physics at the Pondicherry University at Puducherry in May 2006. He successfully finished his second M.Sc in Nanotechnology from Royal Institute of Technology at Stockholm in November 2009. As a part of Master's curriculum in Nanotechnology he did his graduation project titled "Deposition and characterization of hydrogenated nanocrystalline silicon thin films for flexible solar cell applications" at University of Minho, in the groups of Dr. Pedro Alpuim and Dr. Fátima Cerqueira.
In January 2010, Veerendra started as a PhD researcher for De Stichting voor Fundamenteel Onderzoek der Materie (FOM), placed at the High Field Magnet Laboratory under the supervision of Dr. A. McCollam, Dr. U. Zeitler and Prof. dr. ir. J. C. Maan. The main topic of his research consisted of the magnetotransport properties of the two-dimensional electron system formed in $LaAlO_3/SrTiO_3$ heterostructures. The results obtained during his PhD are described in this thesis.